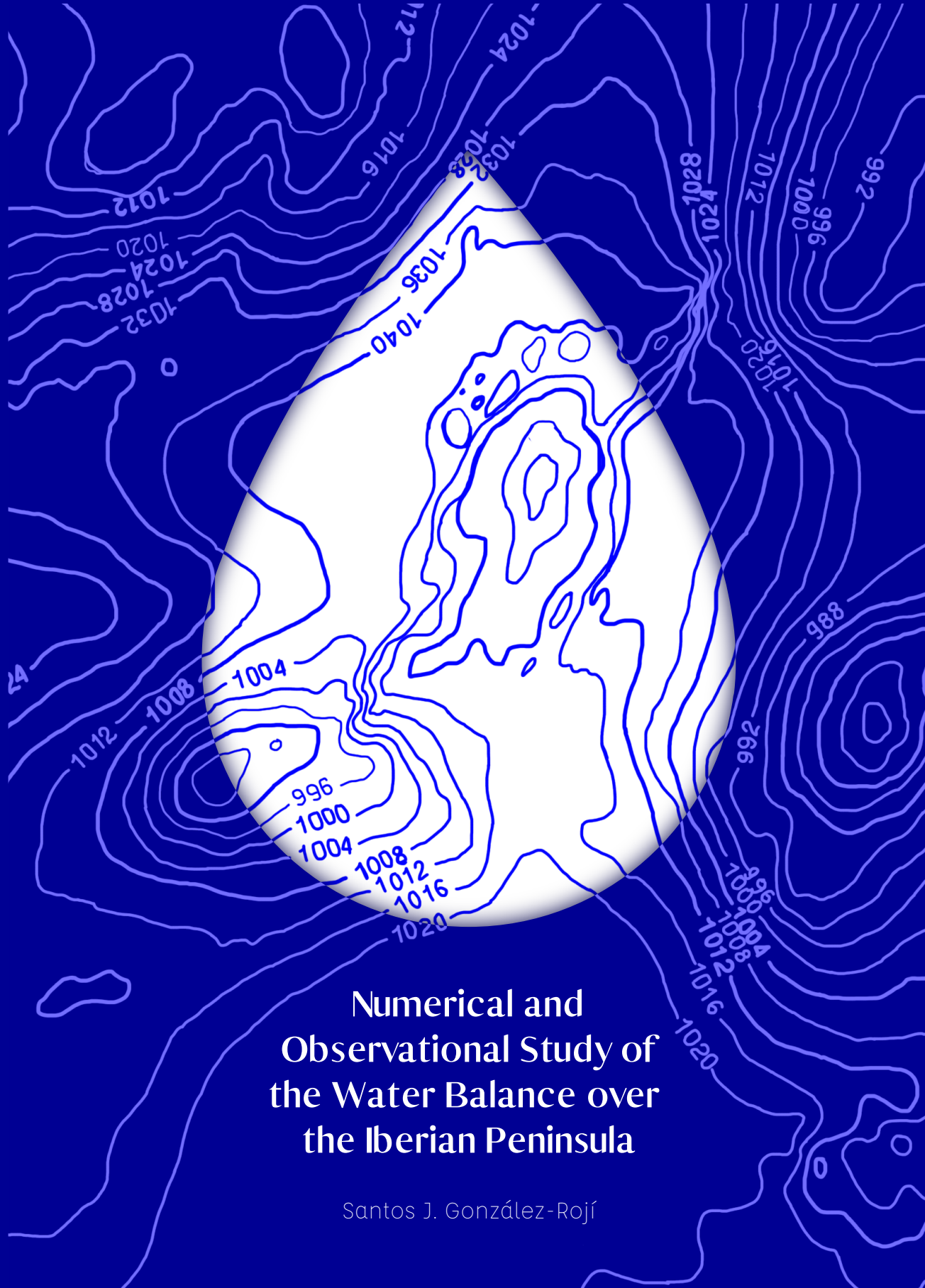


This thesis is intended for anyone curious about the role of precipitable water, evaporation, precipitation and transboundary fluxes in the Water Balance over the Iberian Peninsula. All of these atmospheric features are of paramount importance for natural processes, ecosystems and socioeconomic activities, hence their importance. Here, we explore the ability of the dynamical downscaling simulating those phenomena for period 2010-2014, and the simulated precipitation is compared against that downscaled by a statistical downscaling model.



Numerical and Observational Study of the Water Balance over the Iberian Peninsula

Numerical and Observational
Study of the Water Balance
over the Iberian Peninsula

Numerical and Observational Study of the Water Balance over the Iberian Peninsula

Santos J. González-Rojí

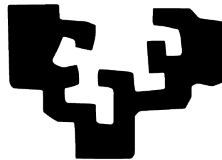
Supervised by

Jon Sáenz Agirre

and

Gabriel Ibarra-Berastegi

eman ta zabal zazu



Departamento de Física Aplicada II
Facultad de Ciencia y Tecnología
Universidad del País Vasco

February 2018

This PhD thesis was developed during the period from April 2015 to February 2018 at EOLO group. This work was funded by the Spanish Ministry of Economy, Industry and Competitiveness with a FPI Predoctoral Research Grant (ref: BES-2014-069977), associated to project CGL2013-45198-C2-1-R, led by Jon Sáenz. Two placements of three-and-a-half and two months were carried out during this period at the Department of Geography of Loughborough University, funded by IkaslePraktikak Grant (ERASMUS+ Internships for Students) from the *Erasmus+ Programme of the European Commission's Lifelong Learning Programme* and the Predoctoral Mobility Grant from the *Spanish Ministry of Economy, Industry and Competitiveness* (ref: EEBB-I-17-12513) respectively.

©2018 by Santos J. González-Rojí. All rights reserved.

An electronic version of this thesis can be found at <https://addi.ehu.es>

Bilbao, February 2018

Cover design by Maite Diez (www.maitediez.com).

This document was generated with the 2015 L^AT_EX distribution.

The L^AT_EX template is adapted from a template by Laura García-Álvarez.

To my family

Somewhere, something incredible is waiting to be known.

Carl Sagan

Contents

Abstract	i
Resumen	iii
Acknowledgements	ix
List of Publications	xi
List of Figures	xv
List of Tables	xvii
Abbreviations and conventions	xix
1 Introduction	1
1.1 Objective	4
1.2 What you will find in this thesis	5
2 Data and Methodology	7
2.1 Datasets	7
2.2 Dynamical Downscaling Simulations	12
2.3 Postprocessing the Model Outputs	16
2.4 Statistically Downscaled Model Data	17
2.5 Validation Datasets and statistical indicators employed	21

2.6	Analysis of the Water Balance	23
3	Analysis of the Water Balance	25
3.1	Validation of Precipitable Water	25
3.2	Validation of Precipitation	29
3.3	Validation of Evaporation	35
3.4	Analysis of the Residual	42
3.5	Analysis of the Analysis Increments	44
3.6	Description of the main features of the hydrological cycle	46
4	Comparison of Downscaling Precipitation Models	51
4.1	Analysis of the predictor suites	52
4.2	Comparison of SDSM experiments	52
4.3	Analysis of statistical and numerical downscaling models	58
5	Applications	73
5.1	Validation of wind at 10 m over water	74
5.2	Measurements of offshore wind energy potential	77
6	aiRthermo	81
6.1	Key points of the methodology	82
6.2	Included functions	84
7	Discussion	89
7.1	Configuration of the models	89
7.2	Issues with the validation datasets	91
7.3	Further insight on the results	93
8	Conclusions	97
8.1	Conclusions	98
8.2	Future perspectives	101
	Appendices	103
A	Predictor suites for SDSM experiments	105
B	Taylor diagrams for each region of the IP	111
C	Details on the methodology for the calculation of wind farm related variables	117
C.1	Wind at 10 m	117
C.2	Capacity Factor and Annual Energy Production	118
	Bibliography	119

Abstract

An in depth analysis of the atmospheric branch of the water balance and daily precipitation downscaling is presented for the Iberian Peninsula during the period 2010-2014.

The closure of the balance was studied internally according to the model results after applying different configurations. To do so, two numerical integrations at 15 km horizontal resolution were developed by means of the WRF model nested in ERA-Interim. Both simulations spanned the period 2009-2014, but the first year was considered as a spin-up for the model. The first experiment (N) was configured as in standard numerical downscaling runs, where the boundary conditions drive the model. The same parameterizations were applied to the second experiment (D), but it also included a 3DVAR data assimilation step every six hours. Each term of the water balance was firstly validated against the ERA-Interim reanalysis and several observational datasets: radiosondes and MODIS data for precipitable water, EOBS, ECA&D, TRMM and GPCP for precipitation and GLEAM for evaporation.

The verification showed that the scores obtained by the D experiment were better than those from N, and similar to the results obtained by the driving reanalysis (better in some cases). Thus, the most reliable water balance was provided by the D experiment. According to it, the leading terms are the tendency of the precipitable water, the divergence of moisture flux, evaporation and precipitation. No spatial patterns were recognizable for the annual accumulated evaporation. In contrast, high values of precipitable water were observed in summer near the Mediterranean and Cantabrian coasts. In precipitation, the influence of the Atlantic fronts was recognizable. The transboundary moisture fluxes through the contour of the Iberian

Peninsula vary seasonally. During winter, a net moisture import is measured. In contrast, during spring, summer or autumn, the moisture is exported towards the Mediterranean, and only during midday are the breezes able to reverse this feature.

The comparison of daily precipitation downscaled via statistical and dynamical downscaling was carried out by comparing the above mentioned both WRF simulations with the outputs from an statistical model (SDSM) at twenty-one stations evenly spaced over the Iberian Peninsula. The most similar configuration to that used in WRF was developed for SDSM: ERA-Interim data at 0.75° resolution provided predictor variables necessary to calibrate SDSM from 1979-2009. Apart from comparing downscaled daily precipitation with ERA-Interim, some observational datasets were included for the evaluation period 2010-2014: ECA&D, TRMM, GPCP and E-OBS datasets. The twenty-member ensemble created by the SDSM was not only analysed according to its mean, but also as if each individual member was an independent experiment.

Both WRF experiments and SDSM achieved verification scores similar to the ones obtained by those from observational datasets, but again, the D experiment outperformed N. Comparable correlations were obtained by the SDSM ensemble mean, D and ERAI in four regions of the Iberian Peninsula, but poor results were obtained by the ensemble members. Focusing on precipitation amount indices, the ensemble members outperformed D and particularly the ensemble mean. However, changing to precipitation occurrence indices, the D experiment was the best experiment. Similar results to those from D were obtained by the ensemble mean for wet-day occurrence and consecutive dry days, but not for the maximum five-day precipitation where the ensemble members were better. The Linear Error in Probability Space score showed that the ensemble members outperformed D and SDSM mean, but the Brier Skill Score stated that no added value was produced by the members of the ensemble. Thus, different verification indices lead to different assessments on which is the best downscaling method. However, even if the D experiment does not show the best scores for every calculated index, its results were more stable than those from the SDSM experiment.

The spatial and temporal resolution of our simulations makes them attractive to several kind of projects. In the thesis, the applicability of our WRF simulations was explored, validating the simulated wind field against observed measurements in the West Mediterranean. The offshore wind resources from two potential areas where wind farms could be installed in the Western Mediterranean were thus evaluated.

Additionally, as a direct consequence of the programming codes created during the thesis, the R-package *aiRthermo* was developed and publicly shared in CRAN repository. It includes several functions for the calculation of atmospheric thermodynamic variables, instability indices and Stüve diagrams.

Resumen

El objetivo de esta tesis es analizar el balance de humedad sobre la Península Ibérica simulado mediante diferentes configuraciones del modelo WRF (con y sin asimilación de datos), pero también comparar la capacidad predictiva de una técnica de downscaling estadístico (SDSM) y dinámico (WRF) aplicados a la precipitación. Esta zona de estudio es muy interesante puesto que en un mismo entorno confluyen muchos factores importantes para el balance de humedad. Particularmente, una compleja topografía, varias regiones climáticas (climas Árido, Mediterráneo, Oceánico y Alpino) y diferentes fuentes de precipitación (Atlántica y Mediterránea). Por ello, en un mismo dominio podremos analizar el comportamiento de ambas técnicas de downscaling y el efecto que produce la asimilación de datos en las simulaciones del balance de humedad.

El modelo numérico WRF será el encargado de llevar a cabo el downscaling dinámico, mientras que el SDSM será utilizado para realizar el downscaling estadístico. Ambos modelos han sido ampliamente utilizados en la literatura. Por un lado, el modelo WRF permite generar campos meteorológicos con mayor resolución que la de los modelos globales, y ha sido clave en el estudio de la evaporación, precipitación y humedad sobre la Península Ibérica. Incluso ha sido utilizado para identificar posibles efectos en temperatura y precipitación asociados al cambio climático. Por otro lado, SDSM es un modelo estadístico basado en las relaciones entre una variable observada y diferentes predictores en un lugar en concreto. Diferentes estudios prueban que este modelo es capaz de predecir correctamente la temperatura y precipitación observadas. Hasta el momento, tras revisar la literatura, no se ha llevado a cabo una comparación directa entre ambos modelos para una región compleja como la

Península Ibérica, y tampoco se ha simulado numéricamente el balance de humedad de esta región incluyendo la asimilación de datos. De ahí la novedad y el interés de ambos estudios.

En la primera parte de la tesis, se estudiaron las diferencias observadas en el balance de humedad simulado mediante dos simulaciones generadas con WRF. La configuración básica del modelo fue la misma para ambas simulaciones, actualizando la temperatura de la superficie del mar diariamente en el modelo e incluyendo las parametrizaciones para la radiación (esquema RRTMG), la fracción de nubes (esquema Xu-Randall), los cúmulos (esquema Tiedtke), la capa límite planetaria (esquema PBL) y la microfísica de las nubes (esquema WSM5). El modelo de suelo utilizado ha sido el Noah. En el primer experimento (N), las condiciones de contorno son proporcionadas al modelo para su correcto funcionamiento tras la inicialización en el primer ciclo. En el segundo experimento (D), se incluye un paso adicional en el que se lleva a cabo la asimilación de datos 3DVAR cada seis horas (00, 06, 12 y 18 UTC). La resolución espacial del dominio es la misma en ambos casos (rejilla de $15 \times 15 \text{ km}^2$) y los campos generados por el modelo se almacenan cada tres horas. Esta resolución (tanto espacial como temporal) es apropiada para este tipo de estudios. Mediante la comparación de ambas simulaciones hemos podido determinar las ventajas y desventajas del uso de la asimilación 3DVAR en WRF, además de poder evaluar cuán bien es capaz el modelo de cerrar el ramal atmosférico del ciclo del agua en una región como la Península Ibérica, caracterizada por una compleja topografía. El reanálisis ERA-Interim y otros conjuntos de datos observacionales (MODIS, EOBS, ECA&D, TRMM, GPCP, GLEAM y radiosondeos proporcionados por la Universidad de Wyoming) fueron incluidos en la validación de cada uno de los términos del ciclo hidrológico.

Cada uno de los elementos del balance de humedad fueron validados independientemente. Los resultados de la validación del contenido de vapor de agua precipitable mostraron que el experimento D es capaz de mejorar sistemáticamente la correlación, desviación estándar y RMSE obtenidos por el experimento N en ocho radiosondeos distribuidos uniformemente sobre la Península Ibérica. Este experimento (D) fue capaz incluso de mejorar los resultados del propio reanálisis ERA-Interim. Comparado con datos del conjunto MODIS, los resultados obtenidos fueron parecidos a los obtenidos con radiosondeos. En este caso, los valores de correlación obtenidos por D fueron mejores que los del experimento N y similares a los de ERA-Interim.

La validación de precipitación contra datos de EOBS mostró que ambas simulaciones de WRF y ERA-Interim producían valores bajos de correlación en la costa Mediterránea y en la cuenca del Ebro. Los peores resultados fueron producidos por el experimento N, pero el experimento con asimilación de datos fue capaz de corregirlos. Resultados parecidos fueron observados para el experimento D y ERA-Interim, pero el experimento D es también capaz de mejorar los resultados obtenidos por el reanálisis en el sur de la Península. Resultados similares a los observados con EOBS fueron obtenidos al comparar con el resto de conjuntos observacionales de precipitación (ECA&D, TRMM y GPCP). También en estos casos, el experimento D genera valores similares a los producidos por ERA-Interim y mejora los obtenidos

por el experimento N.

Centrándonos en la validación de la evaporación, se observó que el modelo WRF no es capaz de generar valores realistas de esta variable en aquellos puntos de malla cuyo uso de suelo haya sido definido como *zona urbana* dentro del modelo de suelo NOAA. En esos puntos, se obtienen correlaciones cercanas a cero (o incluso negativas) puesto que la evaporación generada por WRF no muestra variabilidad y sus valores son cercanos a cero. Por ello, todos estos puntos problemáticos fueron eliminados de la validación contra datos de GLEAM (versiones v3.0b y v3.0c). Resultados similares fueron obtenidos entre el experimento D y ERA-Interim. Sin embargo, en ambos casos se observaron valores bajos de correlación cerca de la costa Mediterránea y en el noroeste de la Península. Además, aunque los valores de correlación obtenidos entre el experimento D y ERA-Interim fueron parecidos, el ratio de evaporación simulado por ERA-Interim sobre toda la Península es superior al simulado tanto por el conjunto observacional GLEAM como por ambas simulaciones de WRF.

Después de haber evaluado cada término del ciclo hidrológico, se procedió al estudio del residuo generado por ambas simulaciones de WRF y ERA-Interim. El análisis de los residuos mostró que los términos con mayor importancia dentro del balance de humedad son la tendencia del contenido de vapor de agua precipitable ($\frac{\partial W}{\partial t}$), la divergencia de los flujos de humedad ($\vec{\nabla} \cdot \vec{Q}$), la evaporación (E) y la precipitación (P). Por lo tanto, los términos relacionados con los condensables no son importantes. El efecto de la asimilación de datos es perceptible en los residuos. Se observaron fuertes cambios en el valor de los residuos a lo largo del día (especialmente a las 18 UTC), relacionados principalmente con la asimilación de observaciones de humedad y/o temperatura en niveles bajos de la atmosfera. Ningún patrón espacial fue observado en estos resultados, ni en los valores de evaporación. Sin embargo, los patrones espaciales de la precipitación anual acumulada muestran una clara influencia de los frentes asociados a ciclones Atlánticos en la zona norte de la Península Ibérica.

Los flujos de humedad que atraviesan el contorno de la Península también fueron estudiados. Éstos mostraron una gran variabilidad entre estaciones. Durante los meses de invierno, gran cantidad de humedad entra en la Península a lo largo del día. Sin embargo, los flujos exportan de forma neta humedad durante los meses de primavera, verano y, a menor escala, otoño a través de la costa Mediterránea. Sin embargo, durante las horas centrales del día, las brisas cerca de la zona del Mar de Alborán (sur de la Península) invierten esta situación y facilitan la importación de humedad en la zona.

En la segunda parte de la tesis se llevó a cabo la comparación de la precipitación simulada gracias al downscaling estadístico calculada mediante SDSM y al downscaling dinámico mediante las simulaciones ya generadas con WRF. Esto nos permitió evaluar ambas técnicas y determinar cuál de ellas produce mejores resultados. El modelo SDSM se calibró con una configuración similar a la utilizada en las simulaciones con WRF. Para ello, se utilizaron como predictores datos procedentes del reanálisis ERA-Interim a una resolución de 0.75° . De esta forma, puede llevarse a cabo una justa evaluación de los puntos fuertes y débiles de cada técnica de downscaling. Por defecto, el modelo SDSM genera un ensemble de veinte miembros.

Por tanto, para poder comparar este producto probabilístico con las simulaciones deterministas de WRF, estudiamos la media del ensemble, pero también cada miembro como si de un experimento independiente se tratara.

Veintiún estaciones distribuidas a lo largo de la Península fueron elegidas para este estudio. La precipitación observada en cada una de estas estaciones, definida como predictando dentro del modelo estadístico, se obtuvo a partir de la base de datos ECA&D. Cada estación fue calibrada independientemente en el modelo SDSM, siguiendo una metodología basada únicamente en los indicadores producidos por el propio modelo. De esta forma, el usuario no necesita tener ningún conocimiento previo sobre los fenómenos atmosféricos predominantes en cada estación. Los resultados muestran que tanto las simulaciones creadas con WRF como por el SDSM producen resultados similares a los obtenidos por los conjuntos de datos observacionales (EOBS, TRMM y GPCP). Esto indica que ambas técnicas tienen habilidades predictivas similares a los datos observacionales.

La media del ensemble generado por SDSM, el experimento D y ERA-Interim obtuvieron valores de correlación similares en cuatro regiones definidas sobre la Península Ibérica. Sin embargo, los miembros del ensemble produjeron resultados que no eran comparables a los anteriores. Por tanto, estos resultados no fueron suficientes para determinar qué técnica de downscaling era superior. Por ello, muchos más índices tuvieron que ser calculados.

Para poder evaluar los puntos fuertes del experimento D, la media del ensemble y los miembros de ensemble más allá de los indicadores incluidos en los diagramas de Taylor, también se calcularon los índices LEPS (Linear Error in Probability Space) y BSS (Brier Skill Score). Estos índices nos ayudarán a determinar si los modelos son capaces de realizar una buena predicción de lluvia y si mejoran los resultados producidos por el reanálisis ERA-Interim. Por un lado, los miembros del ensemble obtuvieron los mejores resultados en cuanto al índice LEPS en un total de dieciséis estaciones, mientras que en las cinco estaciones restantes fue el experimento D el que se impuso. Sistemáticamente, el experimento D y los miembros del ensemble mejoraron los resultados producidos por la media del ensemble. Por el contrario, según el índice BSS, la media del ensemble y el experimento D fueron los experimentos que consiguieron mejorar la predicción de referencia (de ERA-Interim en este caso) y muestran valor añadido. Los miembros del ensemble no consiguen añadir valor al modelo global de baja resolución del reanálisis puesto que este índice tiene en cuenta la simultaneidad de la lluvia y no sólo la cantidad de precipitación medida.

Por último, además de los índices LEPS y BSS, se calcularon varios índices de precipitación con el fin de comprobar si ambas técnicas de downscaling son capaces de reproducir el comportamiento de la precipitación observada. Empezando por los índices relacionados con la cantidad de precipitación observada, se observó que el experimento D, la media del ensemble y los miembros del ensemble producen una media de precipitación similar. Sin embargo, los miembros del ensemble superan a los otros experimentos en cuanto a la intensidad de precipitación y el percentil 90. La media del ensemble produce los peores resultados en esos casos. Cambiando a los índices asociados a la ocurrencia de precipitación, los resultados cambian de un índice

a otro. La media del ensemble sobreestima el número de días secos consecutivos y la probabilidad de que ocurra un día húmedo, mientras que el experimento D y los miembros del ensemble los subestiman. Por el contrario, los miembros del ensemble sobreestiman el máximo de precipitación en 5 días consecutivos, pero el experimento D y la media del ensemble lo subestiman. Aunque el experimento D no presente los mejores resultados en estos indicadores, presenta unos resultados mucho más estables que los obtenidos por el SDSM, que varían según el índice estudiado. Por ello, sólo podemos afirmar que dependiendo del índice que estemos analizando, obtendremos una técnica más favorable para la obtención de mejores resultados. Esto no es arbitrario, sino que simplemente refleja que dependiendo de qué tipo de predicción se precise (determinista o probabilista), de los recursos técnicos (CPU y disco) disponibles y del tipo de ejercicio que se desarrolle, se elegirán unas u otras como óptimas.

También se ha explorado la potencial aplicabilidad de los experimentos numéricos llevados a cabo durante esta tesis a otros campos. La alta resolución de la malla utilizada en ambas simulaciones de WRF y la frecuencia de almacenamiento de salidas es muy atractiva para un amplio rango de proyectos. Estos datos permiten llevar a cabo estudios sobre el balance de humedad en otras regiones de Europa (incluso en zonas del océano Atlántico o mar Mediterráneo), pero también son aplicables a otro tipo de proyectos como estudio de brisas o modelización de eventos extremos pasados. Además, ambas técnicas de downscaling pueden aplicarse también al estudio de extremos de precipitación o inundaciones. Incluso para estudios sobre toma de decisiones, ya que el SDSM es capaz de generar resultados parecidos a los producidos por el downscaling dinámico, pero con menor coste computacional y para periodos mucho más largos.

En esta tesis, ambas simulaciones creadas con WRF han sido validadas con datos puntuales en boyas y conjuntos observacionales como el CCMPv2 sobre la región occidental del mar Mediterráneo. Resultados similares a los medidos sobre la Península Ibérica fueron observados en esta región, puesto que el experimento D produce resultados parecidos a los de ERA-Interim y mejores que los de N. Además, gracias al cálculo de varios estadísticos, se pudo determinar que el experimento D produce los resultados más realistas en esa región del Mediterráneo. Por ello, el viento a 10 m simulado por este experimento fue utilizado para el cálculo del factor de capacidad (CF) y la producción de energía anual en dos zonas de potencial instalación de parques eólicos flotantes, localizadas al este del Cabo Begur y al norte de Menorca.

La mayoría de los cálculos realizados durante la tesis fueron llevados a cabo mediante el lenguaje de programación R. Combinando estos programas con códigos en C para el cálculo de variables termodinámicas, se construyó el paquete *aiRthermo*. Este paquete fue publicado en Agosto de 2017 y actualmente está disponible para su descarga (gratuita) en el repositorio CRAN. Este paquete cubre un hueco entre los paquetes de R que pueden encontrarse en ese repositorio, puesto que los pocos paquetes meteorológicos disponibles hasta la creación de *aiRthermo* se centraban únicamente en el cálculo de algunas variables atmosféricas. Gracias a *aiRthermo*, el rango de funciones meteorológicas disponibles en R se ha ampliado, incluyendo ahora

funciones para el cálculo de índices de inestabilidad, ascensos y descensos adiabáticos de parcelas de aire, o incluso para el dibujo de diagramas de Stüve.

Por último, cabe decir que algunas preguntas surgidas durante el desarrollo de esta tesis se han dejado para llevar a cabo en proyectos futuros. Estos son algunos ejemplos. Se deben identificar qué mecanismos físicos pueden explicar la poca habilidad para simular una evaporación realista que presenta WRF en aquellos puntos definidos como *zona urbana* en el modelo de suelo NOAH. Se deben explorar qué efectos producirían en las simulaciones el aumento de la resolución espacial y/o temporal de las condiciones de contorno suministradas al modelo WRF. Se pueden estudiar aquellos flujos de energía que toman parte en generar el sesgo frío observado en el sur de la Península durante los meses de verano. Se debe estudiar cuán bien están representados los diferentes tipos de precipitación (de gran escala o convectivos) en ambas técnicas de downscaling, o cómo es la variabilidad interanual o estacional de la precipitación simulada por WRF y SDSM.

Acknowledgements

Now that these three years of working on my thesis are coming to an end, I will acknowledge all the people I have met during this journey and all the things that I have been able to learn from them. The time to say thank you has arrived.

First, I would like to deeply thank my supervisors Jon Sáenz and Gabriel Ibarra-Berastegi who have always supported and guided me professionally. They are the most approachable supervisors I have had and most probably will ever have. Since the first moment we met they have treated me as a member of the group and not just as a student who has recently finished a Master's degree. This is something that is scarcely found these days and for which I am truly grateful. With that in mind, I cherish the time I have spent with both of them, in both professional and personal capacities.

During these three years I have been very privileged with the opportunities I have been presented. I have been able to attend several international conferences and summer courses in many cities around the world: Boulder, Vienna, Dublin or Trieste amongst others. Furthermore, and thanks to this thesis, a small town in the middle of the United Kingdom called Loughborough was my second home for more than six months. It was there where my thesis become more complete with the help of Prof. Robert L. Wilby, who was always willing to help me. Not only did he help with the SDSM, but also with everything related with my placement at the Department of Geography. I am really happy to see how fruitful this collaboration has been.

This thesis has been developed at the EOLO research group in the University of the Basque Country (UPV/EHU). I want to thank all the members, particularly

Alain Ulazia, Ganix Esnaola and Javier Díaz de Argandoña, with whom I have collaborated in some research projects. Last, but not least, I would like to thank Sheila Carreño-Madinabeitia, who I met while I was doing my Master's and is now a friend and an occasional colleague.

My time at the university within the Applied Physics II department has been a pleasure thanks to all the people I have shared office with. Thanks to my officemates: Paul, Sheila, Iñigo G., Xabi and Iñigo R., and to the former ones: Sofia, Gerardo and Gemma. Also a thank you to those from neighbouring offices: Peio, Jon, Patricia, Leire, Aritz, Telmo, Iñaki, José Fernando, Bea, Unai and Nora. Not only there, PhD students from other departments have also supported me: Laura, Borja, Aitziber, Naiara, María, João, Pablo, Raúl, Iker, Fran, Mikel, Ibai, Olatz, Kepa, Nastassja, Charlotte, Nuria, Julen, Iraultza, Iagoba, Mattin, Iñigo A., Asier and Joanes. Now their friendship extends beyond the academic world. I cannot forget my friends in Loughborough, with whom I look forward to sharing more memorable moments: Chris, Penny, Jonesii, Milly, Andreas, Charlotte, Rich, Hatcher, Jo, Henk, Tim, James, Tom, Sam, Avi, Keechy, Ciara, Dan, Laura, Richard, Maud and Harry. Outside university, I want to thank my friends from my Master's: Inma, Hugo and Miguel, those from my degree in Physics: Andrea, Adriana, Alba, Lander, Laura, Xabier and Egoitz, and my friends that I have kept close since my school days. This has been a herculean task and I hope I have not forgotten anyone.

Finally, and above all, I would like to thank my family. In particular to my parents, for their unconditional love and support.

List of Publications

This thesis is based on the following publications and preprints:

Chapter 3: Analysis of the Water Balance

1. Santos J. González-Rojí, Jon Sáenz, Gabriel Ibarra-Berastegui and Javier Díaz de Argandoña (2018). *Moisture balance over the Iberian Peninsula according to a regional climate model: The impact of 3DVAR data assimilation*. In Journal of Geophysical Research, 122, <https://doi.org/10.1002/2017JD027511>.

Chapter 4: Comparison of Downscaling Precipitation Models

2. Santos J. González-Rojí, Robert L. Wilby, Jon Sáenz and Gabriel Ibarra-Berastegui (2018). *An evaluation of daily precipitation downscaled using SDSM and WRF+WRFDA models over the Iberian Peninsula*. Submitted to Climate Dynamics.

Chapter 5: Applications

3. Alain Ulazia, Jon Sáenz, Gabriel Ibarra-Berastegui, Santos J. González-Rojí and Sheila Carreno-Madinabeitia (2017). *Using 3DVAR data assimilation to measure offshore wind energy potential at different turbine heights in the West Mediterranean*. In Applied Energy, Volume 208, Pages 1232-1245, ISSN 0306-2619, <https://doi.org/10.1016/j.apenergy.2017.09.030>.

List of Figures

Chapter 2: Data and Methodology	7
2.1 Location of the chosen ECA&D stations	9
2.2 Location of the radiosondes from Wyoming University	10
2.3 Location of the buoys at the West Mediterranean	11
2.4 Domain and topography of both WRF simulations	13
2.5 Interactions between parameterization schemes	14
2.6 Structure of WRF simulations	15
2.7 Architecture of the SDSM	18
Chapter 3: Analysis of the Water Balance	25
3.1 Taylor diagrams comparing the observed PW with that from ERAI and both WRF simulations	27
3.2 PW correlation maps for both WRF simulations and ERAI compared to MODIS	28
3.3 PW bias maps for both WRF simulations and ERAI compared to MODIS	28
3.4 PW RMSE maps for both WRF simulations and ERAI compared to MODIS	29
3.5 Precipitation correlation maps for both WRF simulations and ERAI compared to EOBS	30
3.6 Precipitation bias maps for both WRF simulations and ERAI com- pared to EOBS	30

3.7	Precipitation RMSE maps for both WRF simulations and ERAI compared to EOBS	31
3.8	Precipitation correlation maps for both WRF simulations and ERAI compared to ECA&D	31
3.9	Precipitation bias maps for both WRF simulations and ERAI compared to ECA&D	32
3.10	Precipitation RMSE maps for both WRF simulations and ERAI compared to ECA&D	32
3.11	Precipitation correlation maps for both WRF simulations and ERAI compared to TRMM	33
3.12	Precipitation bias maps for both WRF simulations and ERAI compared to TRMM	33
3.13	Precipitation RMSE maps for both WRF simulations and ERAI compared to TRMM	34
3.14	Precipitation correlation maps for both WRF simulations and ERAI compared to GPCP	34
3.15	Precipitation bias maps for both WRF simulations and ERAI compared to GPCP	35
3.16	Precipitation RMSE maps for both WRF simulations and ERAI compared to GPCP	35
3.17	Distribution of the land uses defined by the NOAH LSM across the IP	37
3.18	Problematic points eliminated from the validation of evaporation . . .	37
3.19	Differences between GLEAM v3.0b and v3.0c	38
3.20	Evaporation correlation maps for GLEAM v3.0b	39
3.21	Evaporation bias maps for GLEAM v3.0b	39
3.22	Evaporation RMSE maps for GLEAM v3.0b	40
3.23	Areal mean evaporation for period 2010-2014	41
3.24	Areal mean analysis of the terms of the water balance	42
3.25	Daily and seasonal distribution of the areal mean of the residual . . .	43
3.26	Analysis minus background of the specific humidity at 2 m	45
3.27	Analysis minus background of the specific humidity near 875 hPa . . .	45
3.28	Analysis minus background of the temperature at 2 m	46
3.29	Mean daily evaporation during winter and summer for the D experiment	47
3.30	Accumulated annual precipitation maps for the D experiment, EOBS and ECA&D	47
3.31	Seasonal variability of mean daily PW	48
3.32	Daily analysis of the transboundary moisture fluxes for winter	49
3.33	Daily analysis of the transboundary moisture fluxes for summer	49

Chapter 4: Comparison of Downscaling Precipitation Models **51**

4.1	Distribution of the R2 values obtained for each SDSM experiment and both predictors suites.	54
4.2	Taylor diagrams for each SDSM experiment on Lisbon station	55
4.3	Taylor diagrams for each SDSM experiment on Cáceres station	56

4.4	ROC curves for each SDSM experiment on Lisbon station	57
4.5	ROC curves for each SDSM experiment on Cáceres station	57
4.6	Distribution of the ROC curves for the 21 stations over the IP	58
4.7	Regions defined for the comparison of downscaled precipitation	59
4.8	SDSM predictor suite designed for the E79r experiment	60
4.9	Distribution of the R2 achieved by the E79r experiment	62
4.10	Taylor diagram for Gijón, representative of the Northern region	63
4.11	Taylor diagrams for the stations representative of the Central region	64
4.12	Taylor diagrams for the stations representative of the Mediterranean region	65
4.13	Taylor diagrams for the stations representative of the Southwestern region	66
4.14	Distribution of the correlations obtained after the bootstrap technique	67
4.15	Distribution of the LEPS scores for the chosen stations	68
4.16	Distribution of the BSS scores for the chosen stations	69
4.17	Distribution of the chosen precipitation indices	70
Chapter 5: Applications		73
5.1	Taylor diagrams comparing buoy wind data with that from ERAI and both WRF simulations	75
5.2	Correlation, RMSE and SD ratio maps for both WRF experiments and ERAI compared to CCMPv2	76
5.3	Detailed map of the studied area showing the regions for potential wind farms	77
5.4	Wind roses for the Cabo Begur and Mahon buoys	78
5.5	Annual and seasonal capacity factor maps for the low turbine	79
Chapter 6: aiRthermo		81
6.1	Example of a Stüve diagram obtained with <i>aiRthermo</i>	86
Appendices		103
A.1	Predictor suite created for N48 experiment	106
A.2	Predictor suite created for E79 experiment	107
A.3	Predictor suite created for N79 experiment	108
A.4	Predictor suite created for E79r experiment	109
B.1	Taylor diagrams for the Northern region	112
B.2	Taylor diagrams for the Central region	113
B.3	Taylor diagrams for the Mediterranean region	114
B.4	Taylor diagrams for the Southwestern region	115

List of Tables

Chapter 2: Data and Methodology	7
2.1 Characteristics of the SDSM experiments	20
Chapter 3: Analysis of the Water Balance	25
3.1 Characteristics of the PW regression lines between validation datasets and experiments	26
3.2 Summary table for correlations against precipitation validation datasets	36
3.3 Summary table for bias against precipitation validation datasets . . .	36
3.4 Summary table of correlation against GLEAM v3.0b and v3.0c ver- sions (with and without the urban points)	40
3.5 Summary table of bias against GLEAM v3.0b and v3.0c versions (with and without the urban points)	41
Chapter 4: Comparison of Downscaling Precipitation Models	51
4.1 Number of times that each predictor was used on each region	61
Chapter 5: Applications	73
5.1 Summary table for Annual Energy Production at the largest wind farm	80
5.2 Summary table for Annual Energy Production at the smallest wind farm	80

Abbreviations and conventions

We use the following abbreviations throughout the thesis

AEMET Agencia Estatal de Meteorología (Spanish Meteorological Agency)

AEP Annual Energy Production

AUC Area Under the Curve

BSS Brier Skill Score

CCMPv2 Cross-Calibrated Multi-Platform Dataset

CF Capacity Factor

CRAN Comprehensive R Archive Network

EA East Atlantic Oscillation

ECA&D European Climate Assessment & Dataset project

ECMWF European Centre for Medium-Range Weather Forecasts

EL End Level

ENSO El Niño - Southern Oscillation
ERA-Interim ERA-Interim Reanalysis
EOBS ENSEMBLES OBSERVATIONS
EOF Empirical Orthogonal Function
GCM Global Climate Model
GLEAM Global Land Evaporation Amsterdam Model
GPCP Global Precipitation Climatology Project
IP Iberian Peninsula
LCL Lifting Condensation Level
LEPS Linear Error in Probability Space
LFC Level of Free Convection
LSM Land Surface Model
MAD Median Absolute Deviation
MARS Meteorological Archival and Retrieval System
MLR Multiple Linear Regression
MODIS Moderate Resolution Imaging Spectroradiometer
NAO North Atlantic Oscillation
NCEP NCEP/NCAR Reanalysis 1
NCL NCAR Command Language
NN Neural Networks
PBL Planetary Boundary Layer
PC Principal Component
PW Precipitable Water
r Pearson's correlation
R² Explained Variance
RBF Radial Basis Function
RCM Regional Climate Model

RMSE Root Mean Squared Error

SDSM Statistical DownScaling Model

SST Sea Surface Temperature

SWG Stochastic Weather Generator

TRMM Tropical Rainfall Measuring Mission

WRF Weather Research and Forecasting Model

1

Introduction

THE Iberian Peninsula (IP) is an attractive region for the study of the atmospheric branch of the water cycle and where different downscaling techniques can be tested. The IP is surrounded by the Atlantic Ocean to the north and west, and by the Mediterranean Sea to the east. This distribution influences every element of the hydrological cycle in the region. The IP is influenced by the large-scale moisture transports associated to the sea level pressure patterns over the Atlantic Ocean (*Fernández et al., 2003; Gimeno et al., 2010; Gómez-Hernández et al., 2013*), but also by the development of convective precipitation in the south-eastern corner of Spain (*Zorita et al., 1992; Rodríguez-Puebla et al., 1998; Fernández et al., 2003*).

Besides these sources of moisture, the IP is also affected by some teleconnection patterns, whose effects can be observed in the atmospheric circulation near North Atlantic area (*Rodríguez-Puebla et al., 2001*). The precipitation extremes in Europe are particularly influenced by the North Atlantic Oscillation (NAO) (*Haylock and Goodess, 2004; Zveryaev et al., 2008*), and the East Atlantic oscillation (EA) determines the location of the storm tracks of the region (*Rodríguez-Puebla et al., 1998; Sáenz et al., 2001; Zveryaev et al., 2008*). The blockings are also responsible of the observed precipitation regimes (*Sousa et al., 2017*). According to the literature, teleconnections with the El Niño - Southern Oscillation (ENSO) have also been reported in the IP, but its effects are not stationary (*López-Parages and Rodríguez-Fonseca,*

2012) and they are restricted to different regions of the IP (*Kiladis and Diaz, 1989; Rodó et al., 1997; Frías et al., 2010; Vicente-Serrano et al., 2011; Lorenzo et al., 2011*). However, the inter-annual variability of precipitation cannot be explained by these factors, and additional factors such as the air temperature or humidity must be taken into account (*Goodess and Jones, 2002*).

Some contrasting climatic regions can be found in the IP, delimited by the combination of the aforementioned mechanisms and the strong topography of the zone. According to recent climate classifications, three big climatic areas are predominant in the region (*Kottek et al., 2006; Peel et al., 2007; Lionello et al., 2012; Rubel et al., 2017*): Arid, Warm Temperature and Snow Climates (B, C and D groups of the Köpen-Geiger climate classification respectively). However, depending on the humid and dry seasons, the Warm temperature group can be divided into two subgroups (Cf and Cs respectively). Then, four climate regions can be defined: (1) Arid climate mainly in the south of the IP, but also near the Ebro basin; (2) Mediterranean, in the southwestern corner; (3) Oceanic, observed mainly in the north of Spain and Portugal; Finally, (4) Alpine, in some mountain ranges such as the Pyreness, Sierra Nevada or Picos de Europa.

As a result of all of these factors, the observed precipitation patterns over the IP change from one season to another. During winter, the north and the west receive great amounts of precipitation. In contrast, the most important season for the east and south is autumn (*Rodríguez-Puebla et al., 1998; Esteban-Parra et al., 1998; Romero et al., 1999*). According to *Tullot (2000)*, the precipitation affects the centre of the IP mainly in spring. Nowadays, a decrease in the amount of precipitation measured in the IP has been reported by some studies (*Rodríguez-Puebla et al., 1998; Paredes et al., 2006*), but it can be extended to the entire Mediterranean basin (*Trigo et al., 1999; Quadrelli et al., 2001*). *Vicente-Serrano et al. (2014)* stated that this reduction is also significant in the relative humidity, but not in the specific humidity.

The distribution of the Precipitable Water (PW) also varies along the year and the region. During winter, the largest values are located near the oceanic or marine regions. In contrast, the most remarkable values are observed near the Mediterranean coast in summer (*Zveryaev et al., 2008*). Furthermore, *Ortiz de Galisteo et al. (2011)* pointed out that the diurnal cycle of the PW can be modified by local effects such as the breezes.

These precipitation and PW studies can be included inside an evaluation of the water balance over a certain region. Nowadays, this topic has become really popular in the field as a result of the scarcity of water predicted by climate change simulations (*Iglesias et al., 2007; Bangash et al., 2013; Gampe et al., 2016*). During the last decades, a growing number of studies have been carried out focusing on the study of the water balance over different regions and following different methodologies (*Gutowski Jr. et al., 1997; Trenberth and Guillemot, 1998; Berbery and Rasmusson, 1999; Trenberth et al., 2007; Yeh and Famiglietti, 2008*). Over the IP, *Vérant et al. (2004)* studied the terrestrial water balance for different resolutions of regional simulations. Thus, it is clear that the resolution of the actual reanalyses is not enough to carry out this kind of studies and that high-resolution regional simulations must

be created.

Regional Climate Models (RCM) were firstly developed during the 1990s in order to improve the coarse spatial resolution of Global Climate Models (GCMs). Nowadays, two main techniques coexist: the statistical and the dynamical downscaling. The first is based on empirical relationships between local weather and large-scale variables (*von Storch et al., 1993*). The later is based on the numerical integration of the equations driving the energy, momentum, mass and moisture balances of the atmosphere (*Giorgi, 2006; von Storch, 2006*).

On the one hand, several statistical downscaling methods exist, and they are known to have limitations on their performance. Some studies suggest that highly non-linear techniques such as the Radial Basis Function (RBF) Neural Networks (NN) can perform equally to the linear models (*Weichert and Bürger, 1998; Trigo and Palutikof, 2001*). A search of analogues in the space of the canonical correlation coefficients showed good results in *Fernández and Sáenz (2003)*, and the analogues technique followed by a bias-correcting heuristic formula were used for precipitation downscaling in *Timbal and Jones (2008)*. According to *Goodess et al. (2007)*, some statistical models are more skilful at reproducing the persistence of rainfall more than the frequency of rain, but sometimes they cannot even reproduce extreme daily precipitation amounts. However, the performance of the models is better in the mid-latitudes (*Cavazos and Hewitson, 2005*) and during winter (*Timbal and Jones, 2008; Yang et al., 2010*). Normally, the correlations between the observed and predicted precipitation is about 0.5 if the daily amount is taken into account, but they can reach 0.7 for monthly data. Over the IP, these scores were obtained by the analogues technique, outperforming the NN (*Zorita and von Storch, 1999*). Over the Ebro Valley (*Ibarra-Berastegi et al., 2011*), a comparison of different precipitation downscaling techniques such as machine learning algorithm random forest (RF), a classical Multiple Linear Regression (MLR) model and analogues showed that the RF and the MLR cannot significantly improve the results obtained by the analogues. The Statistical DownScaling Model (SDSM) (*Wilby et al., 2014*), which combines a MLR model and an Stochastic Weather Generator (SWG), shows good estimates of daily temperature (*Liu et al., 2007*), total precipitation (*Wetterhall et al., 2006, 2007*) and areal rainfall (*Hashmi et al., 2011*). However, the extreme precipitation events are less reliable during the dry seasons (*Wilby and Dawson, 2013*).

On the other hand, the dynamical downscaling is performed by the RCMs. It is generally accepted (*Jones et al., 1995; Foley, 2010; Rummukainen, 2010; Feser et al., 2011; Önol, 2012*) that a RCM, a dynamical model nested within a Global Climate Model (GCM), is able to generate more accurate climate simulations than the GCM itself. In addition, some studies (*Rockel et al., 2008; Leung and Qian, 2009*) have stated that even if the RCMs are only fed by the coarse boundary conditions from a GCM, they are able to simulate the small-scale features related to the surface such as floods or orographic precipitation. One of the most popular RCM is the Weather Research and Forecasting Model (WRF, ARW) (*Skamarock et al., 2008*), and it has been widely used in several kind of studies. For example, WRF was used for the study of daily precipitation after changing the resolution of the domain in *Cardoso et al.*

(2013) or for the analysis of evapotranspiration and precipitation over the IP during spring (*Rios-Entenza et al., 2014; Eiras-Barca et al., 2016*). The moisture recycling was also studied with WRF in *Rios-Entenza et al. (2014)*. As part of the EURO-CORDEX initiative, an ensemble of regional models were used to identify possible impacts on temperature and precipitation under the climate change conditions over Europe (*Dosio, 2016*), Portugal (*Soares et al., 2015*) or Spain (*Domínguez et al., 2013*).

Nevertheless, many of the current studies developed with WRF still do not include the data assimilation technique. Focusing on the IP, the number of studies including this methodology is very small. Apart from our group in previous studies (*Ulazia et al., 2016, 2017*), the most similar integration that has been found in the literature for this region is that carried out by the Spanish Meteorological Agency (AEMET) using the HIRLAM model (*Navascués et al., 2013*). The 3DVAR data assimilation step is included every six hours, showing a positive effect on the forecast quality. However, it has not been applied to the study of any term of the water balance, or even compared to another simulation created with the same configuration but without the data assimilation scheme. Furthermore, the resulting products include better resolution than the actual reanalyses and comparable resolution to other precipitation products such as Spain02 (*Herrera et al., 2012, 2016*).

Additionally, a large number of comparisons between dynamical and statistical downscaling can be found in the literature (*Fowler and Wilby, 2007; Schmidli et al., 2007; Gutmann et al., 2012; Casanueva et al., 2016*). These studies show that comparable skill at simulating the present climate is observed for both downscaling techniques (*Wilby et al., 2000; Haylock et al., 2006; Osmá et al., 2015; Casanueva et al., 2016*), but there is still considerable scope to further research about this topic, particularly on the decisions involved in the set-up of the downscaling models. This could include the different sources and spatial resolutions for the driving boundary conditions used in the numerical models or for the predictors included in the statistical models; The optimal set of predictor variables or the record length used during the calibration of the statistical model on a site-by-site basis; whether to use or not the data assimilation scheme while simulating past climates; the diagnostics for assessing downscaling model skill and value-added to coarser resolution GCM inputs. As far as the authors know, there has been only one previous direct comparison between SDSM and WRF for China (*Tang et al., 2016*), and the WRF simulations created for that study did not include data assimilation.

1.1 Objective

Taking all of the above mentioned information into account, our main objectives are to extend the previous studies to a full analysis of the whole atmospheric branch of

the water cycle over the IP, and to analyse the daily precipitation downscaled by the statistical model SDSM and by two different configurations (with and without 3DVAR data assimilation) of the dynamical Model WRF.

In particular, an evaluation of the ability to simulate a realistic water balance over the IP by WRF model will be tested. The advantages or disadvantages of including the 3DVAR data assimilation step while running the WRF model will be also evaluated. To do so, two simulations were carried out for period 2009-2014: one of them was configured so that only the boundary conditions drive the model after the initialization (the N experiment). The same configuration was used on the second one, but included 3DVAR data assimilation every six hours (the D experiment). Neither the climatology nor the interannual variability of both experiments will be studied as five years of simulations are not enough to do so. Firstly, each term of the water balance was independently compared against observational datasets (particularly PW, precipitation and evaporation). Secondly, the closure of the balance was calculated according to the model results in order to check the consistency of the fields. Thirdly, the comparison between both WRF simulations was carried out. In all of these phases, the results for the ERA-Interim reanalysis (hereafter, ERAI) (*Dee et al., 2011*) were included in order to check if the high-resolution products created are able to outperform the driving reanalysis, thus adding value to it.

In order to be able to fairly compare both statistical and dynamical downscaling techniques, a configuration as similar as possible to that used in WRF was designed for the SDSM. ERAI data were used for the creation of the predictor variables necessary for the calibration of the SDSM model. The analysis was carried out on a site-by-site basis, on twenty-one stations evenly spaced over the IP and representative of the different climates observed in the region. Data from ERAI and some observational datasets were included on the comparison of both downscaling techniques. As the SDSM produces a twenty-member ensemble, this probabilistic output cannot be compared directly with the deterministic data from WRF. Thus, for the comparison, the mean of the ensemble will be taken as an independent experiment, but also each member of the ensemble. Several metrics and precipitation indices were calculated for the evaluation of the best downscaling technique.

1.2 What you will find in this thesis

This thesis is structured in eight main chapters. In chapter two, a detailed description of the main characteristics of every dataset used in this thesis is provided. The domain and the physics parametrizations used to configure the WRF model are also presented there, along with a description of the postprocessing applied to the model's raw output. Every tested configuration of the SDSM is listed in this chapter, but also the predictor variables created from the ERAI data. It also includes a detailed

description of every metric and precipitation index used in the evaluation of the water balance and both downscaling techniques.

In chapter three, the evaluation of the water balance over the IP for period 2010-2014 is presented. Firstly, the validation against observational datasets of the PW, precipitation and evaporation is carried out. The closure of the water cycle is evaluated by means of the residual of both WRF simulations. The calculation of the analysis increments produced by the data assimilation step are also studied in this chapter. It concludes describing the main features observed in the water balance simulated by the best experiment.

In chapter four, the statistical and dynamical downscalings are compared on a site-by-site basis in twenty-one stations over the IP. This work was carried out during two placements of three-and-a-half and two months long in the Department of Geography at Loughborough University, under the supervision of Prof. Robert L. Wilby. Firstly, different experiments designed to determine the optimal configuration of the SDSM are evaluated. Once the similar configuration to that from WRF is determined, both downscaling techniques are compared to some observational datasets. The evaluation is not only carried out taking into account correlation-based metrics, and also some precipitation amount and occurrence indices are also included.

In chapter five, a direct application of both WRF simulations is presented. An evaluation of both simulations and ERAI over the Western Mediterranean sea is carried out, comparing the simulated wind field at 10 m with that measured in the region. Once the best experiment is determined, it is applied to the calculation of some metrics related to wind farms.

In chapter six, a detailed description of the methodology followed and the functions included in an R-package created as a result of the calculations made during this thesis is presented. This package is publicly available on the Internet and it can be used for the calculation of thermodynamic variables or for plotting the evolution of air parcels.

In chapter seven, the discussion about some results presented in this thesis is carried out. It will focus on the set-up of both downscaling models and in some issues observed with the observational datasets. It will also provide further insight on the results.

Finally, the last chapter will provide a summary of the key findings of this thesis, along with future perspectives that could follow the topics developed in this thesis.

2 Data and Methodology

THIS chapter presents a detailed description of every dataset that was used in the different studies included in the thesis. They can be separated in three big groups: (1) data downloaded from the Internet for validation purposes, (2) data created by using the WRF model and (3) data created by making use of the SDSM. The raw data created by the dynamical and statistical downscaling models were also postprocessed. How this step was carried out is also detailed here. Finally, a description of every validation technique applied in the thesis is presented.

2.1 Datasets

Every dataset used in this thesis is listed in this section:

- **ERA-Interim Reanalysis:** Two different versions of ERAI data were downloaded from the Meteorological Archival and Retrieval System (MARS) repository at ECMWF, according to its spatial resolution: one at 2.5° and another at

0.75°. Its vertical levels are defined as a terrain-following hydrostatic-pressure coordinate, spanning the atmosphere from 0.1 to 1012.05 hPa in 60 model levels. The data are provided every 6 hours, but most of the times they are aggregated to daily or monthly values. Some data at the original model levels were used for the creation of the predictors for the SDSM. However, the data were also interpolated to several vertical levels in order to provide the boundary and initial conditions in both WRF simulations. This interpolated data was also used for the validation of the experiments.

- **PREPBUFR data:** This dataset includes observations from the NCEP ADP Global Upper Air and Surface Weather Observations. Particularly, it is referenced as *ds337.0*¹. Reports from different sources such as aircrafts, wind profilers, land (Synoptic and Metar), ships, buoys and scatterometers are included. This dataset is used as the provider of observations for the data assimilation step within the WRF model.
- **SST data:** High-resolution ($0.25^\circ \times 0.25^\circ$) daily sea surface temperature (SST) fields from NOAA OI SST v2 (*Reynolds et al., 2007*) were included in both simulations.
- **ECA&D dataset:** The European Climate Assessment & Dataset project (ECA&D) (*Klein Tank et al., 2002*) includes daily precipitation data from land stations. Twenty-one stations evenly spaced over the IP and representative of the different climatic areas were selected (coloured red in Figure 2.1), but without oversampling over some areas (such as Catalonia) where the density of available stations is much higher than in the rest of the domain. Fourteen stations were available for Portugal, but only Lisbon had records during the validation period (2010-2014, same period as for our both WRF simulations). The precipitation amount observed on these stations were used as predictands for the SDSM and as validation for precipitation.
- **NCEP/NCAR Reanalysis:** The NCEP/NCAR Reanalysis 1 data are included in the thesis as the source of predictors for the SDSM. A postprocessed version of the data were downloaded from the SDSM portal². Once a latitude and longitude is given, the predictor set available for the nearest point in the reanalysis grid is returned by the website.
- **Radiosonde data:** Atmospheric radiosondes were obtained from the server of the University of Wyoming³ in order to validate the PW. Only eight stations were available for the IP (see Figure 2.2). In these stations, data are collected twice per day (at 00 UTC and 12 UTC), except for Lisbon station where it is only available once per day (at 12 UTC).

¹Available in <https://rda.ucar.edu/datasets/ds337.0/>

²Downloadable from: <http://co-public.lboro.ac.uk/cocwd/SDSM/data.html>

³Publicly available in: <http://weather.uwyo.edu/upperair/sounding.html>

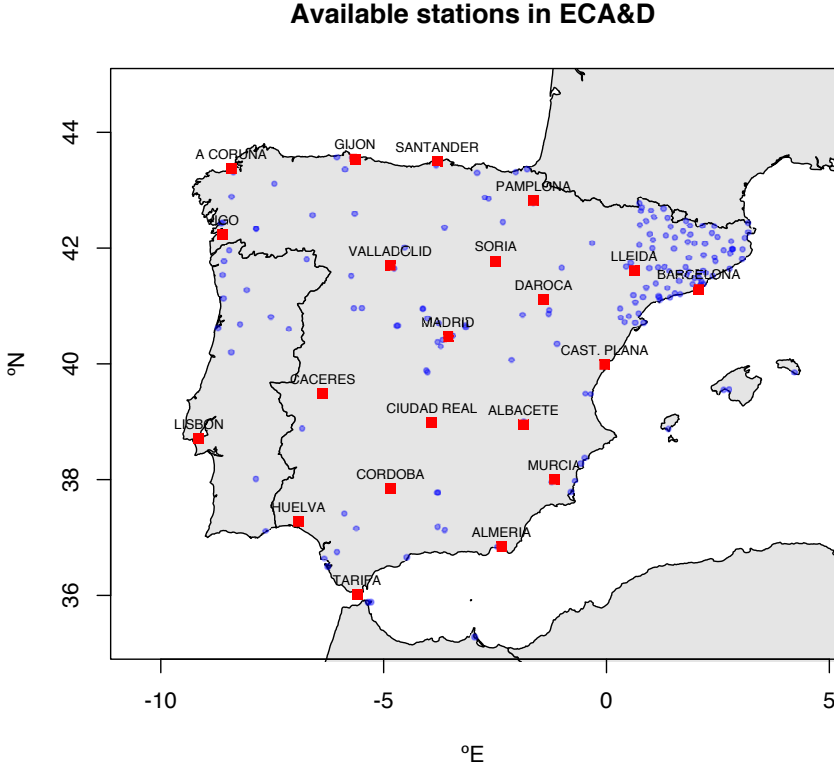


Figure 2.1: Location of all available stations in the ECA&D dataset for the IP (blue dots) along with the chosen twenty-one stations in the study (red squares).

- **MODIS data:** Moderate Resolution Imaging Spectroradiometer (MODIS) data ([Gao and Kaufman, 2003](#)) were used as PW validation dataset. The MODIS data are collected every one to two days in many spectral bands by a spectroradiometer aboard the Aqua and Terra satellites. For our validation, Level-2 PW from both satellites were combined and used in order to improve the temporal resolution of the data. $5 \times 5 \text{ km}^2$ spatial resolution was defined in a domain centred over the IP ($34^\circ\text{-}46^\circ\text{N}$, 12°W - 6°E).
- **ENSEMBLES Observations:** The version 12.0 of the ENSEMBLES OBSERVATIONS (EOBS) dataset ([Haylock et al., 2008](#); [van den Besselaar et al., 2011](#)) was downloaded. This dataset presents a 0.25° grid and a daily temporal resolution. It was used as a precipitation validation dataset for WRF and SDSM.
- **TRMM dataset:** The Tropical Rainfall Measuring Mission (TRMM) data ([Wang et al., 2014](#)) were used as a validation dataset for precipitation. Three-hourly precipitation data are included at a 0.25° spatial resolution. In order to

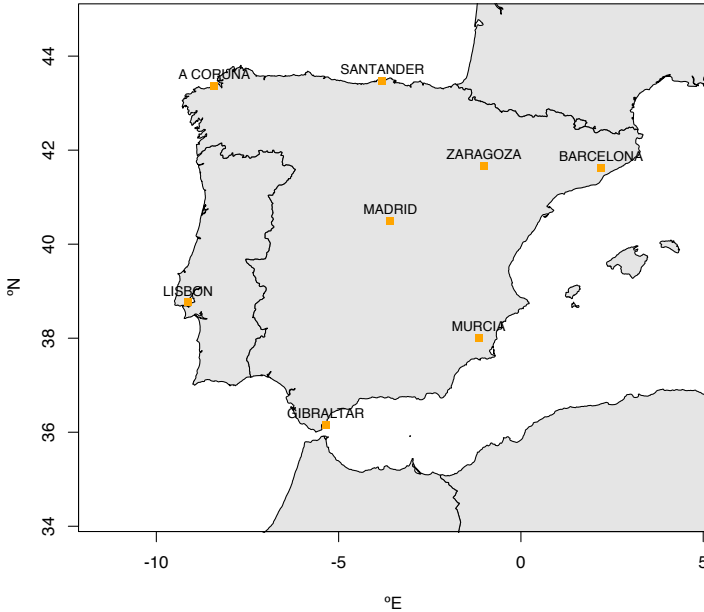


Figure 2.2: Location of all available radiosondes in the server of the University of Wyoming for the IP (orange squares).

compare them with the other precipitation datasets, the data were aggregated to daily values.

- **GPCP data:** The Global Precipitation Climatology Project (GPCP) ([Huffman et al., 2001](#)) data were included in our study to validate the precipitation obtained by WRF and SDSM. It includes daily precipitation data at a 1° horizontal resolution.
- **GLEAM dataset:** Version 3.0 of the Global Land Evaporation Amsterdam Model (GLEAM) dataset ([Martens et al., 2017](#); [Miralles et al., 2011](#)) was used in our study. This dataset is based on observations such as radiation, air temperature, precipitation, snow water equivalent, vegetation optical depth and surface soil moisture from satellites, reanalysis and other observational fields. Three independent GLEAM datasets were available, but only two of them were selected for this study: v3.0b and v3.0c. GLEAM v3.0a dataset was not included in the validation because the net radiation and air temperature used as forcings on it are provided by ERAI. Both selected versions were driven only by satellite data, and the main difference between them was that v3.0c retrieved vegetation optical depth and surface soil moisture from SMOS-observations. Both datasets covered the same domain (50°N - 50°S) using a $0.25^\circ \times 0.25^\circ$ regular grid. GLEAM data are available with daily temporal resolution, and they were used to validate WRF's evaporation.

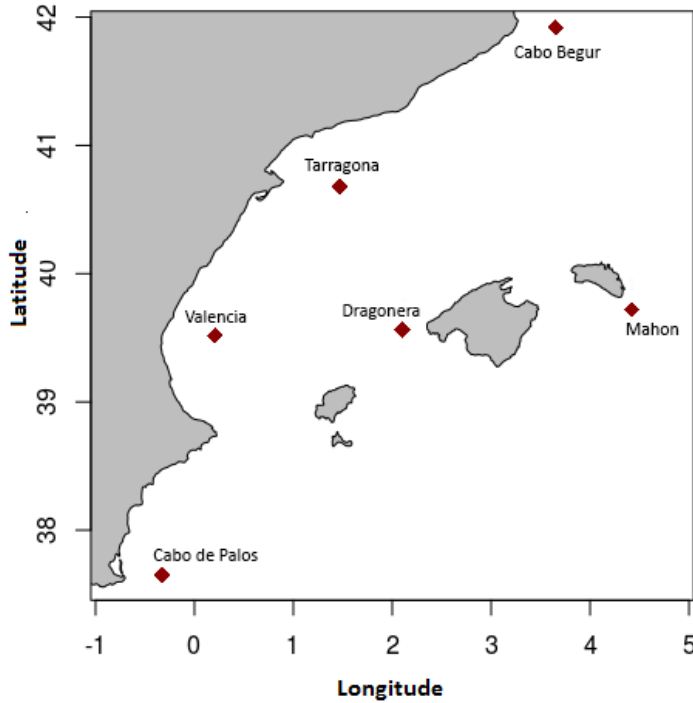


Figure 2.3: Location of the six buoys used for the validation of wind at 10 m over the west Mediterranean.

- Buoy data:** Wind speed (direction and magnitude) data measured by buoys operated by the Spanish State Ports Authority (Puertos del Estado) were downloaded from their public website¹. The six chosen buoys are presented in Figure 2.3. The data are provided hourly and at a height of three meters above the sea level. They were used for the validation of simulated wind over the West Mediterranean region in chapter 5.
- CCMPv2 dataset:** The second version of the Cross-Calibrated Multi-Platform (CCMPv2) dataset (*Atlas et al., 2011*) was included in our study for the evaluation of the spatial wind outputs created by both WRF simulations (see chapter 5). This dataset was created combining radiometer-measured wind speeds, scatterometer wind vectors and moored buoy data by means of a variational data assimilation algorithm that uses ERAI wind fields as background or first guess. It includes six-hourly data at a 0.25° horizontal resolution.

¹Data publicly available at this website: <http://www.puertos.es/en-us/oceanografia/Pages/portus.aspx>

2.2 Dynamical Downscaling Simulations

Two simulations spanning the period 2010-2014 were created using version 3.6.1 of the WRF model, released on August 14, 2014. Both runs were started in 2009, but this first year was designed as spin-up for the Land Surface Model (LSM), as done in previous studies such as [Argüeso et al. \(2011\)](#) and [Zheng et al. \(2017\)](#). The WRF model was nested inside ERAI, which provides the boundary and initial conditions every 6-hours. These boundary conditions drive the model after the initialization in the first simulation (hereafter, the "N" experiment). The second experiment (hereafter, "D") is configured the same way as N, but 3DVAR data assimilation ([Barker et al., 2012](#)) is run every six hours using observations from the PREPBUFR dataset. Only the observations included inside a 120-minute window centered at these analysis times (00, 06, 12 and 18 UTC) are included in the 3DVAR data assimilation step.

The domain is centered on the IP but it also covers much of north-west Africa and western Europe (20°-60°N, 25°W-15°E) (Figure 2.4). Being quite large, the literature for similar cases ([Jones et al., 1995](#); [Rummukainen, 2010](#)) indicates that the results should not be affected by border effects and that meteorological features are allowed to develop freely over the region. A mask over the IP (coloured in red in Figure 2.4) was defined in order to select the points that were included in the analysis of the water balance (2108 grid points in total). Normal vectors were also defined at its boundary, so that positive vectors are defined outwards the mask. Both N and D simulations had 51 vertical levels and 15x15 km² horizontal resolution. With this resolution, the WRF model is able to reproduce the topography of the IP in a better way than ERAI. The distribution of the mountain ranges in the WRF grid is quite similar to that in the GLOBE dataset (bottom right and left panels of Figure 2.4 respectively).

An important part of the design of a experiment to be run by any RCM is to choose the parameterizations that will impose the physics of the model. A good simulation will be intrinsically conditioned by how these parameterization schemes work together, as some variables (e.g. precipitation or surface fluxes) depend on their interactions (Figure 2.5). In both simulations, the NOAA LSM ([Tewari et al., 2004](#)) calculates the soil temperature and moisture in four soil layers, but also the fractional snow cover and the frozen soil. The long-wave radiation scheme RRTMG ([Iacono et al., 2008](#)) is used to compute the clear-sky and cloud upward and downward radiation fluxes in the model, considering each layer in the atmosphere and the surface emissivity according to the land-type in the LSM. The short-wave radiation scheme RRTMG ([Iacono et al., 2008](#)) computes the clear-sky and cloudy solar fluxes, and includes the annual and diurnal solar cycles. Both radiation schemes interact with the model's cloud field, and the cloud fraction is calculated by Xu-Randall method ([Xu and Randall, 1996](#)), based on relationships between stratiform cloud amount and its large-scale predictors. The SST is updated daily and the monthly albedo value is also taken into account. The purpose of the MYNN2 Planetary Boundary Layer

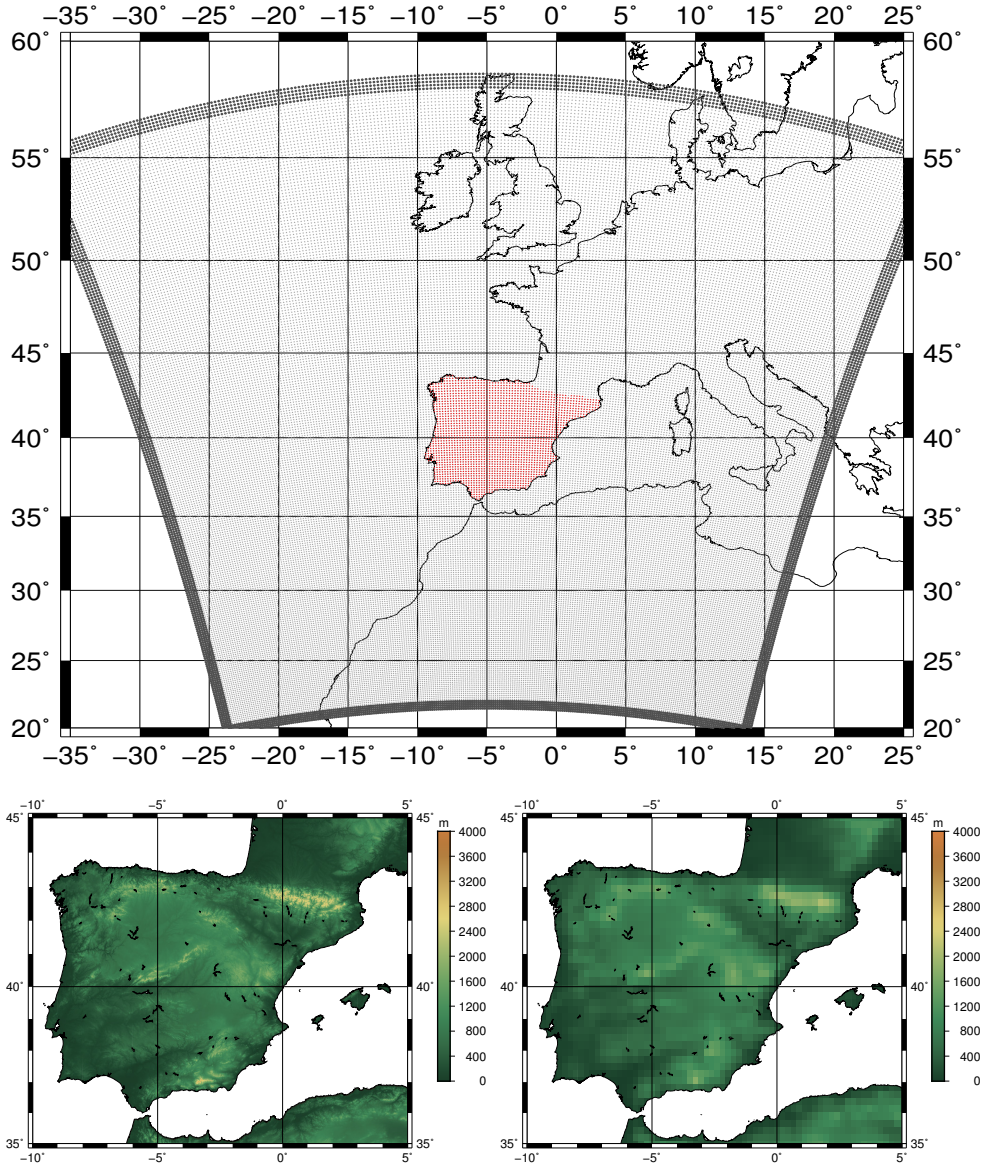


Figure 2.4: Top: Domain of both simulations marked with grey dots. The mask defined for the IP is plotted in red. Bottom left: topography of the IP taken from GLOBE dataset (at 1 km resolution; *Hastings and Dunbar, 1999*) and bottom right: topography as represented in our WRF simulations (15 km resolution).

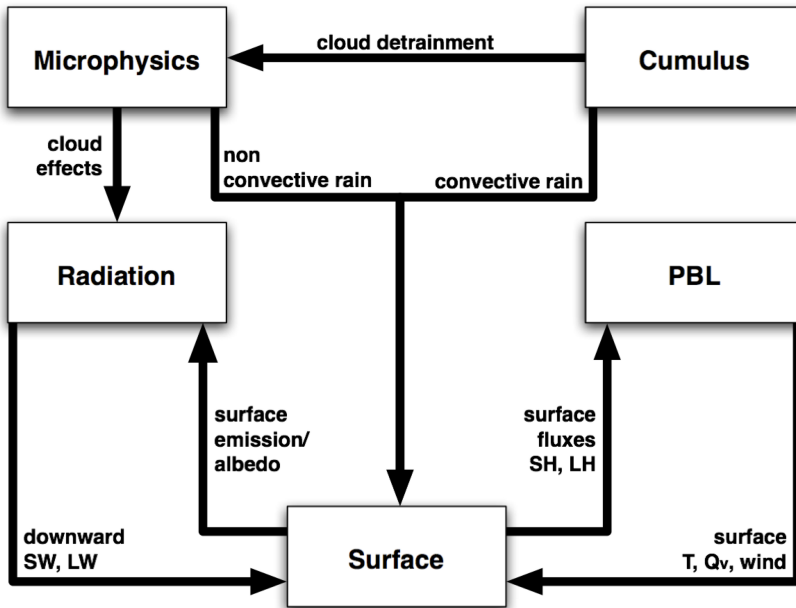


Figure 2.5: Direct interactions between the parameterization schemes inside the WRF model. Taken from the slides presented at the July 2015 Basic WRF Tutorial in Boulder, Colorado (Retrieved on September 17, 2015 from http://www2.mmm.ucar.edu/wrf/users/tutorial/tutorial_presentation_summer_2015.html).

scheme (*Nakanishi and Niino, 2006*) is to distribute surface fluxes with the boundary layer eddy fluxes, where the horizontal diffusion acts along model levels. The cumulus are parameterized by the Tiedtke scheme (*Tiedtke, 1989; Zhang et al., 2011*), which redistributes the air in the surface until the top of the column and allows both deep and shallow convection. Finally, the WRF five class microphysics (WSM5) scheme (*Hong et al., 2004*) is used, which simulates the interactions between water vapour and different cloud particle types (cloud water, ice crystals, raindrops and snow). Hail is not included as it is not necessary for spatial resolutions higher than 10 Km.

Before starting the D experiment, its background error covariance matrices were generated. These matrices describe the covariances of the forecast errors of the numerical weather forecast model, and determine how the information provided by the observations is going to be spread to the nearby grid-points and levels of the model. They were generated for the region and the physical parameterizations used by means of the CV5 option in WRFDA (*Parrish and Derber, 1992*). To do so, a 13-month long run from January 2007 until February 2008 was created. The background error covariances vary monthly and were always built using 90 days around the corresponding month. Integrations used during this 90 day period were initialized either at 00 UTC or at 12 UTC in order to properly sample day and night. For

example, the background error covariance matrix for January was created using the data from December to February, and so on for the rest of the monthly varying background error covariance matrices.

The structure of both simulations is the final key aspect of modelling. On the one hand, the N experiment is created by running six-hour long segments that are restarted from the restart file produced by the previous segment (top panel of Figure 2.6). This methodology is equivalent to a continuous WRF run where boundary conditions feed the model every 6-hours after the initialization of the model in January 1st, 2009. The outputs are saved every three hours. On the other hand, the data assimilation experiment (D) is run during twelve hours starting from every analysis time (00, 06, 12 and 18 UTC) (bottom panel of Figure 2.6). For this simulation, there is only a cold start in January 1st, 2009. The analyses are produced by using the output from the model at a six-hour forecast step from the previous segment as first guess in a 3DVAR data assimilation scheme where observations from PREP-BUFR files are used. The same recording frequency for outputs is used for the D experiment, which means that analysis (00, 06, 12 and 18 UTC) and 3-hour forecasts (at 03, 09, 15 and 21 UTC) are included in our results.

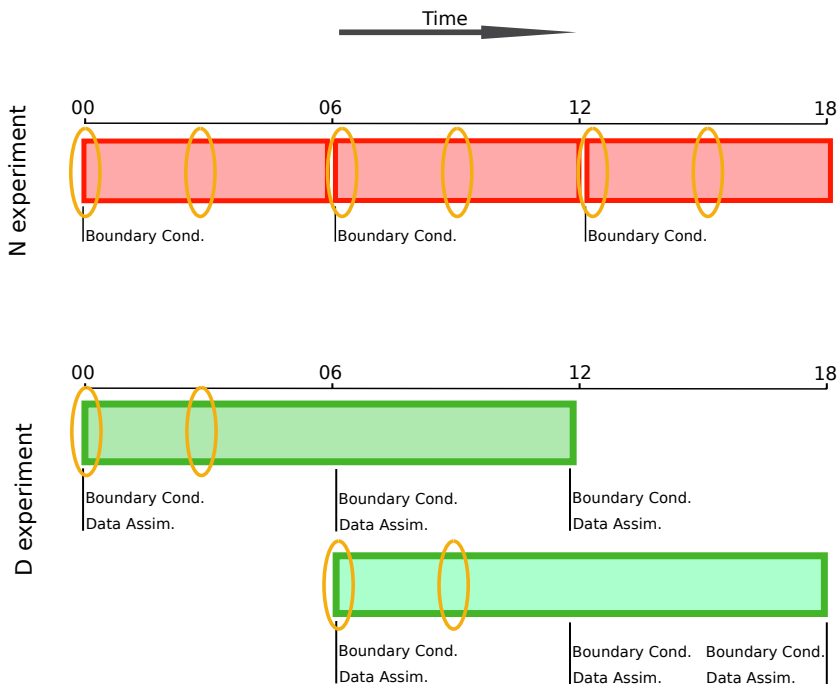


Figure 2.6: Structure of the segments created for the N experiment (top) and for the D experiment (bottom). The orange ellipses mark the recording frequency of the outputs that are used in the postprocessing.

Apart from these two WRF runs, another two were created. One of them, called the S experiment, includes the same configuration as the N experiment but without the NOAA LSM. The other one is called the C experiment and it includes the same configuration as the D experiment, that is, including the data assimilation step but without the Noah LSM. These both experiments would help us to understand the effect of the LSM in the WRF simulations. However, the results of these experiments will not be included in this thesis.

2.3 Postprocessing the Model Outputs

Once both WRF runs were finished, the raw output from the model was postprocessed. The variables cannot be used directly as they are stored by the model since most of them are calculated on model's vertical levels and not on pressure levels. Moreover, some other diagnostic variables must be calculated as they are not included by default in model's output (e.g. evaporation). Depending on their characteristics, the postprocessing will be different. These are the variables that were created during the postprocessing:

- **Temperature [T]:** The temperature field was calculated at 850, 700, 500, 300 and 200 hPa in degrees Kelvin. It was derived from potential temperature and pressure at model's levels according to the definition of the potential temperature in *Tsonis (2002)* and then, interpolated to that pressure levels using the NCAR Command Language (NCL).
- **Specific humidity [SHUM]:** The specific humidity was calculated from the water vapour mixing ratio [QVAPOR] in kg/kg and transformed into the above mentioned pressure levels by NCL.
- **Zonal and meridional wind [U, V]:** Zonal and meridional components of wind were calculated at mass points of the original vertical levels in m/s and then, extrapolated to the selected pressure levels by NCL.
- **Geopotential height [Z]:** The geopotential height corresponding to 850, 700, 500, 300 and 200 hPa is calculated in m using NCL.
- **Vertically integrated zonal and meridional moisture transport [Qx, Qy]:** The zonal and meridional components of the moisture transport were obtained by means of the vertical integration of the specific humidity and zonal/meridional wind product (calculated in mass points). Both are measured in $kg/(ms)$.
- **Vertically integrated zonal and meridional condensed moisture transport [Qcx, Qcy]:** The zonal and meridional components of the condensed

moisture transport were obtained by calculating the product between specific humidity of the condensed particles (cloud water [QCLOUD], ice crystals [QICE], rain drops [QRain] and snow [QSNOW]) and zonal/meridional wind in mass points, and then, integrating along the vertical axis. Both are measured in $kg/(ms)$.

- **Precipitable water column [PW]:** The precipitable water column was calculated by the vertical integration of the specific humidity at the original model levels, and it is measured in kg/m^2 .
- **Condensed precipitable water column [PWc]:** The condensed precipitable water column (in kg/m^2) was calculated by the vertical integration of the specific humidity of the condensed particles at the original model levels.
- **Total precipitation [Rain]:** The total precipitation in $kg/(m^2s)$ was calculated by the sum of the convective precipitation [RAINc] and the non-convective precipitation [RAINnc]. It is an accumulative field, so the value on each time-step is computed as the difference between the next time-step minus the current one.
- **Evaporation [EVAP]:** The evaporation from the surface was calculated from the latent heat flux [LH] from the model surface. This is also an accumulative field, so it is calculated by means of a forward difference. It is measured in kg/m^2s .
- **Surface heat flux [SHFX]:** The surface heat flux in W/m^2 is calculated as the difference between a time-step and its previous one of the accumulated upward sensible heat flux at surface [ACHFX].
- **Mean Sea Level Pressure [MSLP]** The mean sea level pressure is calculated by NCL in Pa .
- **Other variables:** The terrain height [HGT] in m , the water vapour mixing ratio at 2 m [Q2] in kg/kg , the temperature at 2 m [T2] in Kelvin degrees, the surface pressure [PSFC] in Pa and the zonal and meridional wind at 10 m [U10 and V10] in m/s were taken directly from model's output.

2.4 Statistically Downscaled Model Data

The SDSM model is an statistical downscaling model whose algorithm can be described as a conditional weather generator, as regional variables (called predictors) are used to calculate time-varying parameters in a specific site. The relationships between the local predictand (in our case, daily precipitation amount) and the regional

predictors are determined by a least squares calibration. In this case, the transformation applied to the predictand in order to better match a normal distribution is the fourth root transformation, and the missing variance is replicated by adding white noise. Finally, a 20-member ensemble is generated by the SDSM in order to show its uncertainty. The detailed methodology can be found in *Wilby and Dawson (2013)*.

In order to run the model properly, a series of steps must be followed (Figure 2.7). Each calibration must start by selecting a specific site and by retrieving the longest observed time-series available. Then, the longitude and latitude of that station must be used to select the predictor variables from the nearest reanalysis grid cell. The standard predictor variable set includes: downward shortwave radiation flux, mean sea level pressure, precipitation, near-surface specific humidity, mean temperature at 2 m and geostrophic wind strength, both wind components, geopotential height, vorticity, divergence and relative humidity (all at 500 and 850 hPa). These are the predictor variables typically used in statistical downscaling models (*Cavazos, 2000; Wilby and Wigley, 2000; Schoof and Pryor, 2001*). Once the predictand and the predictor set are calculated, the relationships between them must be explored during

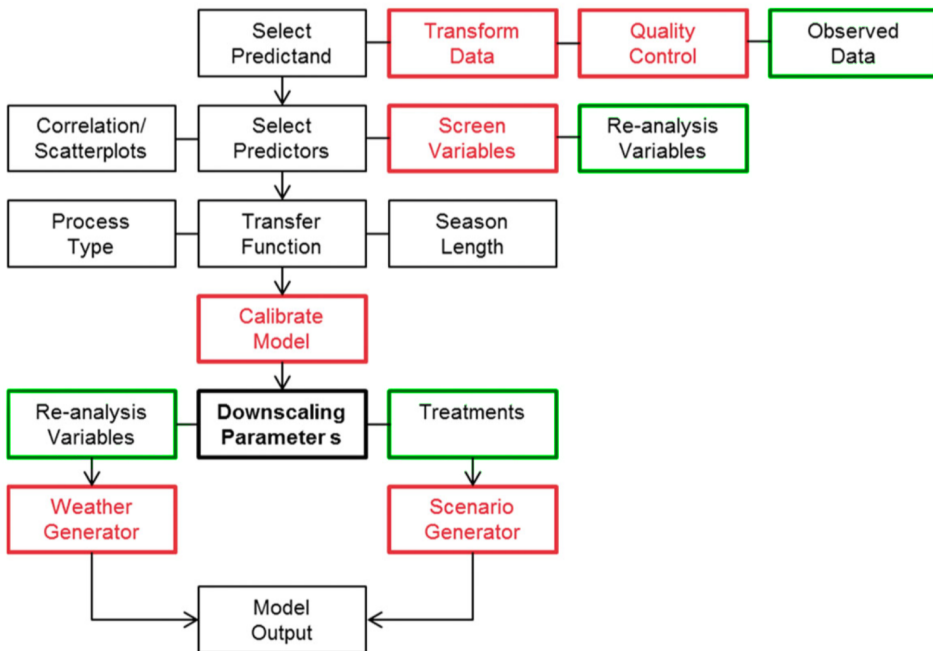


Figure 2.7: Architecture of the SDSM showing every step of it. The color of the boxes shows if inputs are needed (green boxes), if results will appear on the screen (red boxes) or if internal processes are carried out (black boxes). This image is an edited version of that published in *Wilby et al. (2014)*.

a calibration period previously stated. According to those results, the predictors that will be used to calibrate the model must be selected. Finally, the model will create the 20-member ensemble.

During this study, a consistent strategy was adopted to reduce the effect of operator judgements when calibrating the SDSM. First, candidate predictor variables with explained variance (R-squared, R^2) greater than 0.1 (for each month of the monthly analysis calculated by the model) were listed. Second, those with statistically insignificant partial correlation ($p > 0.05$) were eliminated. Finally, the predictor with weakest partial correlation was removed until no predictors with statistically insignificant partial correlation are reported by the SDSM. That means that only predictors with relatively high explanatory power and without multi-co-linearity are chosen. This methodology for the calibration of SDSM is similar to some methods available in the literature (*Wilby et al.*, 1998, 2002; *Gulacha and Mulungu*, 2017). Some of the technical aspects of the calibration have been already largely discussed in other studies such as *Wilby and Wigley* (2000); *Hanssen-Bauer et al.* (2005); *Huth* (2005); *Crawford et al.* (2007); *Mahmood and Babel* (2013, 2014).

We will focus on the previously stated twenty-one stations from the ECA&D dataset (see section 2.1 and Figure 2.1). Daily precipitation totals at these sites were used as the predictand for SDSM. The longitude and latitude of the stations were used to select the predictor variables from the nearest reanalysis grid cell. The predictors from NCEP were downloaded from the SDSM portal. However, the predictors from ERAI were created directly from the reanalysis' raw data.

Both versions of ERAI (at 2.5° and 0.75° horizontal resolution) were postprocessed the same way. Most of the variables were publicly available, but some were created during this postprocessing:

- **Airflow strength at surface, 500 hPa and 850 hPa:** The airflow strength in m/s was calculated as the magnitude of the vector defined by both wind components at each vertical level [U10, V10, U, V].
- **Precipitation:** The precipitation in mm was calculated as the sum of the convective precipitation [CP] and the large-scale precipitation [LSP], as stated by ERAI's developers¹.
- **Near surface relative vorticity:** The near surface relative vorticity is not directly available from ECMWF. In our case, the vorticity [VO] was taken from the level 59 of ERAI's original vertical sigma-levels (according to *Berrisford et al.* (2011), approximately 0.994 if surface is defined as 1).
- **Near surface divergence:** The near surface divergence was defined as the divergence [D] at the original 59th vertical level.
- **Near surface relative humidity:** The near surface relative humidity was calculated from the 2 m dew point temperature [D2] and 2 m temperature

¹see *How are Large Scale Precipitation, Convective Precipitation and Snowfall defined in the ECMWF model?* in ERAI's Frequently Asked Questions (<https://www.ecmwf.int/search/faqs>)

[T2], taking into account the definition of the water vapour pressure (eq. 7.5) in *ECMWF* (2015).

- **Near surface specific humidity:** The near surface specific humidity was calculated from the 2 m dew point temperature [D2] and surface pressure [SP], taking into account the definition of the specific humidity (eq. 7.4) in *ECMWF* (2015).

Different strategies were used to calibrate the version 5.2 (Decision Centric) of the SDSM during the thesis, resulting in four different experiments (Table 2.1). These options are based on the use of NCEP and ERAI for downscaling predictor variables. Two calibration periods were selected according to reanalyses' characteristics: 1948-2009 and 1979-2009. Additionally, two different grid resolutions were used with ERAI, namely 2.5° and 0.75° . Configuring the SDSM model in this way allowed us testing the sensitivity of the results to different calibration periods, predictor sets and resolutions of the coarse-model data. Additionally, the results of the comparison of SDSM versus WRF are more reliable since using different datasets and resolutions for calibration but the same validation period allows deeper understanding of the consequences of the various calibration decisions.

We use a consistent nomenclature to aid comprehension of the large number of model configurations and input permutations. The first letter of the experiment code defines the reanalysis used to create the predictor variables ("N" for NCEP and "E" for ERAI). The following two numbers represent the year when the calibration period begins ("48" for 1948 or "79" for 1979). A final character "r" (as in experiment "E79r") denotes that the spatial resolution of the ERAI data is at 0.75 degrees instead of 2.5. Even if the SDSM was run using two calibration periods (depending on each experiment), the validation period was always the same (2010-2014, the one available in both WRF simulations).

Table 2.1: Characteristics of the experiments used for the analysis of the effect of calibration period, predictors and resolution in the SDSM model.

Experiment	Model	Predictors	Resolution	Calibration	Validation
N48	SDSM	NCEP R1	$2.5^\circ \times 2.5^\circ$	1948-2009	2010-2014
N79	SDSM	NCEP R1	$2.5^\circ \times 2.5^\circ$	1979-2009	2010-2014
E79	SDSM	ERA Interim	$2.5^\circ \times 2.5^\circ$	1979-2009	2010-2014
E79r	SDSM	ERA Interim	$0.75^\circ \times 0.75^\circ$	1979-2009	2010-2014

2.5 Validation Datasets and statistical indicators employed

Several datasets described in section 2.1 were used for validation purposes in this thesis: Atmospheric radiosondes and MODIS data for PW; EOBS, TRMM, GPCP and ECA&D datasets for precipitation (simulated by WRF or by SDSM); and GLEAM v3.0b and v3.0c for evaporation. However, it must be said that the number of datasets that can be used for validation is not very high because at the same time they must cover the period 2010-2014 and they must ideally have a comparable resolution to that used in the model runs.

Since most of the chosen datasets presented a daily temporal resolution, the data from ERAI and both WRF experiments were aggregated to daily values. Different validation techniques and validation scores were used in this study, depending on the characteristics of the analysed variables. If the validation focuses on a single site, Taylor diagrams were used to plot the standard deviation (SD), root mean squared error (RMSE) and Pearson's correlation (r), as it is a really visual way to interpret the results (*Taylor, 2001*). However, if the validation focuses on a field (e.g. PW or evaporation), the nearest neighbour to each point at WRF's mask for the IP was calculated in the other grids. This methodology has been regularly used in previous studies such as *Borge et al. (2008)*; *Jiménez et al. (2010)*; *Jiménez and Dudhia (2012)*; *Önol (2012)*; *Soares et al. (2012)*. Then, the results were plotted in coloured maps representing the correlation, the bias or the RMSE.

Not only for accurately representing the sampling errors of the observed data, the bootstrap technique with resampling was also used to calculate the significance of our results. Particularly to determine the difference between different verification scores for alternative models. To do so, 1000 time series were created with replacement and compared against the validation datasets. The results of these new time series are also included in the Taylor diagrams. All the corresponding points plotted delimit a shaded region around the results for the full sample (represented by a big point). This region shows the variability of the scores and if the shaded regions of two different experiments do not overlap each other, the results are taken as significant. However, while comparing both downscaling techniques (in chapter 4), the results of the bootstrap technique will not be included in the Taylor diagrams and the scores reached by this technique will be studied in a separate figure in order to improve the clarity of the Taylor diagrams.

Additionally, an empirical orthogonal function (EOF) analysis was carried out. This methodology will help us to identify and extract the independent patterns (the normal modes) that would reconstruct the original data. Following the nomenclature described by *Hannachi et al. (2007)*, the spatial patterns are typically called EOFs, and their associated temporal projections are the principal components (PCs).

Particularly for the dynamically and statistically downscaled precipitation comparison study (chapter 4), some statistical indicators were derived from the results of the SDSM and WRF experiments. To test the ability of the SDSM experiments fore-

casting the observed precipitation, the Area Under the Curve (AUC) of the Relative Operating Characteristic (ROC) curve ([Mason, 1982](#)) was calculated. These curves plot the hit rate versus the false alarm rate by means of several probability thresholds (from 0.05 to 0.95 by 0.05 in our case). The diagonal line of the plot delimits if the forecast is able to discriminate between events and non-events. If the curve goes above the diagonal, the forecast is skilful, but if it goes below the diagonal, the forecast is not skilful at all. In our case, the AUC perfect score would be 0.5, and 0 would represent no skill.

As the SDSM creates a 20-member ensemble by default, we need to compare a deterministic product as WRF with a probabilistic one. To do so, the results from SDSM experiments will be studied focusing on the mean of the ensemble, but also studying each member of the ensemble independently as if they were different experiments. An evaluation of the SDSM ensemble was evaluated by means of the Linear Error in Probability Space (LEPS) ([Ward and Folland, 1991](#)). It measures the error in probability space as opposed to measurement space, and the perfect score would be 0 (with values ranging between 0 and 1).

Additionally, the added value of both downscaling techniques was analysed by means of the Brier Skill Score (BSS). In this case, the precipitation from ERAI was used as a reference forecast. The definition given by [Storch and Zwiers \(1999\)](#) was followed, commonly used in the literature ([Winterfeldt et al., 2011](#); [García-Díez et al., 2015](#)). It was applied to the D experiment, SDSM mean and each ensemble member. The values of the score range between -1 and 1. The studied experiment outperforms the reference forecast if positive values are obtained, but the reference forecast is better if negative values are returned.

Finally, several precipitation indices were calculated. However, as our validation period (2010-2014) is not really long, there is not enough data to reliably calculate extreme precipitation indices such as the number of heavy events or the fraction of total from heavy events. Thus, only indices related to the precipitation amount and occurrence were included in this study:

- Absolute mean daily precipitation (pav): average precipitation of all days.
- Wet-day intensity (pint): average precipitation of days above 1 mm.
- 90th percentile wet-day total (pq90): 90th percentile of precipitation of days above 1 mm.
- Maximum consecutive dry days (pxcdd): number of consecutive days with precipitation below 1 mm.
- Wet-day probability (pwet): number of days with precipitation above 1 mm divided by the number of days of the analysed period.
- Maximum five-day total precipitation (px5d): maximum precipitation amount measured in five consecutive dry days.

These indices have previously been used to analyse precipitation in studies such as [Haylock et al. \(2006\)](#), [Wilby and Yu \(2013\)](#) and [Nicholls and Murray \(1999\)](#).

2.6 Analysis of the Water Balance

In order to analyse the atmospheric water budget over the IP simulated by both WRF simulations and ERAI, the moisture conservation equation for vertically integrated quantities and surface fluxes (equation 12.9 from *Peixoto and Oort (1992)*) is used:

$$\frac{\partial W}{\partial t} + \vec{\nabla} \cdot \vec{Q} + \frac{\partial W_c}{\partial t} + \vec{\nabla} \cdot \vec{Q}_c = E - P \quad (2.1)$$

where W is the PW, $\vec{\nabla} \cdot \vec{Q}$ is the divergence of moisture flux, and E and P are the evaporation and precipitation respectively. The subscript c denotes the terms related to the condensates simulated by model's microphysical scheme.

Starting from equation 2.1, the residual η of the water conservation equation was defined for each grid point as follows:

$$\eta = \frac{\partial W}{\partial t} + \vec{\nabla} \cdot \vec{Q} + \frac{\partial W_c}{\partial t} + \vec{\nabla} \cdot \vec{Q}_c - E + P \quad (2.2)$$

The most important terms in Equation 2.1 (W , $\vec{\nabla} \cdot \vec{Q}$, E , P) were quantitatively verified against observations, namely precipitable water (in section 3.1), precipitation (in section 3.2) and evaporation E (in section 3.3). In other cases, direct observations do not exist (such as is the case for divergence of moisture transports $\vec{\nabla} \cdot \vec{Q}$) and the verification was carried out by checking the closure of the water conservation equation. The spatial pattern of the residual η was studied for both WRF simulations and ERAI, particularly for the annual and seasonal means. Additionally, annual and seasonal accumulation maps were calculated for each term of the water balance, together with areal mean plots when showing time series of evaporation.

3 Analysis of the Water Balance

THE main objective of this chapter of the thesis is to study the moisture balance over the IP using both simulations created with WRF. The closure of the atmospheric hydrological cycle will be studied focusing on the moisture balance within the model, but also on how each element of it is simulated (by comparing with observational datasets).

Several sections are included in this chapter. The first three of them focus on the validation of elements of the water balance: PW in section 3.1, precipitation in section 3.2 and evaporation in section 3.3. Afterwards, the residual (defined following equation 2.1) and the effect of the data assimilation step are analysed in sections 3.4 and 3.5 respectively. Finally, the most important features observed on the hydrological cycle are presented in section 3.6.

3.1 Validation of Precipitable Water

As previously stated in section 2.5, two different datasets were used to validate the PW over the IP: Radiosondes downloaded from the server of the University

of Wyoming and data from MODIS.

The radiosonde data are based on eight stations evenly spaced across the IP. For each station a Taylor diagram was created, including both WRF experiments and ERAI. Figure 3.1 shows the results for the comparison of these data with the observed PW. The experiment with data assimilation (D) was the one with the best scores in all the available stations (r between 0.98 and 0.99 for daily data) with a 95% confidence level. The D experiment (including data assimilation) improved the results of the N experiment (r between 0.8 and 0.85). Furthermore, it was able to outperform ERAI (r between 0.93 and 0.97). The SD produced by both WRF experiments is closer to that observed, and in five stations (Madrid, A Coruña, Santander, Zaragoza and Murcia), its value is better than the one for ERAI. The same distribution of the experiment as for correlation is observed for RMSE. The D experiment produces the best score (RMSE smaller than 2 mm in every station), followed closely by ERAI (RMSE ranging between 2 mm and 4 mm). The N experiment, without data assimilation, produced the worst RMSE in every station (RMSE higher than 3.5 mm).

By means of the bootstrap technique with resampling, 1000 time-series were created for each experiment and compared with the observations. Their results are included on each Taylor diagram as points that are arranged as shaded regions. Since the shaded regions of the experiments do not overlap each other, our results are shown to be significant.

Scatterplots between both simulations and ERAI with observations showed that the slope obtained from the regression line was really well reproduced by both WRF runs (N: from 0.82 to 0.98, D: from 0.92 to 1.00). Particularly for the D experiment, which was able to beat ERAI (from 0.79 to 1.01). However, the bias was larger for the N experiment (between 1.96 mm to 4.09 mm), whilst for D and ERAI the spread of the values was smaller (between -1 mm and 1 mm). The results for every station can be found on Table 3.1.

The correlation coefficient of each experiment after removing the seasonal cycle

Table 3.1: Characteristics of the regression lines between the observed PW and N, D and ERAI.

Experiment	A Coruña		Santander		Zaragoza		Barcelona	
	Slope	Intercept	Slope	Intercept	Slope	Intercept	Slope	Intercept
ERAI	0.97	0.17	0.79	-0.29	0.92	-0.69	0.79	0.97
N	0.98	1.96	0.95	1.76	0.92	2.46	0.82	3.441
D	0.98	0.35	0.96	0.49	1.00	0.00	0.93	0.55
Experiment	Murcia		Gibraltar		Lisbon		Madrid	
	Slope	Intercept	Slope	Intercept	Slope	Intercept	Slope	Intercept
ERAI	0.82	0.39	0.94	-1.07	1.01	0.99	0.91	0.53
N	0.82	3.67	0.82	3.57	0.91	4.09	0.90	2.888
D	0.93	0.55	0.92	-0.01	1.00	0.66	0.99	0.37

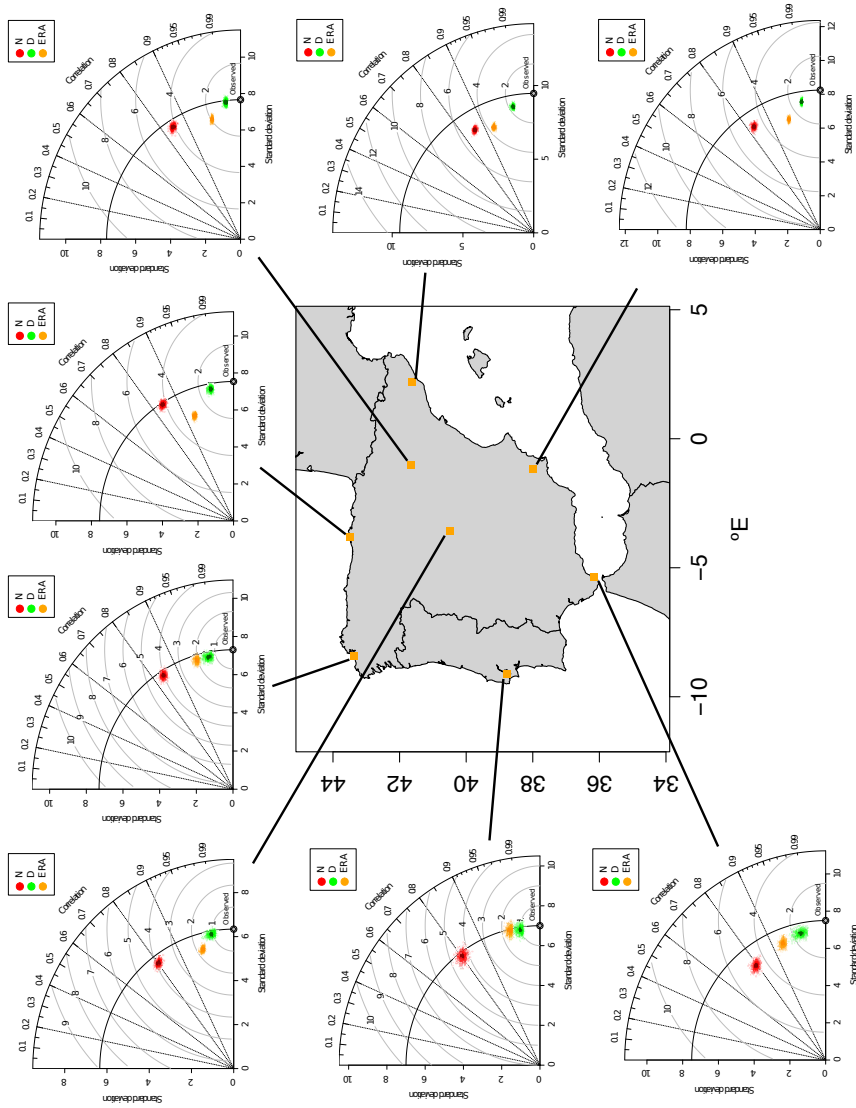


Figure 3.1: Taylor diagrams showing the standard deviation, r and RMSE results for ERAI, N and D experiments compared to radionuclide data (coloured in orange, red and green respectively). The small dots represent the results for each time series created using the bootstrap technique, while the big dots correspond to the results obtained from the full sample of observed radionuclide data.

3.1 Validation of Precipitable Water

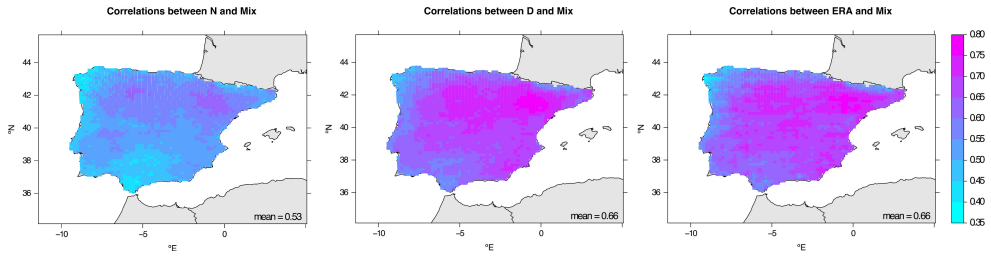


Figure 3.2: Correlation for both WRF simulations and ERAI compared to PW data collected by MODIS aboard Aqua and Terra satellites. The spatial average of the points included in the IP is presented in the right bottom corner of the map.

was also calculated. The D experiment is the one with the best score (r between 0.97 and 0.99). Worse scores were obtained for ERAI (r between 0.86 and 0.96), but not as bad as those for the N experiment (r between 0.67 and 0.78).

The verification results for mixed Level 2 data measured by MODIS aboard Aqua and Terra satellites are presented in Figure 3.2. Poor correlations for the N experiment were observed, particularly in the southern and northwestern IP. The D experiment is able to improve the results obtained for N. Not only in the problematic areas of the N experiment, but also on the northern plateau and the Ebro basin. The correlation pattern observed for the D experiment is quite similar to that obtained by ERAI. Both datasets (D and ERAI) reached the same area-averaged r (0.66), while the N experiment obtained 0.53. It is clear that the agreement between satellite and model PW is lower than between soundings and model data.

The bias between both WRF simulations and ERAI with MODIS L2 data is presented in Figure 3.3. The mountain ranges across the IP were clearly recognizable in both WRF simulations. The N experiment presented the poorest results near the final stretch of the Tagus, Guadiana and Guadalquivir rivers, but also in the Ebro basin. The D experiment was able to slightly improve these results, obtaining closer values to those obtained with ERAI (D: -14.84 mm and ERAI: -14.25 mm). The

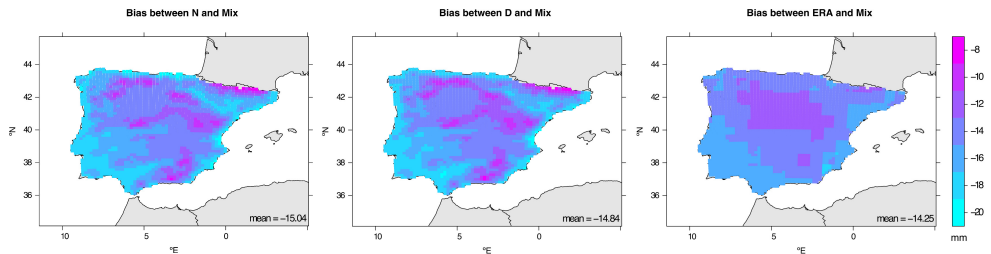


Figure 3.3: Same as Figure 3.2, but for PW bias (mm).

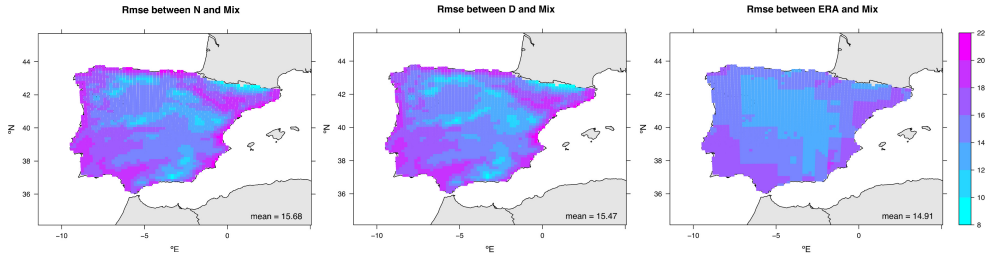


Figure 3.4: Same as Figure 3.2 and 3.3, but for PW RMSE (mm).

results of the experiments are different at a 95% confidence level. The resolution of the spatial grid used in WRF allows a better representation of the results, suggesting that the physical features of the IP delimit the distribution of the PW.

The RMSE maps corresponding to daily data between WRF experiments and ERAI with MODIS data were also calculated (Figure 3.4). Similar results to those for bias were obtained. The best results for both WRF simulations are obtained near the mountain ranges of the IP, and the highest values are located near the coasts of it. However, the D experiment is able to slightly improve the results from the experiment without data assimilation (N: 15.68 mm and D: 15.47 mm). Again, the results of the experiments are different at a 95% confidence level. For ERAI, the highest values are observed in the southwestern and Mediterranean coasts of the IP. The areal mean RMSE observed for this experiment is 14.91 mm.

Both validation datasets showed that the D experiment improved the results obtained by the N experiment, and that these results are comparable to those obtained by ERAI. However, the 15 km resolution at WRF's domain allows a better understanding on the spatial distribution of the PW.

3.2 Validation of Precipitation

Many datasets were selected for the validation of precipitation. As stated in section 2.5: EOBS, TRMM, GPCP and twenty-one stations from ECA&D.

We will start by showing the validation of precipitation against the EOBS dataset. Figure 3.5 shows the correlations between this dataset and both WRF simulations and ERAI. The northwestern IP is the best region reproduced by WRF and ERAI. Poor correlation values are observed in the Ebro basin and southeastern Spain, particularly for the N experiment (mean r value 0.53). However, the experiment with data assimilation is able to improve r in these regions, making it comparable to ERAI as both reach similar areal mean r values: 0.64 and 0.63 respectively. Different correlation patterns are observed for these two similar experiments: while the D ex-

3.2 Validation of Precipitation

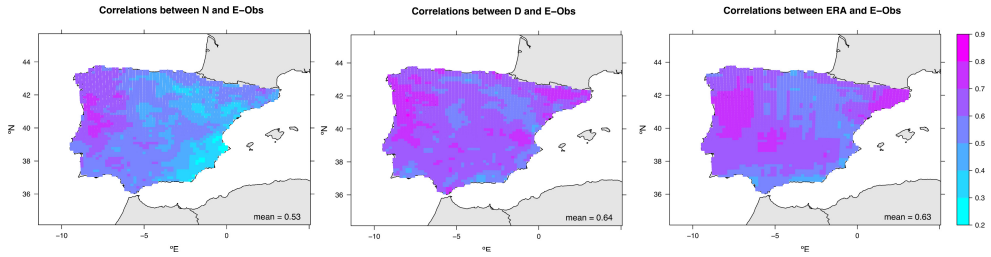


Figure 3.5: Precipitation correlation maps between EObs dataset and both WRF simulations and ERA. The mean r value for correlations against EObs is presented in the right bottom corner of the maps.

periment has problems reproducing the rain in the west side of the mountain ranges, ERAI presents major problems in the southern coast of Spain and in the Ebro basin.

The bias for EObs (Figure 3.6) showed large differences for the N experiment in the northwestern part of the IP, the Pyrenees and in the Central and Baetic mountain ranges. The D experiment shows better agreement with EObs, with some discrepancies remaining mainly in the north of the IP. A similar pattern is observed for ERAI, especially in the northwestern IP. Mean biases of -0.18, 0.07 and -0.02 mm/day are measured for N, D and ERAI respectively.

The RMSE (Figure 3.7) showed that the N experiment presented major discrepancies with EObs near the mountain ranges of the IP, but also near the mouth of the Ebro river. The experiment with data assimilation is able to reduce them and only in the northwestern IP can be found high values of RMSE. A similar pattern is observed for ERAI. The areal RMSEs obtained for N, D and ERAI are 4.62, 3.75 and 3.49 mm/day respectively.

Focusing on the correlations of the twenty-one stations selected from the ECA&D dataset (Figure 3.8), the N experiment obtained the poorest results. Particularly near the Mediterranean coast, where values below 0.3 can be found. The D experiment improves these results in the center and southern regions of Spain, but the poorest

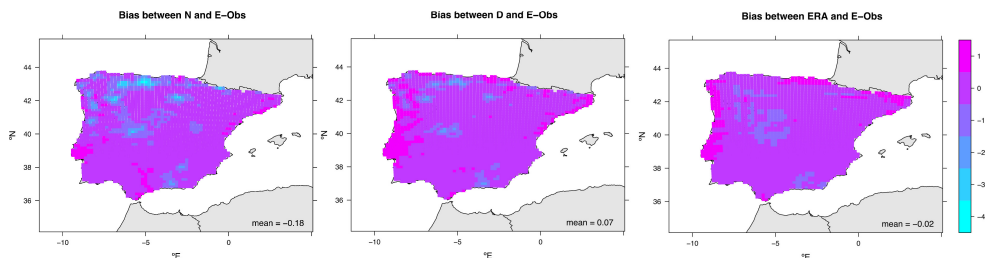


Figure 3.6: Same as Figure 3.5, but for bias (mm/day).

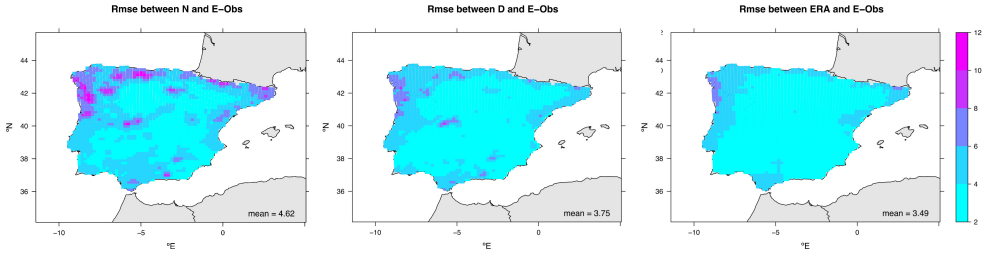


Figure 3.7: Same as Figure 3.5 and 3.6, but for RMSE (mm/day).

results can still be found near the Mediterranean coast. The areal mean correlations improved from 0.44 to 0.54 with the data assimilation step. The experiment with data assimilation is able to outperform ERAI in some stations of the southern IP, but ERAI's areal mean correlation (0.5) is quite close to that from D.

The biases are better for the inland parts of the IP for both WRF simulations and ERAI (Figure 3.9). For the N experiment, the largest biases are obtained in A Coruña, Lisbon, Córdoba and Barcelona stations. This experiment underestimates the precipitation in A Coruña, but overestimates it in Lisbon and Barcelona. The D experiment is able to improve the results for A Coruña and Barcelona, but not those for Lisbon and Córdoba. However, this experiment is that with the largest mean bias (0.3 mm/day). Lisbon is also problematic for ERAI, along with Vigo and Santander, where largest biases can be found. The best score is obtained for the N experiment, followed by ERAI (0.08 and 0.12 mm/day respectively)

Focusing on the RMSE, a northwest-southeast dipolar pattern can be observed on the three experiments (Figure 3.10). For both WRF experiments, the largest RMSE is found in Vigo and the smallest in Murcia. For ERAI, the smallest RMSE is obtained inland, in Madrid. The largest areal mean RMSE is obtained for the N experiment, followed by ERAI and D, with 5.09, 4.56 and 4.43 mm/day respectively.

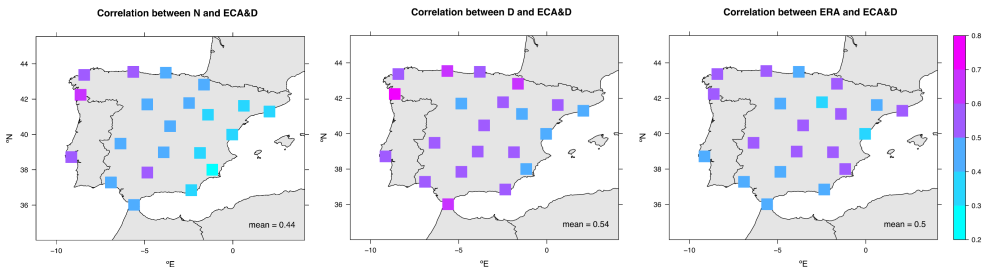


Figure 3.8: Precipitation correlation maps between ECA&D dataset and both WRF simulations and ERAI. The mean r value for each one of the chosen twenty-one stations from ECA&D is presented in the right bottom corner of the maps.

3.2 Validation of Precipitation

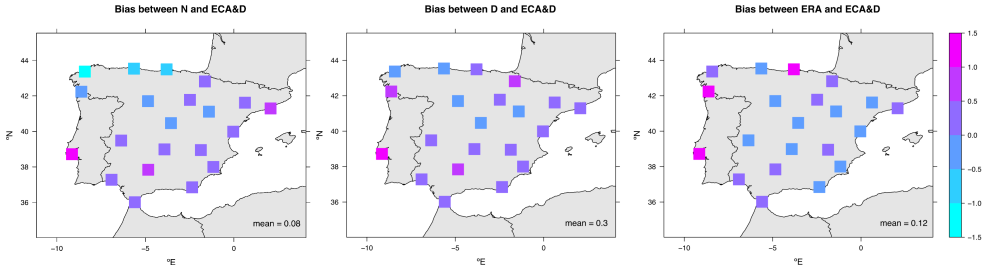


Figure 3.9: Same as Figure 3.8, but for bias (mm/day).

Similar maps to those from EOBS are obtained for TRMM, where the best correlation values are obtained for the northwestern IP (see Figure 3.11). However, compared to TRMM, the poorest results are obtained also in the east Cantabrian coast apart from the Mediterranean coast. Again, the D experiment is able to improve the correlation of these problematic zones. The correlation pattern for D and ERAI is similar, and also their areal mean correlation: 0.47 and 0.48 respectively (0.36 for N).

Focusing on the bias between WRF precipitation and TRMM, similar differences to those in GPCP are also observed here near the Cantabrian coast (see Figure 3.12). Both WRF simulations overestimate the precipitation in that region, particularly the N experiment. The data assimilation reduces these differences. The areal mean bias is reduced from -0.65 to -0.4 mm/day changing from N to D. Similar pattern is observed over the IP for ERAI (areal mean bias is -0.48 mm/day). The three experiments highly underestimate the precipitation near the Pyrenees.

The RMSE pattern observed for both WRF experiments is similar to that obtained with EOBS (see Figure 3.13). Again, the largest values are obtained near the mountain ranges of the IP, particularly in the northwestern zone. However, the D experiment manages to reduce this RMSE from N (the areal mean RMSE is reduced from 5.58 to 4.72 mm/day). For ERAI, the largest values appear near the Pyrenees and in Sierra Nevada. The areal mean RMSE for ERAI is 4.3 mm/day, smaller than

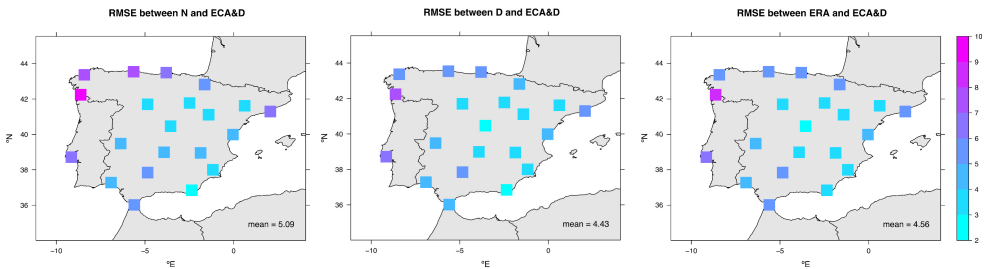


Figure 3.10: Same as Figure 3.8 and 3.9, but for RMSE (mm/day).

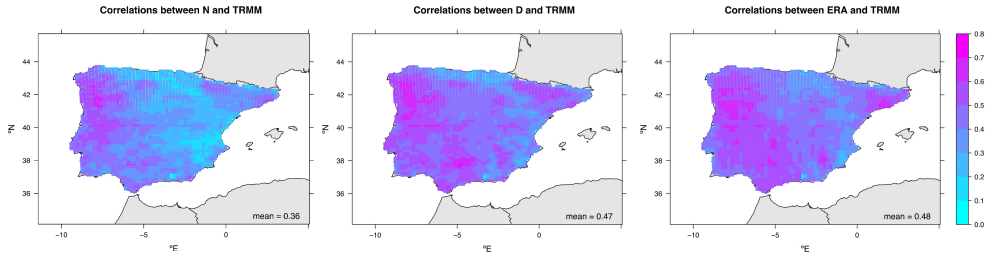


Figure 3.11: Precipitation correlation maps between TRMM dataset and both WRF simulations and ERAI. The mean r values obtained by each experiment are presented in the right bottom corner of the maps.

that for D.

Finally, the scores for GPCP were calculated. Focusing on the correlation (Figure 3.14), the highest values are obtained over Portugal and the Pyrenees on the three experiments. The poorest correlations are observed for the N experiment, near the Mediterranean and east Cantabrian coasts along with the Ebro basin. The data assimilation experiment improves the results from N. ERAI's pattern is similar to that from D, but the poor resolution of ERAI influences the results. The areal mean correlations are 0.46 mm/day for both D and ERAI, but 0.39 mm/day for N.

Changing from correlation to bias (see Figure 3.15), it is clear that the same pattern observed on the other gridded datasets is also here. Both WRF simulations overestimate the precipitation near the mountain ranges of the northwestern IP, particularly the N experiment. Precipitation is underestimated near the Mediterranean coast and Ebro basin. ERAI underestimates the precipitation in the east Cantabrian and Catalanian coasts. The areal mean biases for N, D and ERAI were 0.24, 0.49 and 0.4 mm/day respectively.

The largest RMSEs for both WRF experiments (Figure 3.16) are located in the above mentioned mountain ranges. However, the data assimilation is able to improve the results and the RMSE is highly reduced in those places (areal mean RMSE is reduced from 6.02 to 5.41 mm/day from N to D). For ERAI, the results are smoothed by the poor resolution of the reanalysis, but a similar pattern to D is observed. In

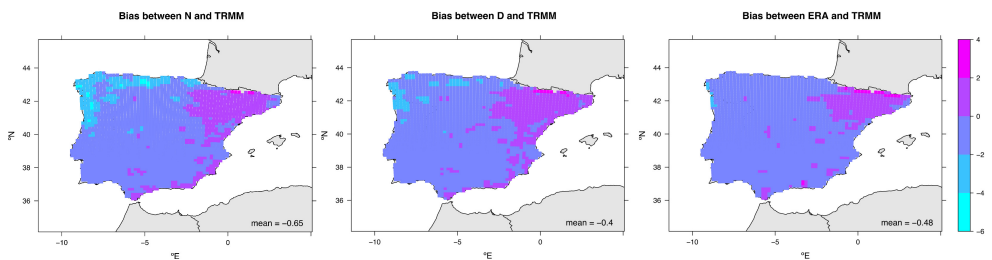


Figure 3.12: Same as Figure 3.11, but for bias (mm/day).

3.2 Validation of Precipitation

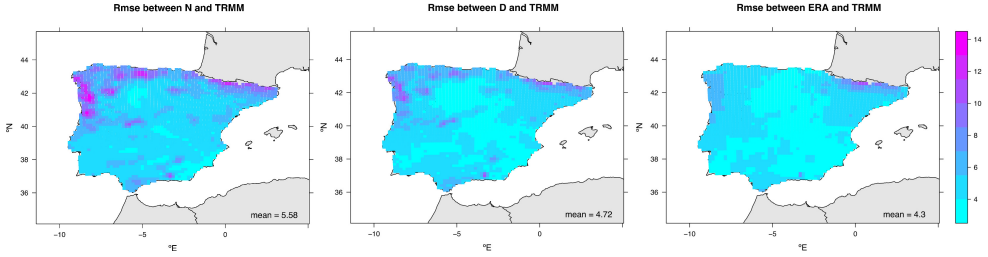


Figure 3.13: Same as Figure 3.11 and 3.12, but for RMSE (mm/day).

this case, the areal mean RMSE is 5.06 mm/day.

Once every experiment was validated against the observational datasets, in order to summarize the r and bias results, a quantile-based analysis is presented in Tables 3.2 and 3.3. Taking into account these four validation datasets, the correlations obtained by the N experiment against each of them were worse than those for ERAI and the D experiment. The D experiment obtained better (or at least similar against GPCP and TRMM) results to those for ERAI on each validation. The highest results for the D experiment were obtained while comparing to EOBS dataset, with values ranging from 0.53 to 0.76 across the IP. However, the largest differences between D and ERAI are obtained while comparing to ECA&D datasets. In this case, the correlations for D range between 0.69 and 0.45, while for ERAI the values range between 0.60 and 0.38.

Focusing on the bias (Table 3.3), the spread of the results was bigger for the N experiment, particularly comparing with TRMM. Comparable results were observed for ERAI and the D experiment. However, the spread of the D experiment was better when comparing to ECA&D. Then, it is clear that the D experiment improves the results from the N experiment (without data assimilation) and that similar results are obtained for D and ERAI.

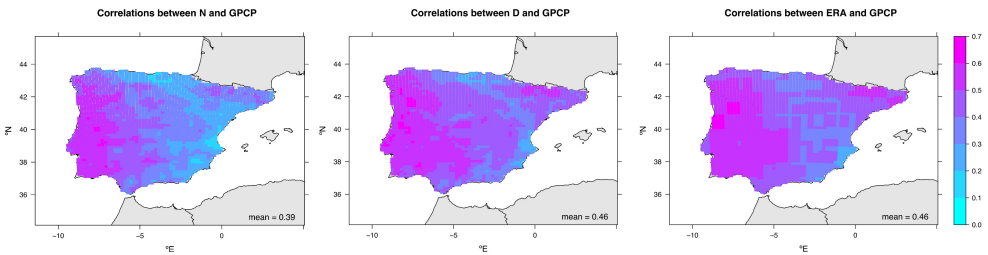


Figure 3.14: Precipitation correlation maps between GPCP dataset and both WRF simulations and ERAI. The mean r value for GPCP is presented in the right bottom corner of the maps.

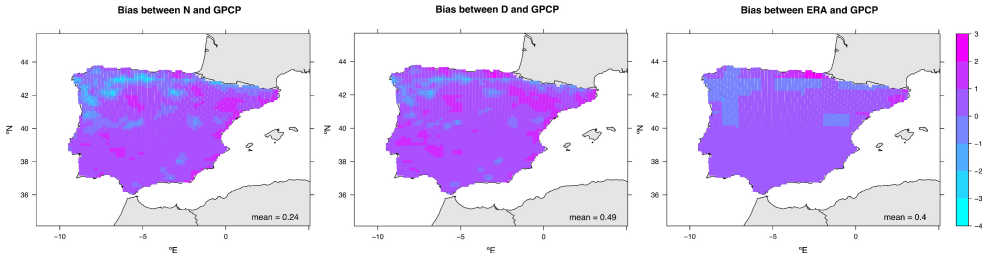


Figure 3.15: Same as Figure 3.14, but for bias (mm/day).

3.3 Validation of Evaporation

Analysing the static geographical data used by WRF for our domain, the predominant types of soil and land uses over the IP can be studied. The soil type in the region is mainly loam, with the exception of the Guadalquivir basin that is made of clay. Conversely, the land uses over the IP are more varied (see Figure 3.17). Evergreen and mixed forests are detected in the mountain ranges of the IP and in the northern Spain. The plateaus are full of croplands, mixed with woody savannas and open shrublands in the southern Spain. A clear relationship with the climatic areas arises from this distribution of land uses.

Focusing on the *Urban and Built-Up* category in the model soil type, three different urban sites can be clearly spotted: Barcelona, Madrid and Porto. These urban points of the grid must be removed since WRF is not able to simulate correctly their evaporation (Figure 3.18) due to the mismatch between the real land use and the simulated one. The correlation of these points with their nearest points in GLEAM grid was zero or negative, with values between 0 and -0.4. As this was a problem related to the LSM, all these points were eliminated from the validation.

As previously stated in section 2.5, two versions of the GLEAM dataset were selected as validation datasets for evaporation: GLEAM 3.0b and 3.0c. Mean daily

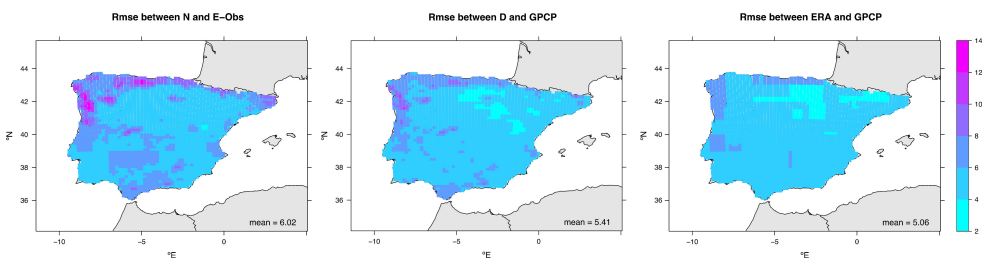


Figure 3.16: Same as Figures 3.14 and 3.15, but for RMSE (mm/day).

3.3 Validation of Evaporation

Table 3.2: Spatial quantile-based analysis of the correlations obtained for precipitation in both WRF experiments and ERAI with the validation datasets: EOBS, ECA&D, GPCP and TRMM. The best results were highlighted with orange boxes.

Dataset	Exp	q97.5	q95	q75.	q50	q25	q5	q2.5
EOBS	N	0.71	0.68	0.59	0.53	0.48	0.36	0.32
EOBS	D	0.76	0.74	0.68	0.64	0.61	0.55	0.53
EOBS	ERA	0.76	0.74	0.68	0.63	0.58	0.52	0.49
ECA&D	N	0.59	0.57	0.49	0.44	0.39	0.31	0.29
ECA&D	D	0.69	0.67	0.57	0.53	0.50	0.46	0.45
ECA&D	ERA	0.60	0.60	0.53	0.50	0.45	0.39	0.38
GPCP	N	0.58	0.57	0.48	0.39	0.31	0.23	0.21
GPCP	D	0.60	0.58	0.53	0.46	0.41	0.32	0.29
GPCP	ERA	0.58	0.58	0.52	0.47	0.41	0.33	0.31
TRMM	N	0.57	0.54	0.44	0.36	0.28	0.20	0.18
TRMM	D	0.63	0.60	0.53	0.48	0.42	0.32	0.30
TRMM	ERA	0.62	0.60	0.55	0.48	0.42	0.35	0.33

evaporation of both GLEAM versions was calculated for 2011-2014 (Figure 3.19), the period when both versions overlap. The largest values of evaporation (above 1.5 mm/day) are found in the northwestern IP, near the Pyrenees and near the Portuguese and Mediterranean coasts in both datasets. The poorest results (below 1 mm/day) are found in the southeastern corner of the IP and in the northern plateau. The most remarkable differences between GLEAM 3.0b and 3.0c are concentrated in the north-western and eastern sides of the IP. The highest values of the difference were located in this last region, reaching 0.20 mm/day. Taking into account that the differences between both versions are not really large and that the year 2010 is not available for version 3.0c, only the correlation, bias and RMSE maps against GLEAM v3.0b were included here with the aim of showing a validation for the same

Table 3.3: Same as Table 3.2 but for bias (mm/day).

Dataset	Exp	q97.5	q95	q75.	q50	q25	q5	q2.5
EOBS	N	0.59	0.48	0.18	-0.05	-0.39	-1.38	-1.84
EOBS	D	0.88	0.71	0.31	0.12	-0.15	-0.72	-1.05
EOBS	ERA	0.93	0.71	0.16	-0.04	-0.25	-0.59	-0.67
ECA&D	N	0.89	0.68	0.32	0.20	-0.10	-0.90	-0.99
ECA&D	D	1.02	0.77	0.43	0.28	0.09	-0.17	-0.23
ECA&D	ERA	1.09	1.08	0.29	0.00	-0.17	-0.38	-0.42
GPCP	N	1.13	1.06	0.77	0.49	-0.03	-1.42	-2.01
GPCP	D	1.25	1.18	0.87	0.63	0.27	-0.73	-1.19
GPCP	ERA	1.09	0.93	0.63	0.43	0.22	-0.25	-0.55
TRMM	N	0.73	0.51	-0.14	-0.45	-0.88	-2.70	-3.23
TRMM	D	0.86	0.64	-0.05	-0.33	-0.63	-1.81	-2.31
TRMM	ERA	0.90	0.41	-0.21	-0.51	-0.74	-1.66	-1.82

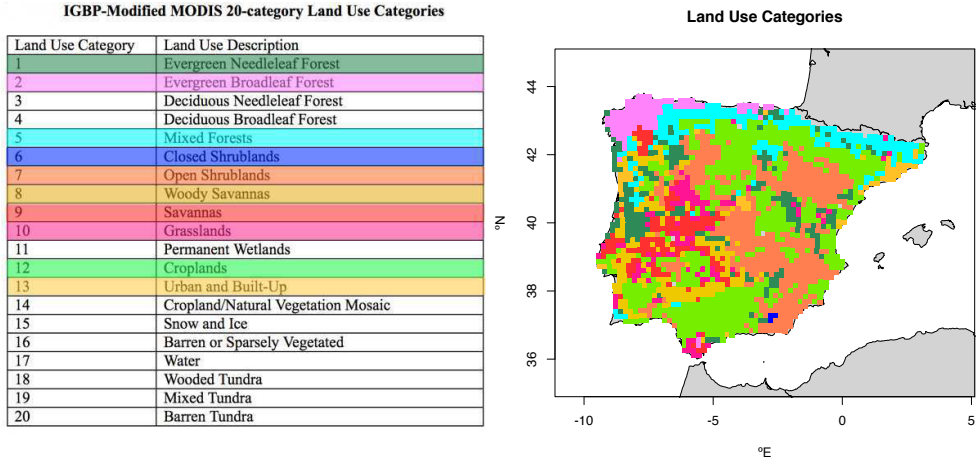


Figure 3.17: The surface of the IP coloured according to the Modified MODIS 20 Land Use Categories, defined by the NOAA LSM in both WRF simulations.

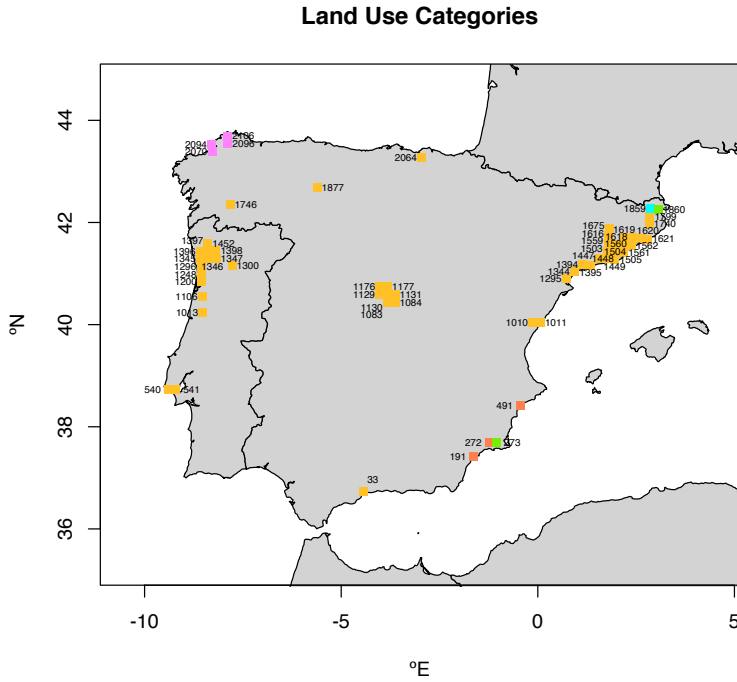


Figure 3.18: Eliminated points from the validation of evaporation because of the lack of ability to simulate observed evaporation by Noah LSM depending on their land uses. The same colorbar to that in Figure 3.17 is used here.

3.3 Validation of Evaporation

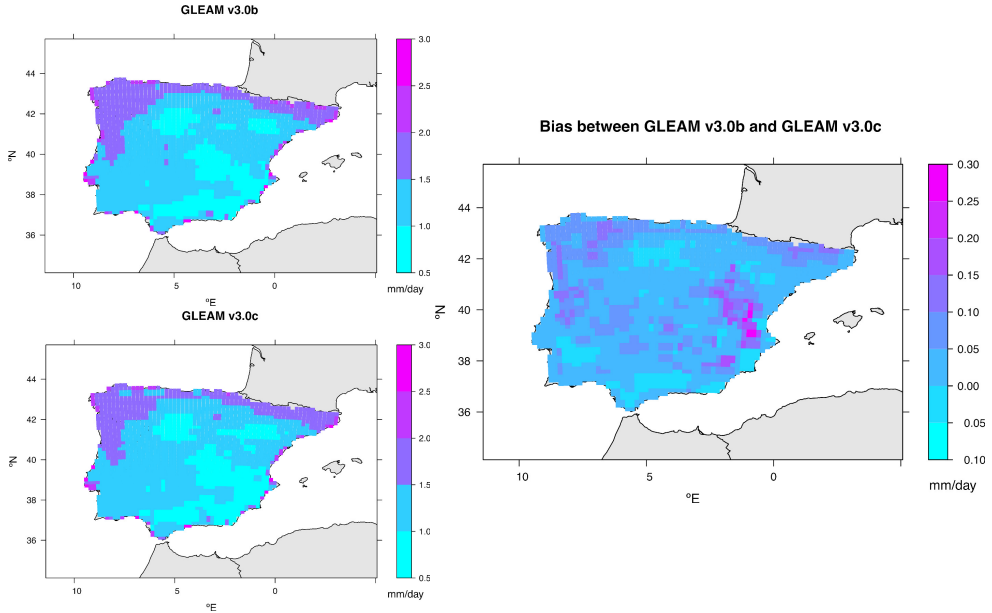


Figure 3.19: Left panel: Mean daily evaporation for GLEAM 3.0b (top) and 3.0c (bottom). Right panel: Differences between both datasets for period 2011-2014.

period as that for both WRF experiments (2010-2014). However, a summary table comparing both versions of GLEAM dataset is included at the end of this section.

The correlation map for the comparison of evaporation with GLEAM v3.0b is presented in Figure 3.20. For the N experiment, poor results appear near the Ebro basin and the Mediterranean coast. The D experiment is able to improve these results, as showed by the areal mean values obtained for N and D (0.34 and 0.48 respectively). The values obtained by the experiment with data assimilation are similar to those for ERAI (0.51). A similar pattern is observed in both experiments, showing their poorest results for the Mediterranean coast and the northwestern IP. Similar results (and patterns) were obtained if comparing to GLEAM v3.0c dataset, with 0.33, 0.47 and 0.51 as mean values for N, D and ERAI respectively.

Results for the evaporation bias are presented in Figure 3.21. For the N experiment, the best results were observed inland. Near the southern and south-eastern coasts of the IP some points with large biases appeared. However, the areal mean bias was only -0.01 mm/day for this experiment. Both the D experiment and ERAI showed a negative bias, being more remarkable for ERAI (-0.26 mm/day and -0.82 mm/day respectively). No clear pattern was observed for the D experiment, but some grid cells with large biases were observed again. For ERAI, large positive biases appeared near the Pyrenees, contrasting with the large negative biases near the coasts of the IP. Similar results were obtained for GLEAM v3.0c, with -0.05, -0.32 and -0.86 mm/day biases for N, D and ERAI respectively.

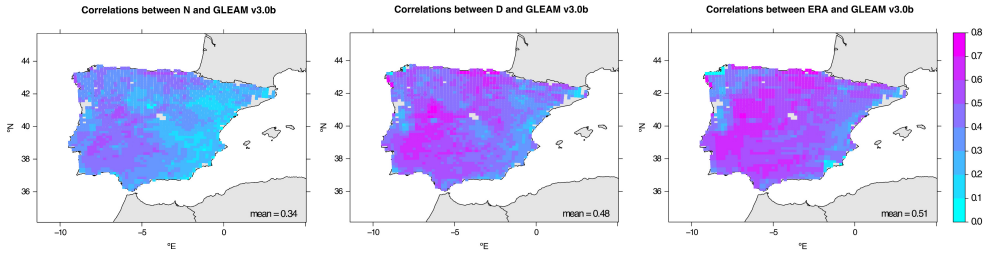


Figure 3.20: Evaporation correlation maps between GLEAM (version 3.0b) for both WRF simulations and ERAI. The problematic points presented in Figure 3.18 were eliminated and the mean correlation values are presented in the right bottom corner of the maps.

The RMSE maps of both WRF simulations and ERAI against GLEAM v3.0b are presented in Figure 3.22. For the N experiment, the best results appeared inland of the IP. The largest values are located in the northwestern IP, but particularly in some grid points of the southern and Mediterranean coasts. The D experiment is able to reduce the big RMSE at these points, but it also produced larger RMSEs in other regions of the IP. However, the areal mean RMSE obtained by both WRF experiments is quite similar: 0.73 mm/day for N and 0.77 mm/day for D. The poorest results for ERAI are obtained near the coasts of the IP (not in the Cantabrian coast) and the mean RMSE is 1.08 mm/day. Similar patterns were obtained for GLEAM v3.0c, with 0.71, 0.79 and 1.11 mm/day for N, D and ERAI respectively.

The effect of removing all urban points in the validation was observed particularly in the correlation and bias measured for both WRF experiments and ERAI. Those results are presented along with the summary tables of the correlations and biases of both GLEAM versions (Tables 3.4 and 3.5). A quantile analysis of the values before and after removing these problematic points can help us to quantify its effect. Focusing on the correlation, the worst results were always obtained by the N experiment (with and without the *Urban* points). The D experiment and ERAI obtained similar results if the *Urban* points are included or not. Same features are observed for the correlations with GLEAM v3.0c. It is clear that if the problematic points are removed, the correlations are improved below the 50th percentile for both

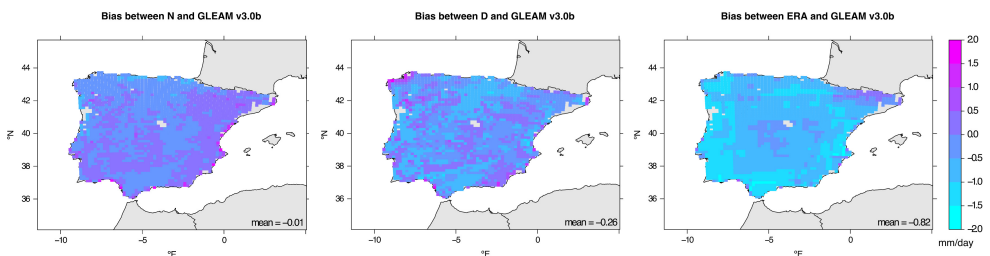


Figure 3.21: Same as Figure 3.20 but for bias (mm/day).

3.3 Validation of Evaporation

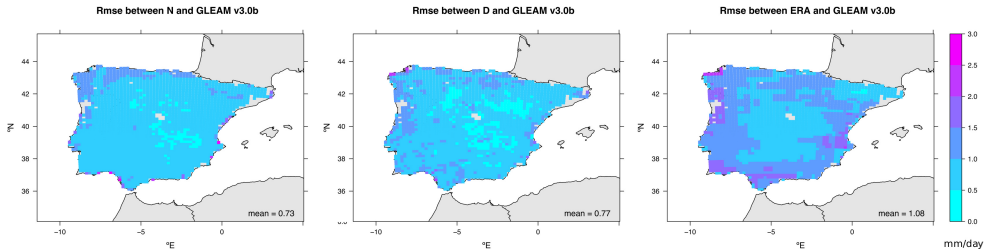


Figure 3.22: Same as Figures 3.20 and 3.21 but for RMSE (mm/day).

versions of the GLEAM dataset.

If we change to the bias (Table 3.5), the N experiment is the one with the best scores in both datasets, followed by D and ERAI. The biases are highly reduced in both WRF experiments when the problematic points are eliminated (above the 50th percentile). However, no substantial changes affect ERAI and only the 95th percentile changed when removing the urban points. Therefore, we can assume that the results are quite robust in the central part of the probability distribution function of the verification scores (correlation, bias and RMSE).

Finally, as a result of the negative biases observed for ERAI, the areal mean of the monthly evaporation was calculated. Figure 3.23 showed a similar spatially averaged evaporation rate for GLEAM and both WRF experiments. However, an intensified behaviour was observed for ERAI over the IP. The bias between ERAI and GLEAM v3.0b varied from 0.59 in winter to 1.11 mm/day in summer. For GLEAM v3.0c, a bias of 0.6 in winter and 1.30 mm/day in summer were measured.

Table 3.4: Spatial quantile-based analysis of the correlations obtained for evaporation in both WRF experiments and ERAI with version 3.0b and v3.0c from GLEAM, with and without the problematic urban points. The best results were highlighted with boxes (in orange for v3.0b and in blue for v3.0c).

Version	Exp	q97.5	q95	q75.	q50	q25	q5	q2.5
v3.0b (No Urban)	N	0.51	0.50	0.42	0.35	0.26	0.18	0.17
v3.0b (No Urban)	D	0.66	0.64	0.55	0.48	0.41	0.31	0.27
v3.0b (No Urban)	ERA	0.66	0.64	0.59	0.53	0.45	0.33	0.28
v3.0b (with Urban)	N	0.51	0.49	0.42	0.34	0.26	0.17	0.09
v3.0b (with Urban)	D	0.66	0.64	0.55	0.48	0.40	0.27	0.06
v3.0b (with Urban)	ERA	0.66	0.64	0.59	0.53	0.45	0.31	0.27
v3.0c (No Urban)	N	0.52	0.50	0.41	0.33	0.25	0.17	0.15
v3.0c (No Urban)	D	0.66	0.64	0.55	0.48	0.40	0.31	0.26
v3.0c (No Urban)	ERA	0.66	0.64	0.59	0.53	0.46	0.32	0.27
v3.0c (with Urban)	N	0.52	0.50	0.41	0.33	0.25	0.15	0.10
v3.0c (with Urban)	D	0.66	0.64	0.55	0.47	0.39	0.26	0.06
v3.0c (with Urban)	ERA	0.66	0.64	0.59	0.53	0.45	0.30	0.26

Table 3.5: Same as Table 3.4 but for Bias (mm/day).

Version	Exp	q97.5	q95	q75.	q50	q25	q5	q2.5
v3.0b (No Urban)	N	0.50	0.40	0.16	-0.01	-0.21	-0.41	-0.48
v3.0b (No Urban)	D	0.52	0.37	0.03	-0.34	-0.57	-0.83	-0.90
v3.0b (No Urban)	ERA	-0.03	-0.31	-0.63	-0.84	-1.04	-1.29	-1.41
v3.0b (With Urban)	N	1.23	0.51	0.18	-0.00	-0.21	-0.41	-0.48
v3.0b (With Urban)	D	1.27	0.56	0.06	-0.31	-0.56	-0.82	-0.90
v3.0b (With Urban)	ERA	-0.03	-0.27	-0.61	-0.84	-1.04	-1.29	-1.41
v3.0c (No Urban)	N	0.48	0.36	0.13	-0.04	-0.25	-0.50	-0.58
v3.0c (No Urban)	D	0.46	0.32	-0.02	-0.39	-0.62	-0.87	-0.94
v3.0c (No Urban)	ERA	-0.13	-0.34	-0.66	-0.88	-1.08	-1.33	-1.45
v3.0c (With Urban)	N	1.18	0.49	0.14	-0.03	-0.24	-0.50	-0.58
v3.0c (With Urban)	D	1.22	0.51	0.00	-0.37	-0.62	-0.87	-0.94
v3.0c (With Urban)	ERA	-0.11	-0.29	-0.65	-0.88	-1.08	-1.33	-1.44

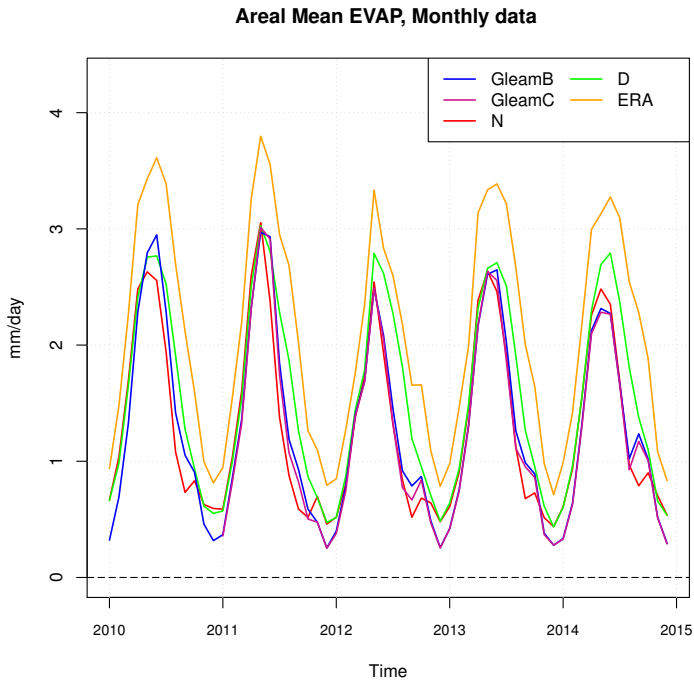


Figure 3.23: Areal mean evaporation simulated by different datasets for 2010-2014. GLEAM v3.0b in blue, GLEAM v3.0c in magenta, the N experiment in red, the D experiment in green and ERAI in orange.

3.4 Analysis of the Residual

The most important terms of equation 2.1 were determined by analysing the spread of their areal mean values. Figure 3.24 shows the distribution of the areal mean monthly data for ERAI and both WRF simulations. It was found that the terms relative to condensates can be disregarded, as previously found by other studies (*Peixoto and Oort, 1992; Snider, 2000; Hirschi et al., 2006*), and that the leading terms of the water balance were the tendency of the PW, the divergence of moisture flux, evaporation and precipitation.

The distribution of the residual was also calculated for Figure 3.24, and the largest residual during 2010-2014 was obtained by ERAI. Both WRF experiments showed a similar spread of the residuals but with opposite signs. It was positive for N

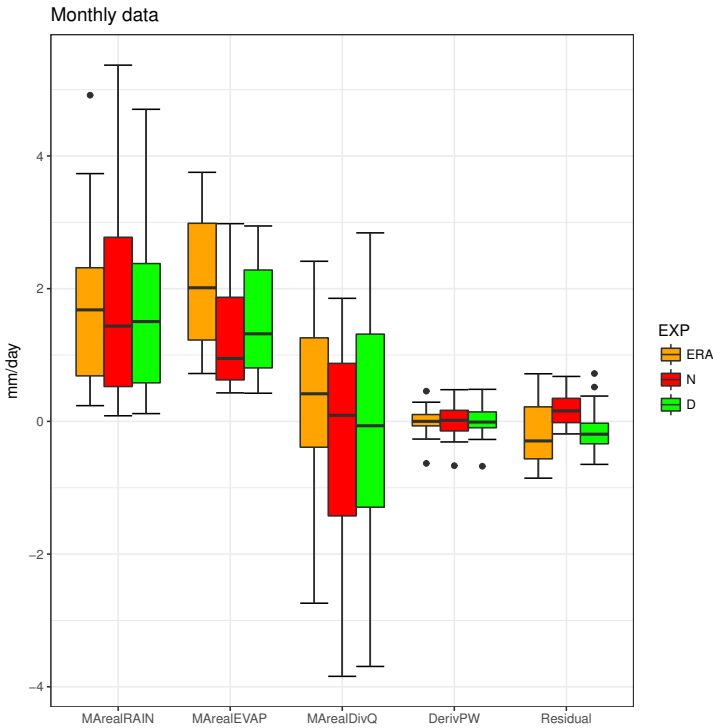


Figure 3.24: Areal mean precipitation (MArealRAIN), evaporation (MArealEVAP), divergence of moisture flux (MArealDivQ), tendency of the PW (DerivQ) and residual, according to different experiments: ERAI in orange, the N experiment in red and the D experiment in green (in mm/day).

and negative for D . Both WRF experiments were configured the same way, so the change in sign from one to another must be attributed to the effect of the 3DVAR assimilation step. Additionally, the D experiment showed a better agreement with observations during the verification. It has also proved to be the experiment with better or similar results to ERAI for each term of the water balance. Taking this feature in mind, only the residual of the D experiment was deeply analysed.

Figure 3.25 shows the distribution of the areal mean values of the residual according to the hour and season for the D experiment. The differences between the values were bigger during summer (JJA) and smaller during winter (DJF). No remarkable differences were observed between spring (MAM) and autumn (SON). A similar behaviour of the six-hourly residuals was noticed on every season. At 00 and 06 UTC, comparable values were obtained. Then, at 12 UTC, the residual was always reduced. Finally, at 18 UTC, the largest values were observed.

An analysis by means of PCs of the area averaged terms $[\frac{\partial W}{\partial t}]$, $[\vec{\nabla} \cdot \vec{Q}]$, $[E]$ and $[P]$ showed that the leading PC explains 72% of the total variance with anomalies of the same sign tied to $[\frac{\partial W}{\partial t}]$ and (weaker) $[P]$. In this leading PC, an opposite

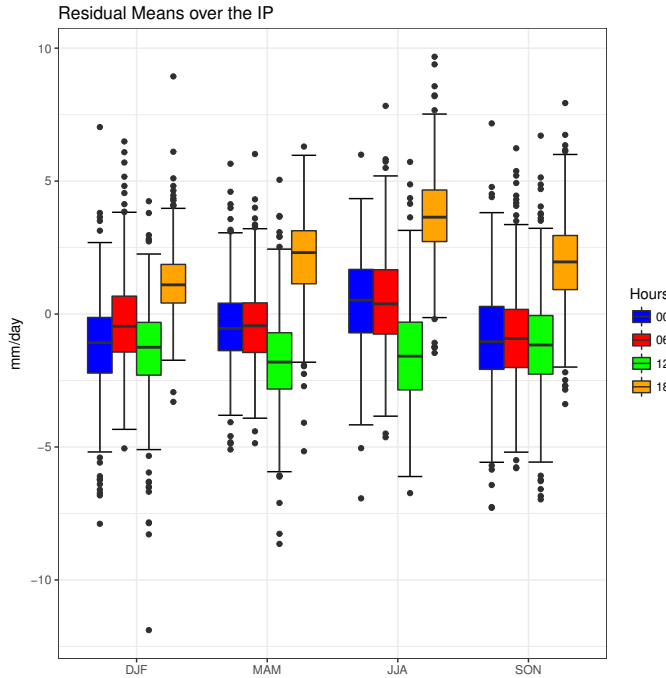


Figure 3.25: Areal mean of the residual over the IP according to the D experiment stratified by season (winter DJF, spring MAM, summer JJA, autumn SON) and hour (00 UTC, 06 UTC, 12 UTC and 18 UTC in blue, red, green and orange respectively).

sign in the anomalies corresponds to $[\vec{\nabla} \cdot \vec{Q}]$. The second PC explains 20% of the total variance, and it basically represents the variability of $[P]$ with a much weaker contribution (with opposite sign) of $[E]$ and $[\frac{\partial W}{\partial t}]$. Finally, the third PC represents only 6% of the total variance. It projects almost exclusively onto $[E]$, and its time-series shows a clear seasonal pattern with higher values during summer. It explains 77% of the variability of $[E]$. However, since neither of these PCs nor the original variables are strongly linearly related with the residual, there is no simple explanation for their area-averaged values.

3.5 Analysis of the Analysis Increments

It seems reasonable to think that the data assimilation step is the main cause of the six-hourly changes of the residual. In order to analyse its role in the structure of the residual, Figure 3.26 shows the distribution of the analysis increment of the specific humidity at 2 m during the data assimilation process at different times and seasons. Large analysis increments in moisture at 12 UTC and 18 UTC for each season were observed. During winter, the analysis increment occurs mainly at 12 UTC and not at 18 UTC. As stated by the box and whiskers, the spatial pattern at 12 UTC was more intense than that at 18 UTC. In both cases, great values in the south of Madrid, southeastern IP and Ebro and Guadalquivir basins can be found. It is clear that the differences between seasons were highlighted, with strong increments in summer, but less during winter. However, the spatial pattern was constant in every season.

The distribution of the analysis increments of the specific humidity at model's averaged 6, 7 and 8 vertical levels (near surface, approximately at 875 hPa) is presented in Figure 3.27. The data assimilation systematically removes moisture at this level, particularly when data from the soundings across the IP are available. As stated in section 2.1, the radiosondes are available at 00 UTC and 12 UTC (except for Lisbon that is only available at 12 UTC). Their effect is clearly visible as the bull-eye structure appear in those locations at the same time. At 06 UTC, when no sounding is available, the effect of the data assimilation is strongly reduced as the pressure is reduced. Above 100 hPa (averaged 30, 31 and 32 model's vertical levels), small increments in moisture (smaller than 1×10^{-7} kg/kg) appear particularly at 00 UTC and 12 UTC.

Regarding the analysis minus background of the temperature at 2 m, according to Figure 3.28, the most remarkable increments were observed at 00 and 12 UTC of every season. They occurred particularly in the south of the IP during winter, reaching the Cantabrian Range in summer. The assimilation substantially corrects the well known cold bias in summer temperatures observed in the IP for WRF simulations (*Fernández et al., 2007; Argüeso et al., 2011; Jerez et al., 2012*).

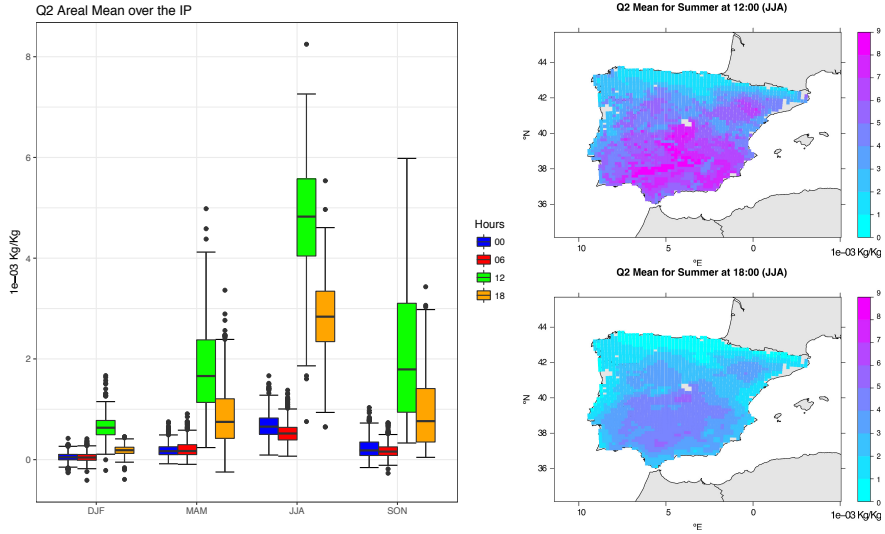


Figure 3.26: Left: Areal mean over the IP of the analysis minus background of the specific humidity at 2 m (in 1×10^{-3} kg/kg) according to the season (winter DJF, spring MAM, summer JJA, autumn SON) and hour (00, 06, 12 and 18 UTC in blue, red, green and orange respectively). Right: Spatial distribution of the analysis minus background during summer at 12 UTC (top) and 18 UTC (bottom).

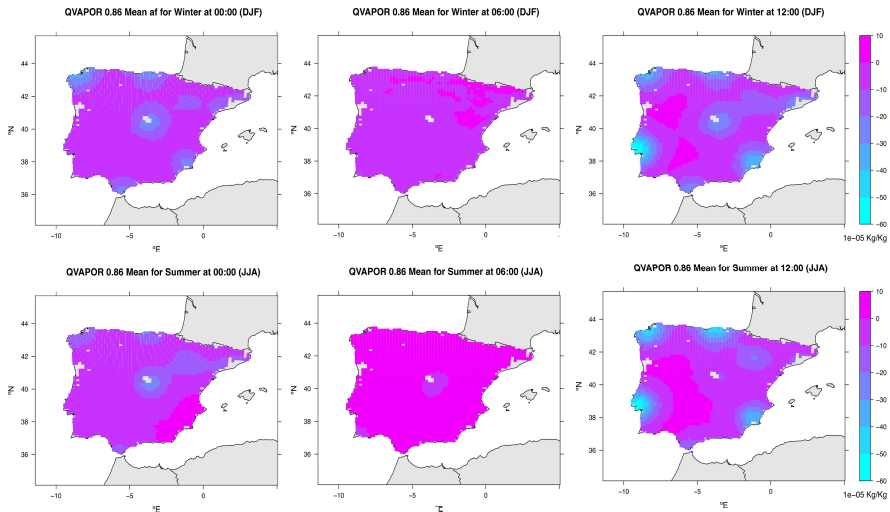


Figure 3.27: Spatial distribution of the analysis minus background of the specific humidity near 875 hPa at 00 UTC, 06 UTC and 18 UTC during winter (top) and summer (bottom).

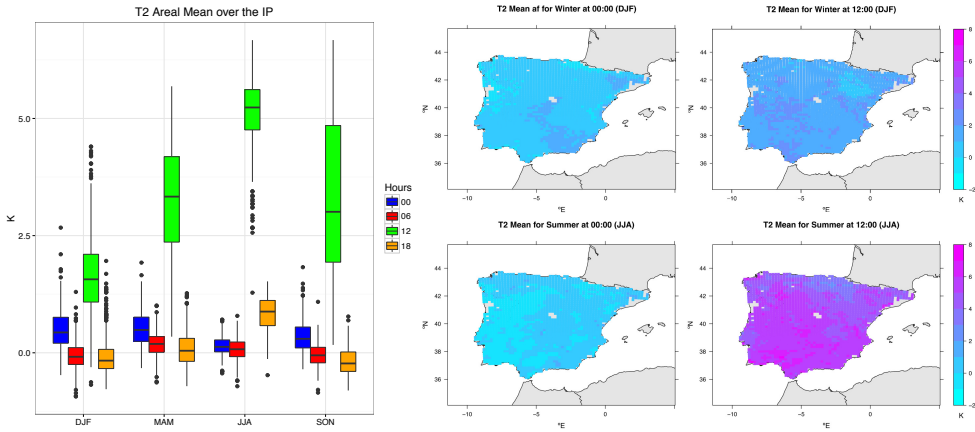


Figure 3.28: Left: Areal mean over the IP of the analysis minus background of the temperature at 2 m according to the season (winter DJF, spring MAM, summer JJA, autumn SON) and hour (00, 06, 12 and 18 UTC in blue, red, green and orange respectively). Right: Spatial distribution of the analysis minus background during winter at 00 and 12 UTC (top), and during summer at those same hours (bottom).

3.6 Description of the main features of the hydrological cycle

The D experiment accurately simulates the structure of the hydrological cycle over the IP. This section focuses on the main features of this cycle described by this experiment. The accumulated annual values of evaporation did not show a clear pattern over the IP. However, checking the mean daily values of evaporation for winter and summer (Figure 3.29), some interesting features can be observed. The evaporation of the IP is really small during winter (0.67 mm/day on average). The largest values are located in the south of Portugal for that season. During summer, conversely, remarkable values (above 4 mm/day) are observed in the north and north-western IP, the areas where the soil has the highest moisture content in that season. No special structures were observed for the evaporation during spring and autumn.

The influence of the Atlantic sources of moisture was recognizable in the precipitation (Figure 3.30). The D experiment obtained a similar pattern to that obtained by AEMET for period 1971-2000 (AEMET, 2011). In both cases, the smallest values appeared in the southeastern IP and the largest in the northwestern region and near the mountain ranges. This pattern was not so recognizable for the EOBS dataset, as the mountain precipitation is not captured by its coarse spatial resolution. A good agreement between the D experiment and ECA&D dataset was observed. The precipitation is underestimated by the D experiment only in some stations of the southwestern IP, probably related to the difficulties simulating the convective pre-

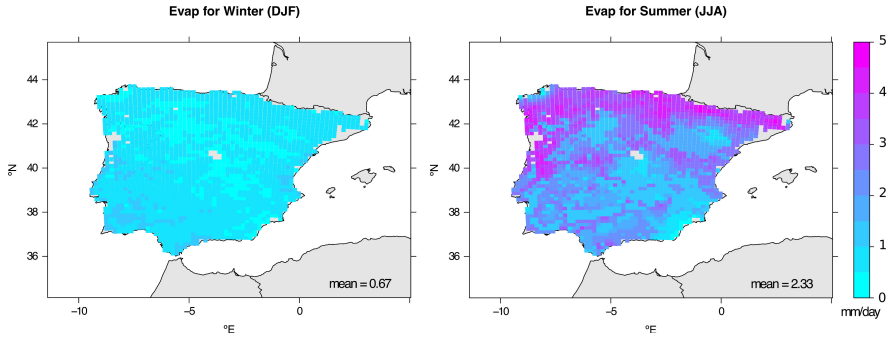


Figure 3.29: Mean daily evaporation (mm/day) simulated by the D experiment over the IP for winter (left) and summer (right). The mean value of the evaporation over the IP is presented in the right bottom corner of the maps.

precipitation regimes that dominate this region.

The seasonal variability of the PW was also analysed in Figure 3.31. The PW showed higher values in the Mediterranean coast and the Ebro basin during summer. Remarkable values were also observed near the Bay of Biscay. During the other seasons, especially spring and autumn, the PW values were higher in the most important basins of the IP: Guadalquivir, Guadiana, Tagus and Ebro basins. The smallest values were located near the mountain ranges during winter, as could be expected

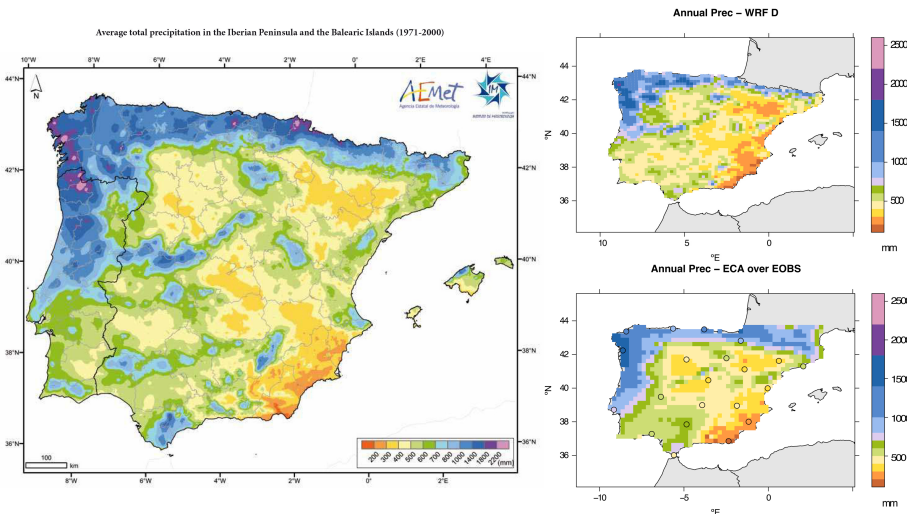


Figure 3.30: Accumulated annual precipitation (mm) over the IP taken from the Spanish Meteorological Agency atlas (*AEMET*, 2011) for 1971-2000 (left), compared to those from the D experiment (top right) and from ECA&D and EOBS (bottom right).

3.6 Description of the main features of the hydrological cycle

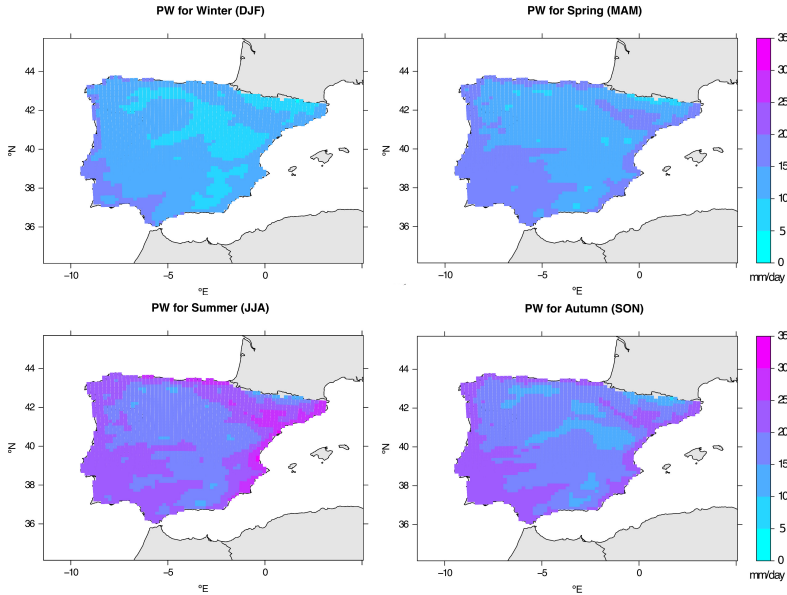


Figure 3.31: Mean daily PW (mm) simulated by the D experiment over the IP for winter (top left), spring (top right), summer (bottom left) and autumn (bottom right).

from the lower temperatures at low levels of the atmosphere and the smaller height of the troposphere at those places.

An advantage of using a model such as WRF is that new fields that cannot be estimated from observations alone can be studied. This is the case of the moisture that crosses the boundaries of the IP. Figure 3.32 shows the transboundary moisture fluxes across the boundaries of the IP during winter as simulated by the D experiment. According to the net values of each studied hour (00 UTC, 06 UTC, 12 UTC and 18 UTC), the IP imports a great amount of moisture during this season. The overall net flux is always negative, in the range of -34.35 Pg/mon and -12.7 Pg/mon for day and night respectively. The moisture enters the IP mainly through the Portuguese coast and exits the peninsula through the Mediterranean coast. During spring, the IP exports moisture at night (30 Pg/month), but imports it during the day (-27 Pg/mon).

During summer (Figure 3.33), the IP exports moisture during the whole day (net flux always positive ranging from 48 to 68 Pg/mon) except at 12 UTC and 15 UTC that the IP moisture flux is negative (-0.34 and -8 Pg/mon respectively). At those times, moisture is imported specially because of the breezes in the Alboran Sea (southern Spain) (see 06 UTC versus 18 UTC plots). This breeze reaches its maximum intensity slightly later than 12 UTC. During Autumn, the IP mainly imports moisture, with the net flux ranging from -31 Pg/mon to 4 Pg/mon. As stated by *Berberly and Rasmusson (1999)*, a similar behaviour to that for the IP was observed

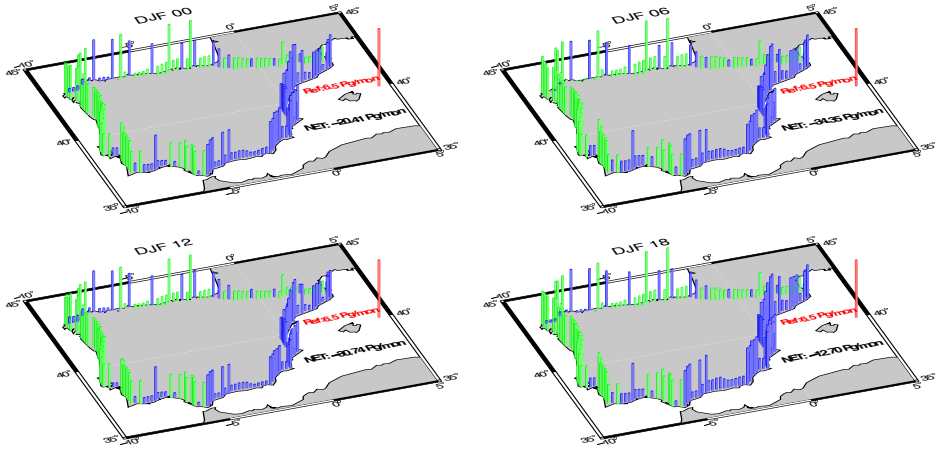


Figure 3.32: Transboundary moisture fluxes analysis at 00 UTC (top left), 06 UTC (top right), 12 UTC (bottom left) and 18 UTC (bottom right) during winter. The reference bar is labelled at 6.5 Pg/month. The green bars represent an inland flux, while the blue bars refer to an outward flux.

in the United States.

The discussion of these results will take place in chapter 7. The discussion will focus mainly on different topics such as the length of the spin-up in our experiments, the effect of the data assimilation on the results, the representativeness problem, the coarse resolution of the validation datasets, the *urban or built-up* grid points discovered during the validation of evaporation and the breezes.

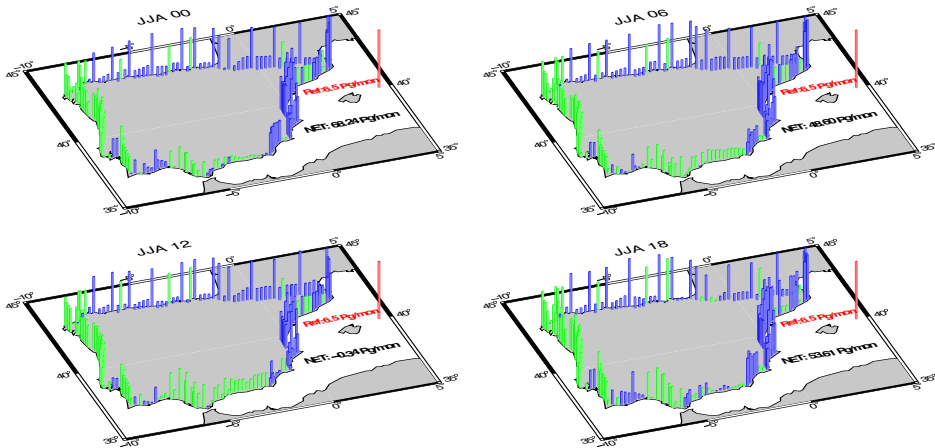


Figure 3.33: Same as Figure 3.32 but for summer.

4

Comparison of Downscaling Precipitation Models

THIS chapter focuses on the optimal calibration of the Statistical DownScaling Model (SDSM) and the comparison of the daily precipitation downscaled by this model and both WRF simulations (N and D experiments).

As different strategies were used to calibrate the SDSM, some comparisons between SDSM experiments were carried out in order to study the predictor suites created for each of them, the effect of reducing the calibration period, changing the source of the predictors or enhancing the resolution of the reanalysis used as source of the predictors on the downscaled precipitation. These results are presented in sections 4.1 and 4.2. Finally, the most similar SDSM experiment to the configuration used in WRF was compared to both WRF simulations in section 4.3, with our main objective here being to determine the best downscaling model.

4.1 Analysis of the predictor suites

As previously stated in Table 2.1 from chapter 2, four SDSM experiments were carried out with SDSM. In order to create a fair comparison between them, four different predictor suites were created¹. Taking into account that 21 stations were selected over the IP and that there are 16 permutations of experiment-predictor suite, 336 downscaled precipitation time series would be created using SDSM. Hence, 672 comparisons would be needed to carry out with both WRF simulations. The potential dimensionality of an exhaustive analysis would be very large so, in order to manage the degrees of freedom, two representative predictor suites were selected.

The four predictor suites were evaluated as follows: the N48 suite was compared to that from N79. The number of selected input predictors reduces by 6% from 125 predictors in N48 to 118 in N79. Fourteen stations retain the same predictors sets in both suites. In the remaining cases, differences between suites are due to reductions in the number of predictors used for calibration (e.g. Murcia, Albacete and Castellón de la Plana) or changes between predictors at different vertical levels. For example, Tarifa uses the wind strength at 850 hPa in the N48 predictor suite instead of 500 hPa in N79.

There is also a reduction in the number of input predictors when comparing the E79 and E79r suites. In this case, 132 predictors are used in E79 predictor suite and 113 in E79r suite (-14%). Nine stations have the same predictors in both suites. In the other stations (e.g. A Coruña, Santander, Tarifa, Cáceres and Albacete), there are fewer input predictors. Only Barcelona station has a new predictor in E79r compared to E79. This suggests that improving the resolution of the reanalysis, reduces the number of predictors needed to calibrate SDSM.

There is more than 85% overlap between the various predictor suites. In order to maximise the parsimony of the input predictors (*Wilby and Wigley, 2000*) and consistency in the reanalysis resolution, suites N48 and E79 were selected. Hereafter, both suites are named after the reanalysis used on their corresponding experiments: the predictor suite based on the N48 experiment refers to the ‘NCEP predictor suite’ and E79 to the ‘ERA predictor suite’.

4.2 Comparison of SDSM experiments

The R² values obtained by SDSM for each experiment when applying both NCEP and ERA predictor suites are presented in Figure 4.1. For the N48 experiment, where

¹All of the predictor suites created can be found on the Appendix A.

SDSM is calibrated for period 1948-2009 using inputs from NCEP, a similar pattern is observed for both predictor suites. The best scores are obtained in the northwestern and southern IP, while the worst appeared near the Mediterranean sea (particularly in Barcelona). However, according to the mean values of the 21 stations, the ERA predictor suite produced slightly better scores than NCEP predictor suite (15.23% and 16.13% respectively, but not significant at 95% confidence level).

If the calibration period is reduced (1979-2009) but the inputs from NCEP are maintained (N79 experiment), the R2 achieved for NCEP and ERA predictor suites are 17.16% and 18.31% respectively. In other words, the use of the more recent predictors yields higher validation skill scores. There are only three occasions when R2 improves for the longer (i.e. 1948 onwards) calibration period: Madrid, Huelva and Almería stations for the NCEP predictor suite; Lisbon, Madrid and Almería for the ERA suite. Overall, the improvements in R2 appeared near the Mediterranean Coast. The stations in the northwestern (Cantabrian) coast yield the best scores.

Changing the inputs from NCEP to ERAI but keeping the same calibration period as in previous experiment (1979-2009), E79 obtained a mean R2 of 17.96% and 19.87% when using the NCEP and ERA predictor suites respectively. Some interesting features are observed in the southwestern zone, particularly for Huelva and Córdoba where significant improvements appeared. There are declining R2 values in stations such as Lisbon, Barcelona and Tarifa when using the NCEP predictor suite.

Using the best resolution of ERAI as inputs for SDSM (E79r experiment), the best R2 scores are reached. For both predictor suites, the best R2 values were obtained in northwestern Spain, particularly in A Coruña and Gijón. However, values above 15% are observed on each station of the IP using both predictors suites (with the exception of Lisbon and Barcelona when using the NCEP suite).

Then, it seems clear that the best calibration scores are obtained for the E79r experiment using the ERA predictor suite. However, the significance of these differences must be evaluated. To do so, the bootstrap technique with resampling was applied to each experiment. Two stations from the twenty-one available were selected to show the results: Lisbon and Cáceres.

The Taylor diagrams for each SDSM experiment on Lisbon station are presented in Figure 4.2. Small improvements are observed between experiments when reducing the calibration period, changing to ERA inputs or enhancing the resolution of the reanalysis, particularly for the E79r experiment. The E79r experiment improves the correlation and SD if the ERA predictor suite is used ($r=0.6$), but the correlation is reduced while using the NCEP suite ($r=0.5$). The mean of the ensemble created by SDSM (SDSM mean) improves always the correlation obtained by each member of the ensemble independently (between 0.3 and 0.5), but not the SD. The RMSE is also better for the SDSM mean on each experiment. The bootstrap technique shows that differences between both predictors suites arise for E79 and E79r experiments. Apart from Lisbon, no overlapping shaded regions of the bootstrap technique are observed for Huelva, Albacete, Barcelona, Castellón de la Plana or Lleida.

On the other stations, as shown for instance using Cáceres, no significant differences between experiments are observed on the results from the bootstrap technique

4.2 Comparison of SDSM experiments

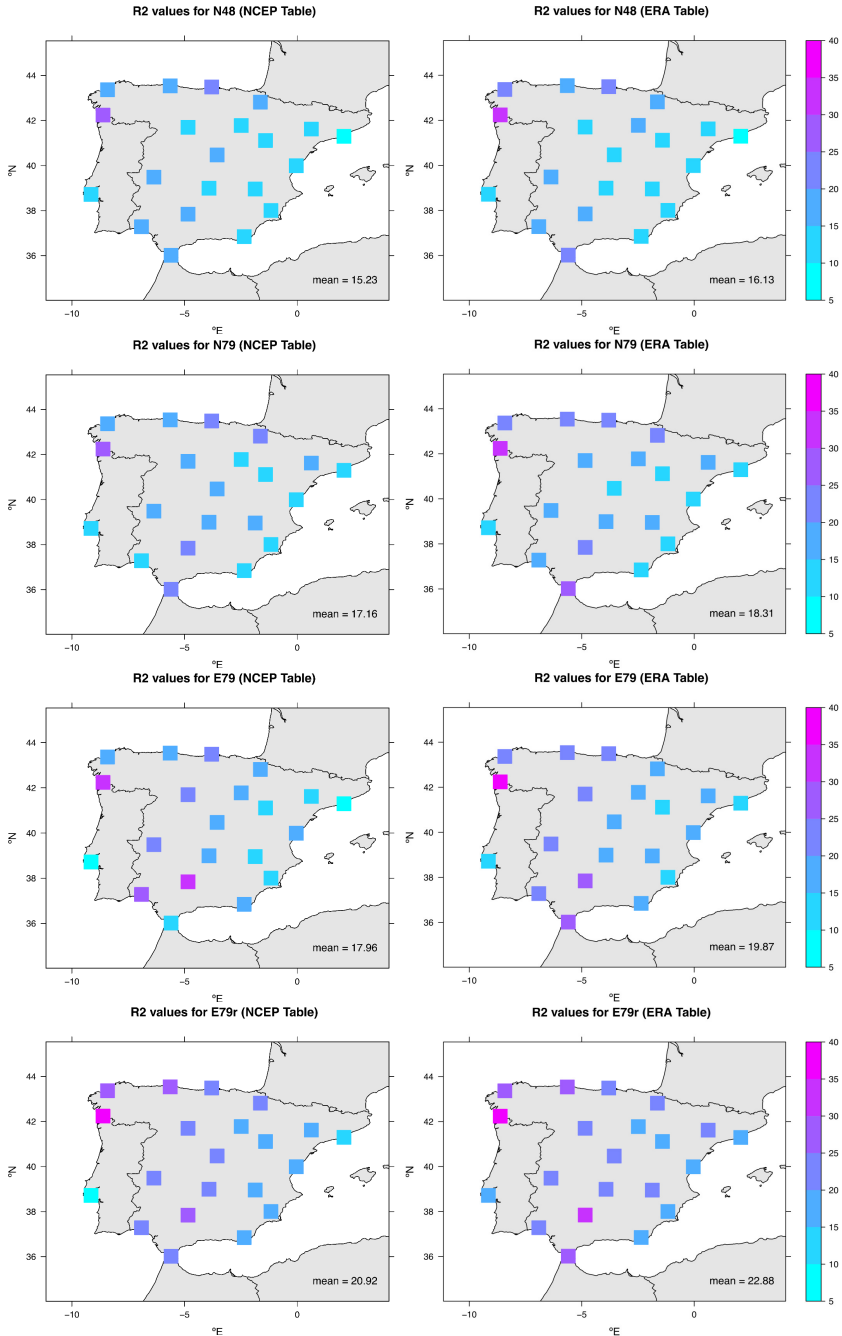


Figure 4.1: Spatial distribution of the R2 (expressed in %) obtained by SDSM for N48, N79, E79 and E79r experiments (first, second, third and fourth rows respectively) calibrated following the NCEP and ERA predictor suites (left and right respectively). The mean R2 value is presented in the right bottom corner of each map.

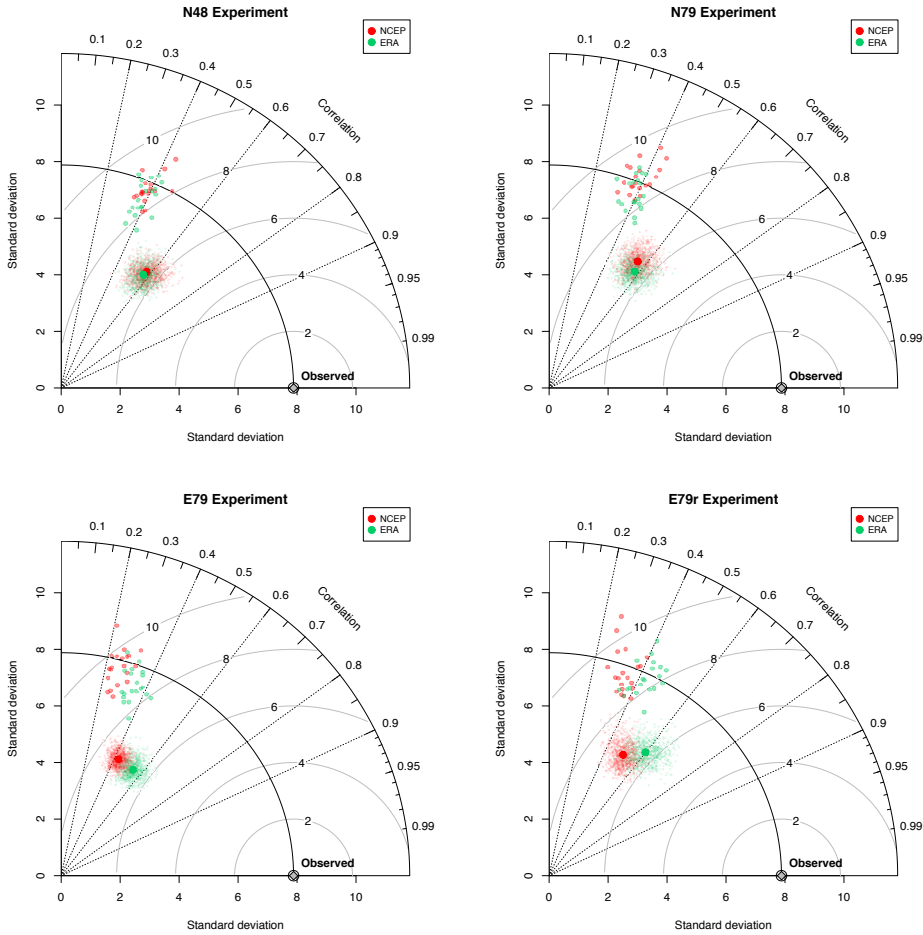


Figure 4.2: Taylor diagrams for Lisbon station showing the differences between applying the NCEP (red) and ERA suite (green) on N48 (top left), N79 (top right), E79 (bottom left) and E79r experiments (bottom left). In each panel, the SDSM ensemble mean (big dot), SDSM ensemble members (light dots) and the observed station data (grey diamond) are shown. The results for the 1000 new time-series created by the bootstrap technique with resampling are also plotted with small diamonds.

(Figure 4.3). Small improvements in correlation and RMSE (not SD) are still observed for the experiments when changing to ERA predictor suite, particularly when the E79r is selected, but there are no significant differences between them.

The significance of the results was also studied by means of the ROC curves of the ensembles created by SDSM for each experiment and station. The ROC curves

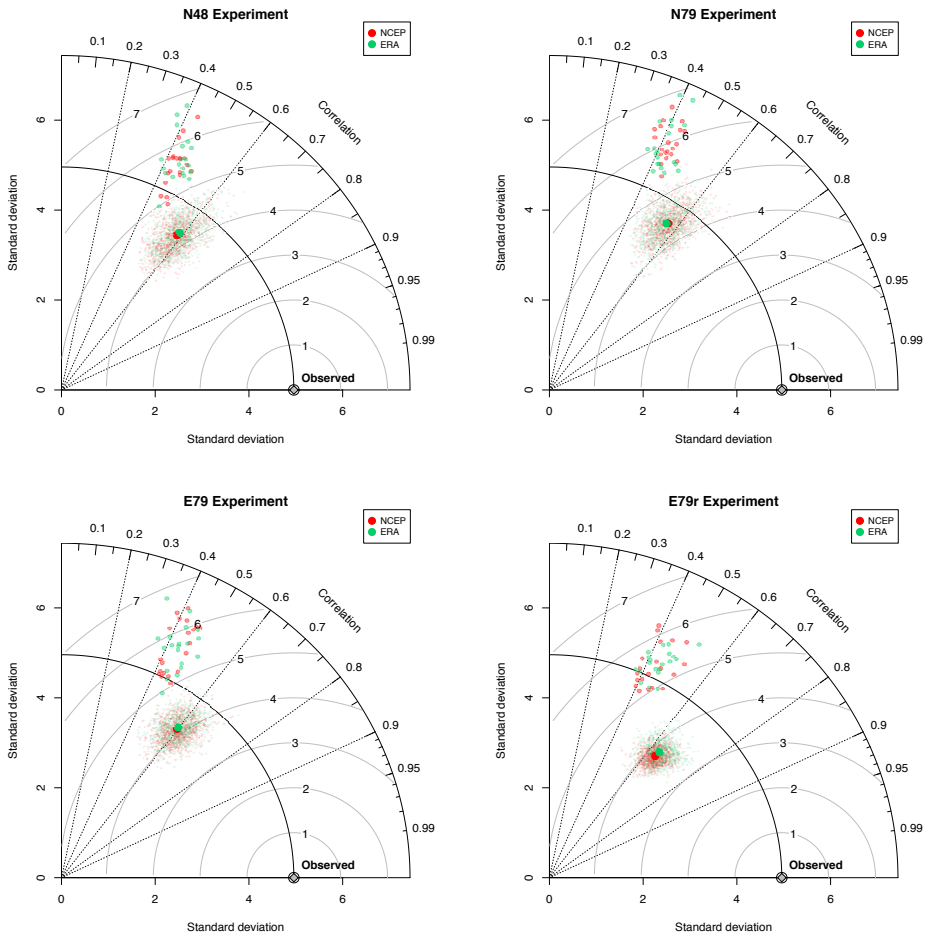


Figure 4.3: Same as Figure 4.2 but for Cáceres.

for the ensemble means at Lisbon are presented in Figure 4.4. Small differences on the central part of the ROC curves appear for both predictor suites. For the NCEP suite, the best AUC score is obtained by the N79 experiment (0.391), but for the ERA suite it is reached for the E79r experiment (0.393). In both cases, the worst results are obtained by the E79 experiment. Differences between the ROC curves are observed for other stations apart from Lisbon, such as Albacete, Tarifa, Barcelona, Gijón, Madrid and Daroca.

For the rest of the stations, no significant differences between the ROC curves are observed, such as for Cáceres (Figure 4.5). In this station, the best AUC scores are obtained by the E79 experiment when using the NCEP (0.404) and ERA suites

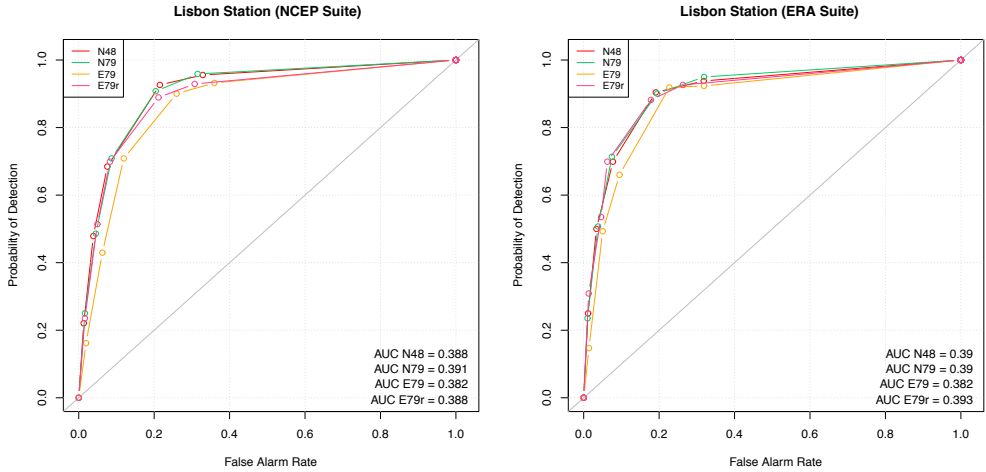


Figure 4.4: ROC curves for the ensemble mean of each experiment at Lisbon stations while using the NCEP (left) or ERA (right) predictor suites. The N48, N79, E79 and E79r are coloured by red, green, orange and magenta lines respectively. The AUC of each experiment is stated in the right bottom corner of the plots.

(0.406). However, the E79r is close to that experiment in both cases (0.401 and 0.405 respectively).

The distribution of the AUC scores obtained by the 21 stations over the IP was also studied by means of a box and whisker chart (Figure 4.6). The best scores

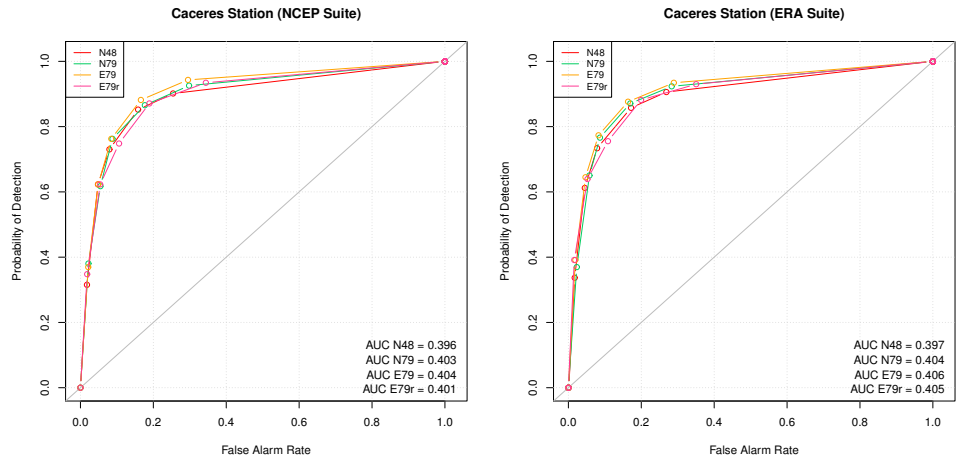


Figure 4.5: Same as Figure 4.4 but for Cáceres.

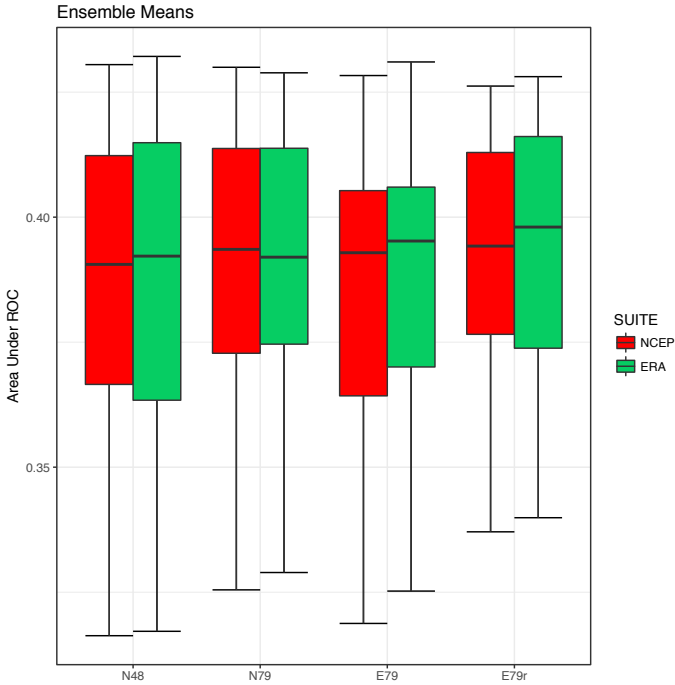


Figure 4.6: Distribution of the ROC curves for the 21 stations over the IP according to the SDSM experiment and predictor suite used (NCEP in red and ERA in green).

are obtained by the E79r experiment, followed by the E79 experiment. However, the differences are not significant enough and there is no proof that this experiment outperforms the others systematically and with enough statistical confidence.

4.3 Analysis of statistical and numerical downscaling models

For the comparison of statistical and numerical downscaling models, both WRF simulations were compared to the E79r experiment. It was calibrated on the SDSM with its own predictor suite as no statistical significance was found for the E79r experiment when applying the NCEP or ERA predictor suites. This way, the results are produced after calibrating the model with the optimal predictor suite designed for that experiment. This experiment is the most similar one to that configuration used in both WRF runs. That is, ERAI at 0.75° grid resolution is used as the boundary conditions on both WRF simulations and as the source of the predictors for SDSM.

The chosen twenty-one stations were divided into four regions according to the similarities between those included on each of them: Northern, Central, Mediterranean and SouthWestern regions (in blue, green, pink and orange respectively in Figure 4.7). These regions are similar to those defined by *Serrano et al. (1999)* and to the spatial patterns of annual precipitation obtained by *Rodríguez-Puebla et al. (1998)* from the analysis of the spatial variability in long observed series.

Figure 4.8 shows the predictor suite created for the E79r experiment. Precipitation was the only predictor used for every station. The downward shortwave radiation flux was used on twenty sites, and 850 and 500 hPa geopotential height on sixteen and ten stations respectively. Nine stations used as predictors the relative humidity at 500 hPa and the mean sea level pressure. Finally, both components of wind at 850 hPa were used on five stations, followed by meridional wind at surface and at 500 hPa on four stations and zonal wind at surface and at 500 hPa on three sites. Hence,

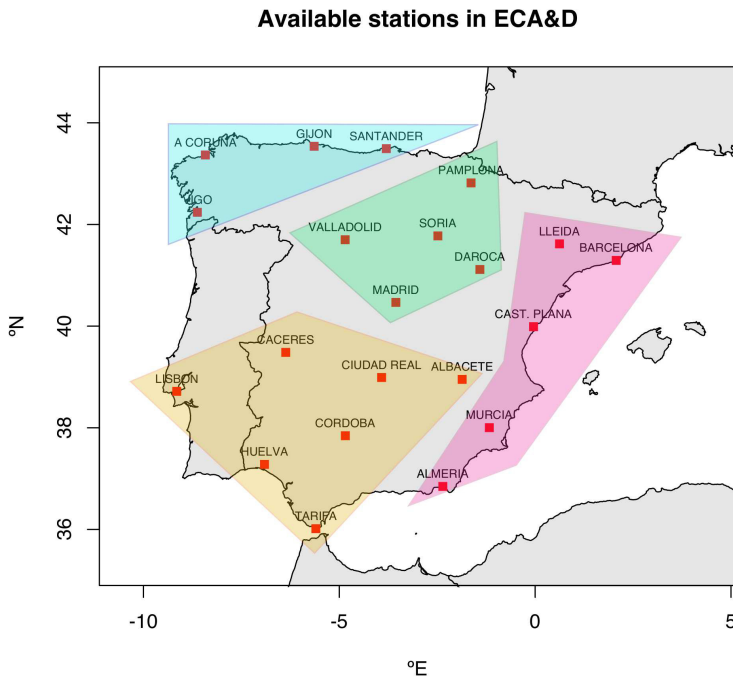


Figure 4.7: Location of the four regions defined according to the similar properties of the stations: Northern, Centre, Mediterranean and SouthWestern regions (in blue, green, pink and orange) respectively.

4.3 Analysis of statistical and numerical downscaling models

Experiment E79r – Predictor Suite

	DSWR	MSLP	USUR	VSUR	DSUR	F500	U500	V500	Z500	H500	D500	F850	U850	V850	Z850	H850	D850	PREC	R500	R850	RSUR
Vigo	1	1	0	1	0	0	1	0	0	1	0	0	1	0	0	1	0	1	0	1	1
ACoruna	1	0	0	0	0	0	1	0	0	0	0	0	0	0	0	1	0	1	1	0	0
Gijon	1	0	0	0	0	0	0	0	0	1	0	0	0	0	0	0	0	1	1	0	0
Santander	1	0	1	0	0	1	0	0	0	0	0	0	1	0	0	1	0	1	0	0	0
Pamplona	1	1	0	0	0	1	1	0	0	1	0	0	0	0	0	1	0	1	0	0	0
Soria	1	1	0	0	0	0	0	1	0	0	0	0	0	0	0	1	0	1	1	0	0
Valladolid	1	1	1	0	0	0	0	1	0	0	0	0	0	0	0	1	0	1	1	0	0
Madrid	1	1	0	0	0	0	0	1	0	0	0	0	0	0	0	1	0	1	1	0	0
Daroca	1	1	0	0	0	0	0	0	0	0	0	0	0	0	1	1	0	1	0	0	0
Lleida	1	1	0	0	0	0	0	1	0	0	0	0	0	0	0	1	0	1	1	0	0
Barcelona	1	0	0	0	0	0	0	0	0	1	0	0	0	0	0	1	0	1	0	0	0
Cast. Plana	1	0	0	0	0	0	0	0	0	1	0	0	0	0	0	0	0	1	0	0	0
Murcia	1	0	0	0	0	0	0	0	0	1	0	0	0	0	1	0	0	1	0	0	0
Almeria	1	0	0	0	0	0	0	1	0	0	0	0	0	0	0	0	0	1	0	0	0
Caceres	1	1	0	0	0	0	0	0	0	0	0	0	0	0	0	1	0	1	0	0	0
Ciudad Real	1	1	0	0	0	0	0	0	0	0	0	0	0	0	0	1	0	1	1	0	0
Albacete	0	0	0	0	0	0	0	0	0	1	0	0	0	0	0	1	0	1	1	0	0
Tarifa	1	0	0	1	0	0	0	0	0	1	0	0	1	0	0	0	0	1	0	0	0
Huelva	1	0	0	1	0	0	0	0	0	1	0	0	1	0	0	1	0	1	0	0	0
Cordoba	1	0	0	1	0	0	0	0	0	1	0	0	0	0	0	1	0	1	1	0	0
Lisbon	1	0	1	0	0	0	1	0	0	0	0	0	1	0	0	1	0	1	0	0	1

Figure 4.8: SDSM predictor suite for the experiment using inputs from ERAI at 0.75 degrees (E79r). The color used to define each station represents the region where they belong, namely: Northern (blue), Centre (green), Mediterranean (pink) and SouthWestern regions (orange). The colours are the same to those used in Figure 4.7. Acronyms of the predictors are defined as in *Wilby and Dawson (2013)*.

the state of the atmosphere, the incident radiation and the atmospheric moisture are taken into account by the SDSM during the calibration step.

A relationship between the region and the predictors used can be noticed in the predictor suite. According to Table 4.1, the favoured predictors for the northern region are the downward shortwave radiation flux, precipitation, geopotential at 850 hPa and zonal wind, relative humidity and geopotential at 500 hPa. For the centre

Table 4.1: Number of times that each predictor was used on each region. The most important values are highlighted using the color associated to each region of the IP: Northern in blue, Centre in green, Mediterranean in pink and SouthWestern region in orange. The same nomenclature as in Figure 4.8 was used here for naming the predictors.

Region	DSWR	MSLP	USUR	VSUR	F500	U500	V500	H500	U850	Z850	H850	PREC	R500	R850	RSUR
North (4)	4	1	1	1	1	2	0	2	2	0	3	4	2	1	1
Centre (5)	5	5	1	0	1	1	3	1	0	1	5	5	3	0	0
Mediterranean (5)	5	1	0	0	0	0	2	3	0	1	2	5	1	0	0
SouthWest (7)	6	2	1	3	0	1	0	4	3	0	6	7	3	0	1

of the IP, the downward shortwave radiation, precipitation and relative humidity at 500 hPa are important predictors along with the mean sea level pressure and meridional wind at 500 hPa. The radiation, precipitation, zonal wind at 500 hPa and geopotential at 500 and 850 hPa seemed to be important for the Mediterranean. Finally, in the southwestern IP, radiation, geopotential at 850 hPa and precipitation must be included, but also the meridional wind at surface, geopotential at relative humidity at 500 hPa and zonal wind at 850 hPa.

The predictors included in the predictor suite for the E79r experiment were divided in three groups according to the latitude, longitude, elevation and annual precipitation during 1980-2010 in order to check the dependency of the frequency of predictor variable selection on these variables by means of a χ -squared test. No statistically significant site-dependencies in the predictor suite were identified. This finding suggests that the optimum predictor set cannot be inferred from this kind of properties and that each station has to be calibrated independently.

After running the SDSM with the above mentioned predictor suite, the explained variances (R2) reached at the stations for calibration period were saved. The spatial distribution of the R2 is presented in Figure 4.9. The R2 varied between 15% and 40% and the mean value is 22%. Two stations are highlighted in the map because of their scores: Vigo and Córdoba, with 39% and 32% respectively. These values of R2 were similar to those gathered by *Gulacha and Mulungu (2017)* for different domains and periods. The poorest results were observed in the Mediterranean coast of the IP, particularly near the Ebro basin and in Barcelona. Conversely, the best results appeared near the Cantabrian coast. A northwest-southeast dipolar pattern is highlighted in these results, related to how well the precipitation types (large-scale or convective, that is, Atlantic or Mediterranean) are simulated by RCMs over the IP. These results are similar to those obtained by *Goodess and Palutikof (1998)*.

Starting by the Northern region, it includes four stations, namely: A Coruña, Vigo, Gijón and Santander. The Taylor diagram for Gijón is presented in Figure 4.10. This station is the one representative of the results for the region¹. The correlation

¹The Taylor diagrams for the other stations can be found in Figure B.1 from the Appendix B.

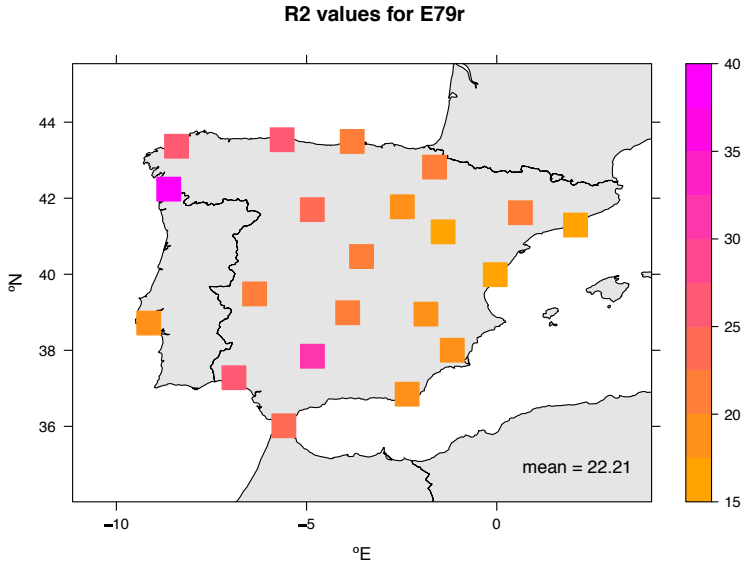


Figure 4.9: Explained variance (in %) achieved for the calibration period by the SDSM for the experiment including predictors from ERAI at 0.75 degrees (E79r). The mean value is presented in the bottom right corner of the figure.

obtained by the SDSM mean and D range between 0.6 and 0.8. However, the D experiment outperforms SDSM mean in the SD. Similar results are measured for ERAI and N, but not as good as those for SDSM and D as their correlation ranges between 0.4 and 0.65. The EOBS dataset reaches the best correlation score (0.95), but TRMM and GPCP (observational datasets too) range between 0.3 and 0.4 and their RMSE is much worse than those for the downscaling experiments. The ensemble members overestimate the SD and their correlation range between 0.3 and 0.5 in every station of the Northern region, while the ensemble mean underestimates the SD but improves the correlation and RMSE.

The centre of the IP comprises five stations: Pamplona, Soria, Madrid, Valladolid and Daroca. The most representative stations of the region are Soria and Madrid, and their Taylor diagrams are presented in Figure 4.11¹. Similar correlations for D, ERA and SDSM mean were observed, ranging between 0.5-0.7, 0.4-0.6 and 0.5-0.6 respectively. The SD is underestimated by D, ERAI and SDSM mean in Soria and Pamplona, but it is correctly simulated only by D and ERAI in Madrid, Valladolid and Daroca. The EOBS dataset outperforms the other datasets and achieves correlations above 0.9 in every station. The TRMM achieved better results than the GPCP, but not as good as our downscaling experiments. Some ensemble members are able to reproduce the observed SD, but usually they overestimate it. Additionally, their correlation is worse than the one obtained by the ensemble mean.

¹Every Taylor diagram for the Central IP can be found in Figure B.2 from the Appendix B.

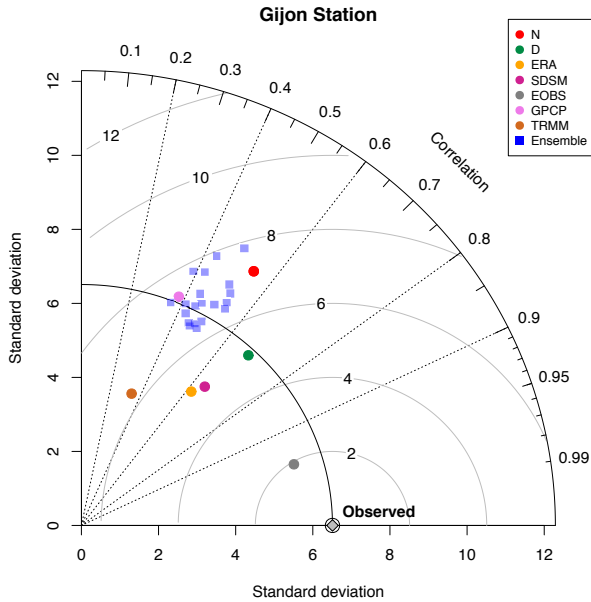


Figure 4.10: Taylor diagram for Gijón Station, representative of the Northern Region. Five experiments can be found on it: WRF N (red), WRF D (green), ERAI (orange), the SDSM ensemble mean (magenta), EOBS (grey), GPCP (violet) and TRMM (brown). Observed station data (grey diamond) and the members of the ensemble created by SDSM (blue squares) are also shown.

The Mediterranean region consists of five stations: Lleida, Barcelona, Murcia, Almería and Castellón de la Plana. Here, the most representative stations of the region¹ are Lleida and Murcia, and their corresponding Taylor diagrams are presented in Figure 4.12. The correlations for D, ERAI and SDSM mean range between 0.4 and 0.6, but the RMSE is better for D and SDSM mean compared to the other datasets. Again, the EOBS dataset obtained the best correlation, contrasting the results shown by the other observational datasets (TRMM and GPCP). The correlations of the ensemble members range between 0.3 and 0.5, but they tend to overestimate the SD in most of the stations, with the exception of Lleida and Barcelona where the observed SD is quite well reproduced.

Seven stations belong to the Southwestern region of the IP: Lisbon, Ciudad Real, Cáceres, Albacete, Córdoba, Huelva and Tarifa. Figure 4.13 shows the Taylor diagrams for Lisbon and Albacete stations, representative of the region². The correla-

¹The Taylor diagrams of each station in the region can be found in Figure B.3 from the Appendix B.

²The Taylor diagrams for the region can be found in Figure B.4 from the Appendix B.

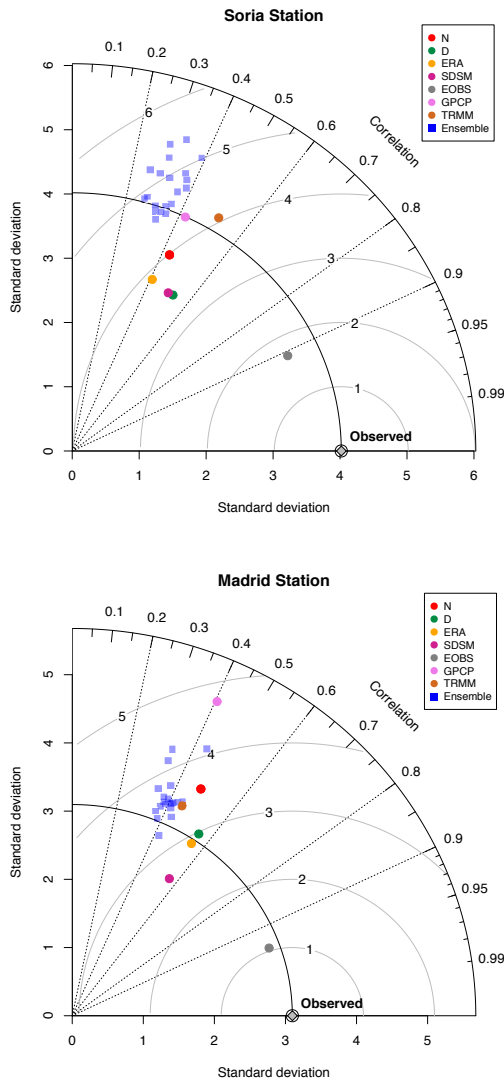


Figure 4.11: Same as Figure 4.10 but for Soria (top) and Madrid (bottom) stations, representative of the Central IP.

tions for D, ERAI and SDSM mean range between 0.5 and 0.6, but the D experiment reaches 0.7 in Tarifa while the others obtained 0.55. Surprisingly, the N experiment obtained comparable correlations (0.6) to D, ERAI and SDSM mean in Lisbon. Additionally, most of the experiments and datasets underestimate the measured SD,

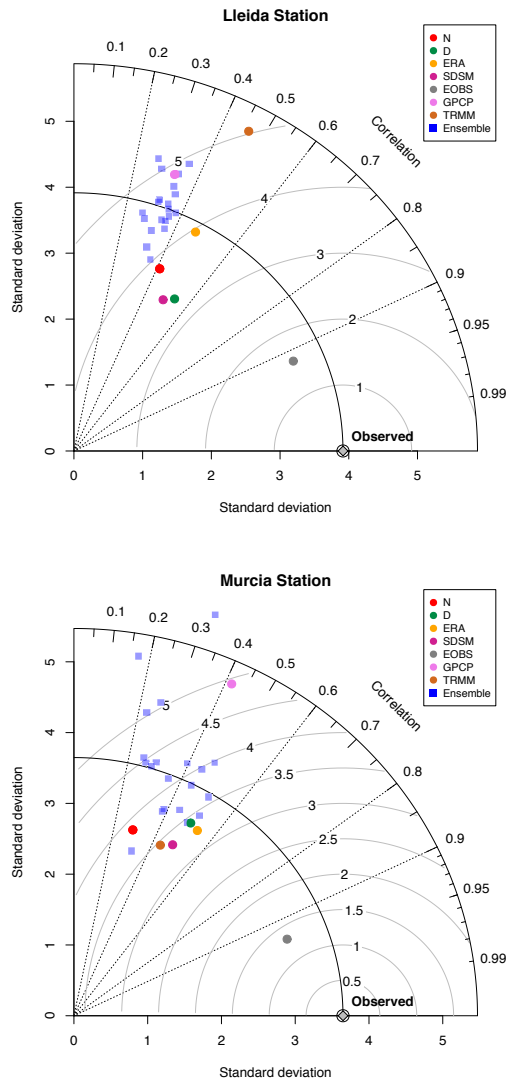


Figure 4.12: Same as Figure 4.10 and 4.11 but for Lleida (top) and Murcia (bottom) stations, representative of the Mediterranean Region.

particularly in Lisbon, Córdoba and Albacete. The ensemble members underestimate the observed SD and their correlations range between 0.3 and 0.5. As in the other regions, the EOBS dataset obtains the best scores and the TRMM and GPCP the worst. However, in this region, these two observational datasets are closer to the

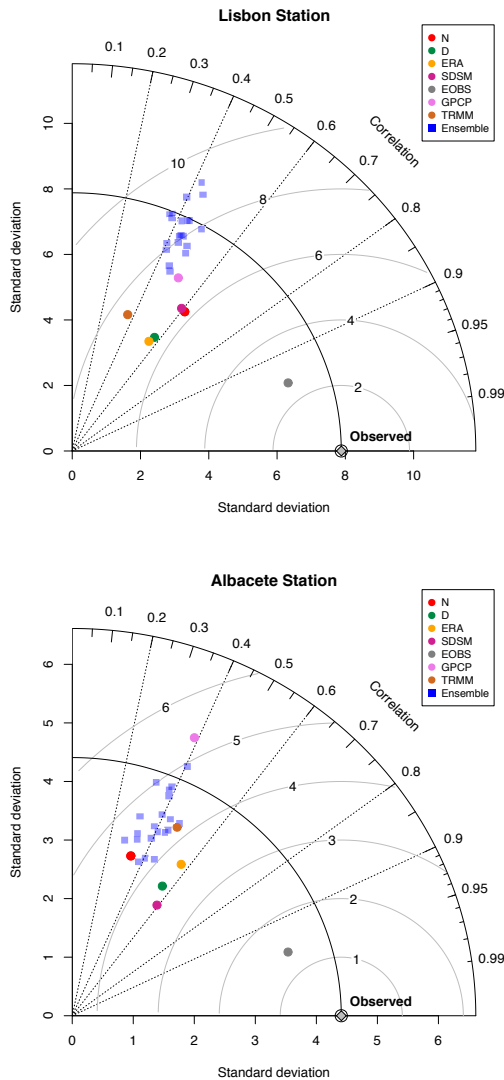


Figure 4.13: Same as Figure 4.10, 4.11 and 4.12 but for Lisbon (top) and Albacete (bottom) stations, representative of the Southwestern region of the IP.

other studied experiments and datasets.

The significance of these results was studied by means of the bootstrap technique (with resampling). The distribution of the correlations obtained by 1000 new time-series is presented in Figure 4.14. As previously stated, the EOBS dataset is the one

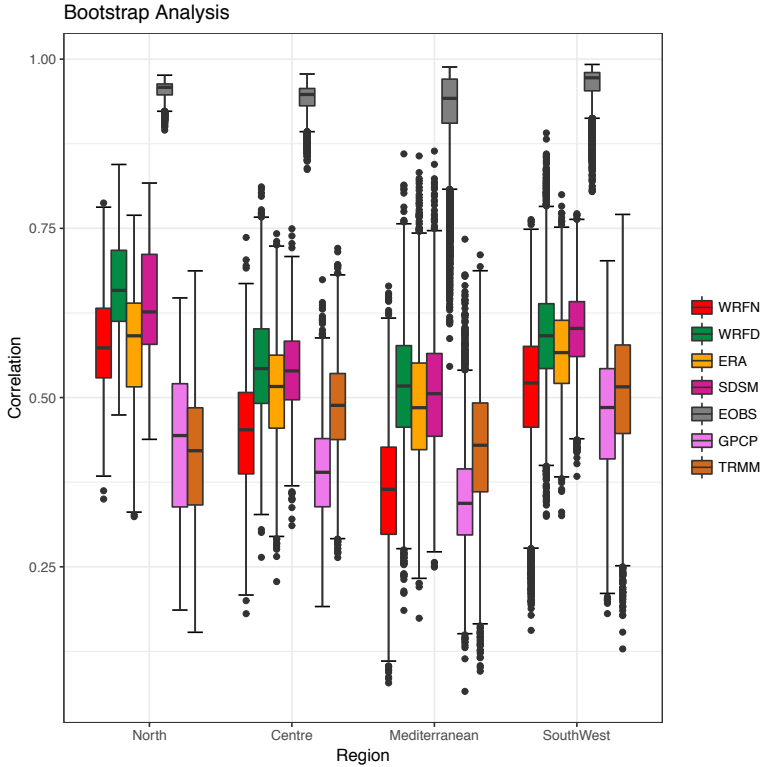


Figure 4.14: Correlations between each experiment/dataset and the corresponding observed precipitation amount. 1000 time-series with daily temporal resolution were created by the bootstrap technique with resampling. The results are plotted according to the region. As in previous figures, WRF N, WRF D, ERAI, the SDSM ensemble mean experiments and EOBS, GPCP and TRMM datasets are coloured in red, green, orange, magenta, grey, violet and brown respectively.

with the best scores on each region of the IP. Conversely, the GPCP and TRMM (alternative observational datasets) obtained the worst results. These observational datasets delimit the values of the correlations as the remaining experiments are found between them. Additionally, comparing both WRF datasets, the D experiment (with data assimilation) outperforms the N experiment (without data assimilation), particularly in the Mediterranean region. Similar correlation values are obtained by D, ERAI and SDSM ensemble mean on each region, but the spread of the values for ERAI tend to be a little bit lower than those for SDSM and D, particularly in the northern region.

According to these results, it is clear that the Taylor diagrams and the bootstrap technique are not enough to differentiate which downscaling experiment (the D exper-

iment or the SDSM mean) would be the best at simulating the precipitation measured over the IP. Then, the LEPS, the BSS and some commonly used precipitation indices were calculated at each station in order to determine the best experiment.

The LEPS for D, SDSM mean and ensemble members compared to the observed precipitation at each station (D-STAT, SDSM-STAT and Ensemble-STAT respectively) is presented in Figure 4.15. Comparing D and SDSM mean, the D experiment outperforms the SDSM mean in every station with the exception of Vigo where D obtains 0.0125 and SDSM mean 0.0093. Conversely, the members of the ensemble outperform the D experiment in most of the stations. The D experiment is able to beat the ensemble members only in five of the twenty-one chosen stations: Santander (from northern region), Castellón de la Plana (included in the Mediterranean region), Tarifa, Córdoba and Lisbon (from the southwestern IP).

Figure 4.16 shows the BSS for D, SDSM mean and ensemble members. Both D and SDSM mean present added value compared to ERAI, particularly the SDSM

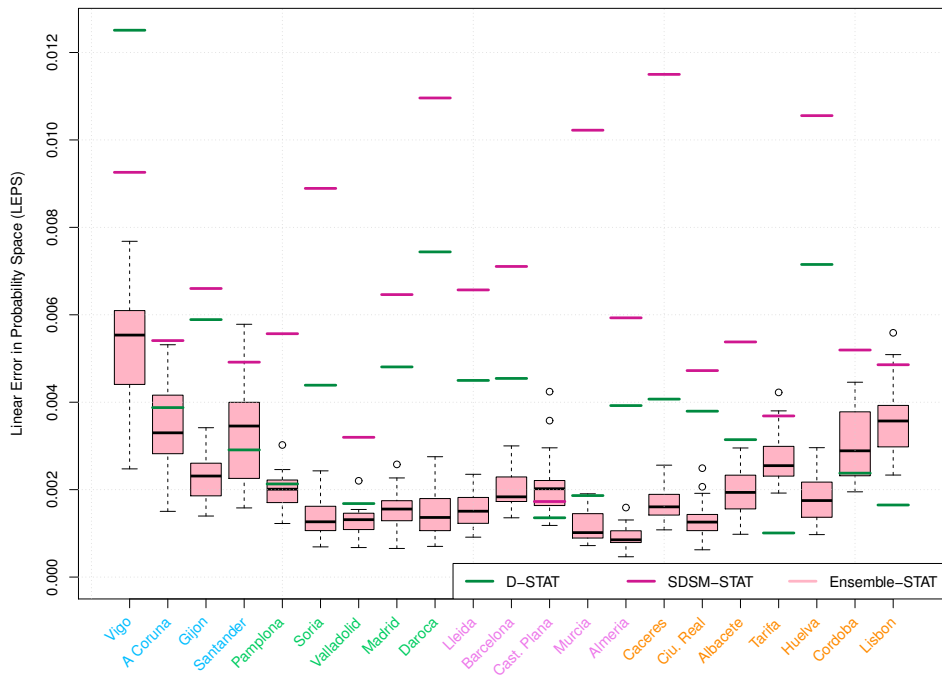


Figure 4.15: LEPS scores for WRF D (green), SDSM mean (magenta) and each member of the ensemble (light pink boxes) computed at each station. The names of the stations are coloured according to the region were they belong: Northern, Central, Mediterranean or Southwestern region (in cyan, green, magenta and orange respectively).

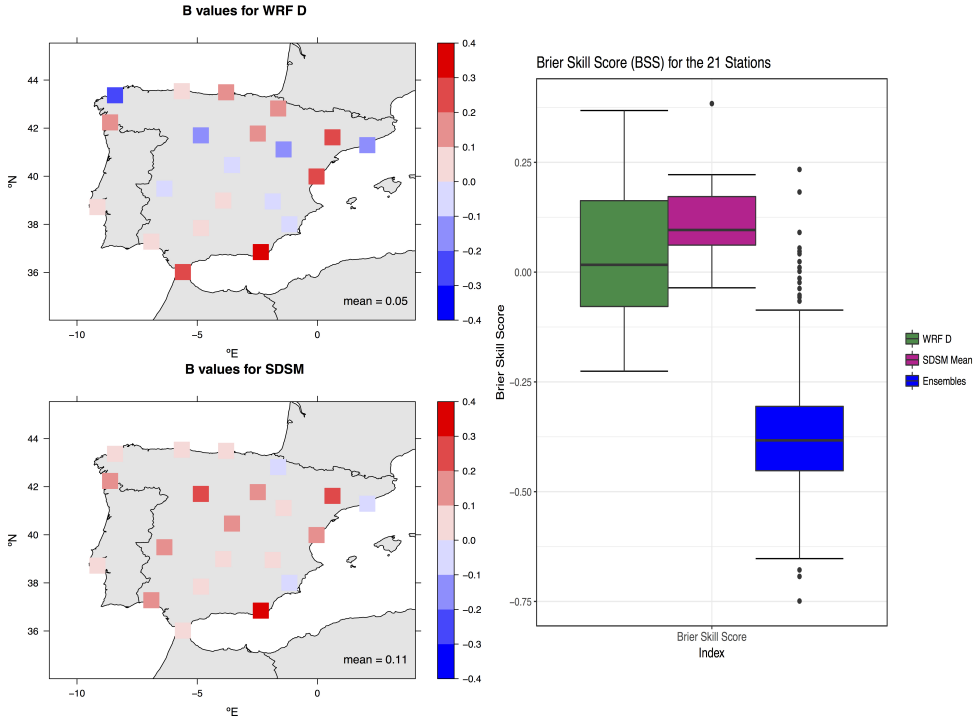


Figure 4.16: Left: The spatial distribution of the BSS for the D experiment (top) and SDSM mean (bottom) experiments. Their corresponding areal mean BSS is displayed in the bottom right corner of the maps. Right: BSS of the twenty-one stations over the IP for the D experiment (green), SDSM mean (magenta) and the members of the ensemble (blue).

mean. According to the box and whisker, it is clear that the ensemble members do not present any added value by themselves. The areal mean value measured for D is 0.05 and 0.11 for SDSM mean, but for both experiments added value is not observed on every station over the IP. For the D experiment, no improvement in the prediction is observed in eight stations: one in the North (A Coruña), three in the Centre (Valladolid, Madrid and Daroca), two in the Mediterranean (Murcia and Barcelona) and three in the Southwest (Cáceres and Albacete). For the SDSM mean, three stations do not show any added value compared to ERAI: one of them in the Centre (Pamplona) and two in the Mediterranean region (Murcia and Barcelona). The best results for D are obtained near the Mediterranean coast (with the exception of Barcelona and Murcia), while for the SDSM mean are obtained in Almería, Lleida and Valladolid.

Additionally, some precipitation indices were calculated for each station. On the one hand, the amount of precipitation simulated by the downscaling experiments was tested by means of the mean precipitation (pav), precipitation intensity (pint) and precipitation 90th quantile (pq90). On the other hand, the occurrence of precipi-

tation was studied by maximum consecutive dry days (pxcdd), wet-day probability (pwet) and maximum five-day precipitation (px5d). The scores obtained by the D experiment, SDSM mean and ensemble members are shown in Figure 4.17.

Starting by the precipitation amount, it is clear that the SDSM mean and the members of the ensemble outperform the D experiment (the corresponding medians are 1.55, 1.48 and 1.24 mm respectively) compared to the stations (1.53 mm). The spread of both SDSM products is really similar to that for the stations. The mean precipitation is underestimated by the D experiment.

The precipitation intensity is quite well simulated by the ensemble members. In that case, the median of the spread is 8.03 mm and 7.92 mm for the stations. The D experiment underestimates it (6.43 mm), but not as much as the SDSM ensemble mean (5.03 mm).

The 90th quantile of precipitation is underestimated particularly by the ensemble mean. The median of its spread is 10.46 mm, and 18.04 mm for the stations. However, the spread of the SDSM ensemble members is similar to that for the observed precipitation (17.64 mm). The D experiment, even if it is closer to the observations than the SDSM mean, underestimates also the 90th quantile of precipitation (14.63 mm).

Changing to occurrence indices, the median of the values of maximum consecutive dry days measured at the stations is 9 days. This number is overestimated by the SDSM mean (11 days), but underestimated by both D and the members of the

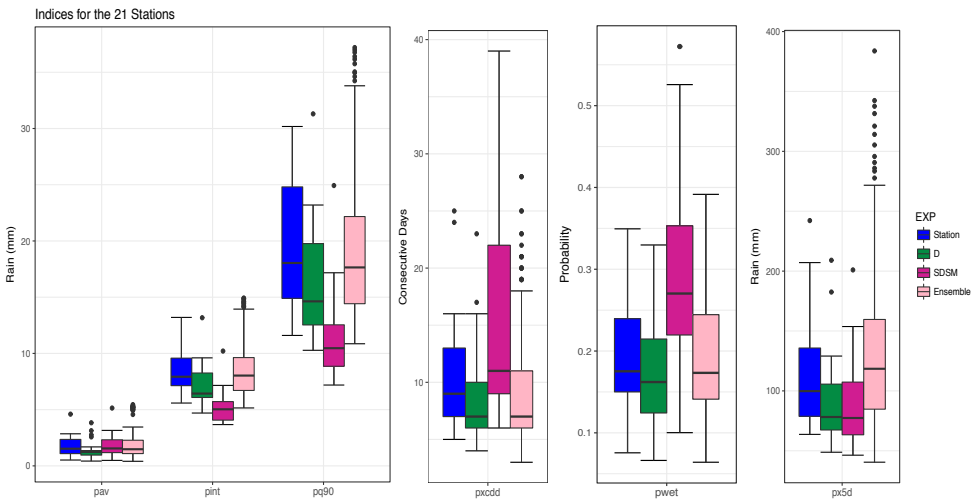


Figure 4.17: Precipitation diagnostics (pav, pint, pq90, pxcdd, pwet and px5d) produced by the observed data, WRF D, SDSM mean and each member of the SDSM ensemble (in blue, green, magenta and light pink respectively). The results of the twenty-one stations over the IP are included on each box and whisker.

ensemble (7 days in both cases). Additionally, the spread of the SDSM mean implies that this experiment tends to overestimate the maximum dry days in several stations.

A similar behaviour to that for maximum consecutive dry days is observed for the wet-day probability. In this case, the probability is highly overestimated by the ensemble mean (0.27) compared to that for the stations (0.18). Conversely, it is slightly underestimated by the D experiment and the members of the ensemble (0.16 and 0.17 respectively).

The maximum five-day precipitation, compared to the median of the stations (99.8 mm), was overestimated this time by the members of the ensemble (118.46 mm) and underestimated by both D and SDSM mean (78.19 and 77.37 mm respectively).

According to this long analysis of both downscaling techniques (dynamical - WRF and statistical - SDSM), it is clear that there is no best downscaling technique and that it depends on the verification statistic that is studied. The discussion of these results will be carried out in chapter 7, particularly the differences that appear between the SDSM ensemble mean and each member of the ensemble. Moreover, it will also focus on some aspects of the protocol followed to calibrate the SDSM, particularly the use of precipitation as a predictor.

5 Applications

BESIDES the main uses of the integrations performed with the WRF model that have been presented so far for the analysis of the Iberian atmospheric moisture budget or precipitation downscaling, both WRF simulations can be applied in many more studies as the chosen domain is represented by $15 \times 15 \text{ km}^2$ spatial resolution and the outputs have been stored every three hours. The validation and study of the atmospheric branch of the water balance was presented in chapter 3, but further research can be carried out focusing on the variability of the transboundary moisture fluxes or the breezes. The applications are not restricted to land, and they can be extended to regions over water such as the Bay of Biscay or west Mediterranean. For example, the surface wind data from the simulations can be used to reconstruct missing data from radial surface current datasets or to estimate the offshore wind energy potential at floating wind farms where previous in-situ wind measurements do not exist.

This chapter focuses on the validation of model outputs over water and on offshore wind energy potential results for two regions in the west Mediterranean where wind farms could be created in the future. These results were obtained in collaboration with the members of our group as a direct application of the numerical model runs produced for this thesis, and they are published on [Ulazia et al. \(2017\)](#). In this case,

I provided both WRF simulations and I took part in the validation of the data over water, but not in the calculation of the offshore wind energy potential estimation.

5.1 Validation of wind at 10 m over water

An accurate estimation of wind at 10 m is needed in order to properly calculate the offshore wind energy potential. To do so, the wind at 10 m obtained by both WRF simulations was validated against the observations of six buoys in the region and against the CCMPv2 dataset, at 0.25 degrees resolution.

The chosen buoys are located in the area delimited by the Cabo Begur in the north and the Cabo de Palos in the south (see section 2.1). However, the anemometer of these buoys is located at 3 m and not at 10 m as the wind simulated by WRF. In order to fairly compare the data from different sources, the wind speed at 10 m for each buoy was calculated by means of the logarithmic law of vertical wind shear¹ after calculating the instantaneous roughness of the sea with Hsu's equation (*Hsu, 2003*). The nearest points in both WRF simulations, ERAI and CCMPv2 were compared to buoy data by means of Taylor diagrams. The significance of the results was also addressed applying the bootstrap technique (with resampling), showed in the Taylor diagrams by shaded regions as explained in section 2.5.

The Taylor diagrams obtained for each buoy can be found in Figure 5.1. According to the results, the correlation coefficient changes locally. For the D experiment, the correlations are observed around 0.8 in Cabo Begur, Mahon and Cabo de Palos, near 0.7 in Tarragona and Dragonera, and 0.6 in Valencia. These correlations are similar to those obtained by ERAI in Tarragona, Valencia and Cabo Begur. Also the RMSE is similar for both experiments in those buoys. The N experiment scores higher RMSE and a lower correlation than ERAI and D. No major differences between ERAI, D and CCMPv2 are found in the results, indicating that D and ERAI are close to the observational error measured between in-situ and gridded (assimilated) observational datasets.

The comparison with buoys does not allow us to evaluate how well both WRF simulations capture the spatial variability of wind. Thus, N and D experiments and ERAI were evaluated versus CCMPv2. However, it must be taken into account that this dataset was created by the combination of wind speed measured by radiometers, scatterometers and moored buoys with ERAI wind fields. This means that the CCMPv2 dataset will be biased towards ERAI.

The correlation, RMSE and SD ratio maps for N and D experiments and ERAI against CCMPv2 are presented in Figure 5.2. Starting by the correlation maps, it is clear that the N experiment obtains the worst results. The D experiment improves

¹This methodology is explained in the Appendix C.1.

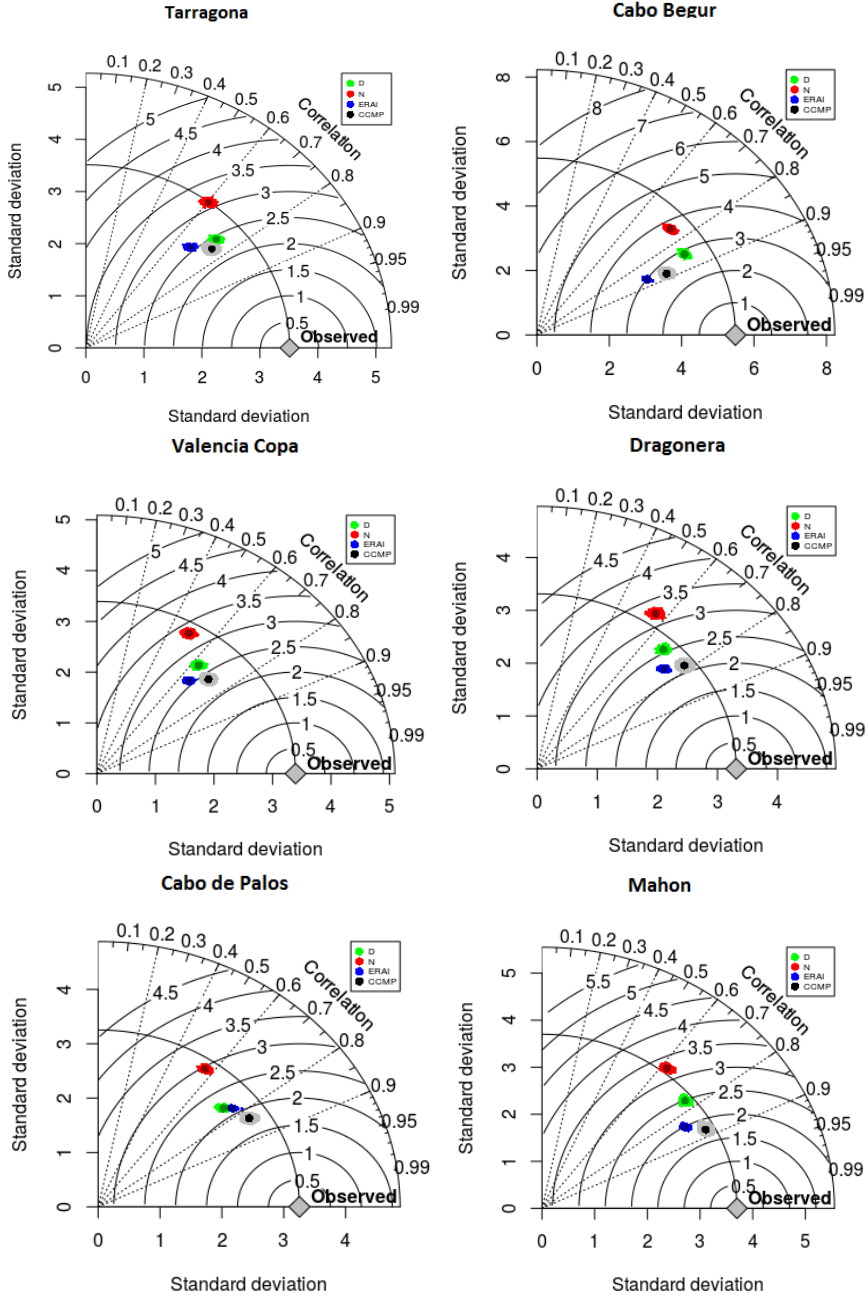


Figure 5.1: Taylor diagrams showing the standard deviation, r and RMSE results for the D and N experiments, ERAI and CCMPv2 dataset compared to buoy data (coloured in green, red, blue and black respectively). The shaded regions delimit the results obtained by the bootstrap technique, while the big dots correspond to the results obtained from the full sample of buoy data.

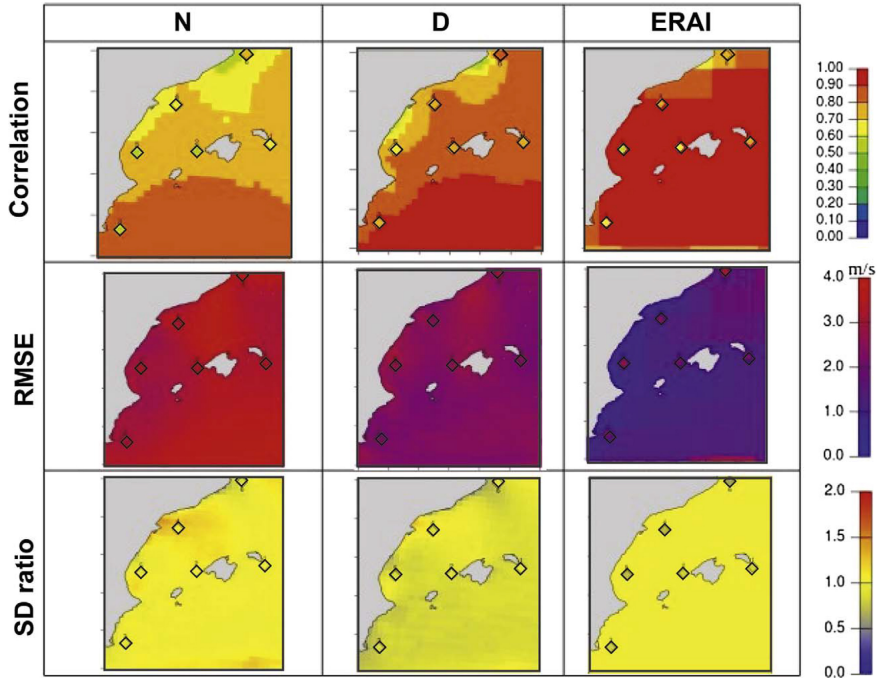


Figure 5.2: Correlation, RMSE and SD ratio maps for both WRF experiments and ERAI compared to CCMPv2. The results obtained for each buoy are presented by coloured diamonds.

the correlation obtained by the N experiment, but the values are not as good as those obtained by ERAI. However, even if ERAI obtains the best scores compared to the gridded dataset, the same is not observed while comparing to observed buoy data. Remarkable differences are observed in those locations for ERAI. The D experiment obtains a much closer agreement with the data measured by buoys.

Changing to the RMSE maps, the smallest values are reached by ERAI, while the largest values are observed for the N experiment. Again, the D experiment improves the results obtained by N. No spatial patterns are observed in those maps, but the areal mean for D is around 2.5 m/s and 1.5 m/s for ERAI. In this case, the differences between the results for the gridded datasets and buoys are remarkable for ERAI.

The SD map for the N experiment shows an overestimated region near the Ebro delta and in the north of the Balearic islands. The map for D improves the results for that region, but shows an underestimation of the variability in the rest of the domain. A really good agreement between ERAI and CCMPv2 is observed in the corresponding SD map. However, the discrepancies between ERAI and buoy data are again remarkable.

Then, all of the statistical indicators calculated support the idea that the CCMPv2

is biased towards ERAI and that the D experiment produces more reliable data thorough the whole domain. Additionally, this WRF experiment includes a higher spatial resolution. This is a valuable characteristic for the estimation of offshore wind energy potential over coastal areas where substantial spatial gradients can exist.

5.2 Measurements of offshore wind energy potential

Two potential wind farm sites were selected, taking into account some legal criteria as the minimum distance from coastline and the bathymetry of the domain, as it is not possible to anchor wind turbines when the sea bed is deeper than 1000 m. The two areas delimited by these criteria are presented in Figure 5.3. The bigger one is located in the Cabo Begur and it spans an area of 2318 km². The other one is located to the north of Menorca and its area is of about 576 km².

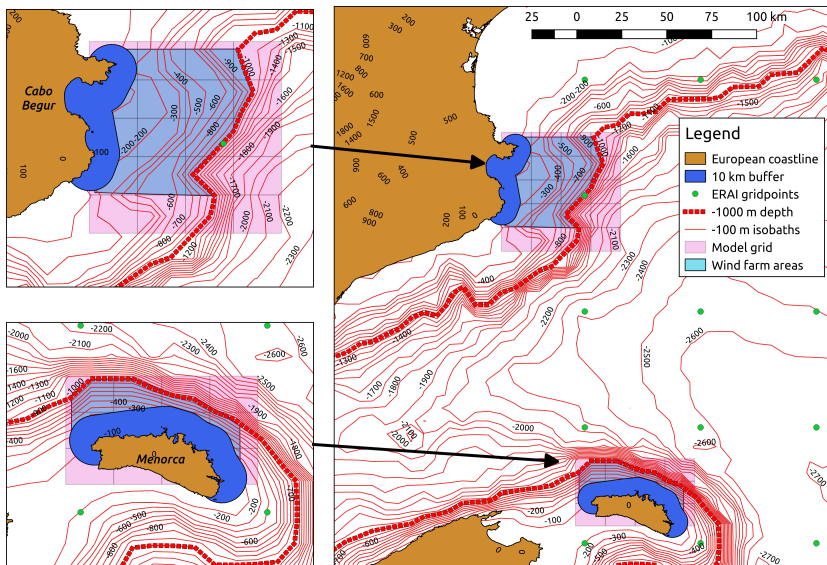


Figure 5.3: Detailed map of the studied region showing the potential wind farm zones. The land is coloured in orange, and the protected coastal area is coloured in blue. The isobaths taken from the ETOPO1 model ([Amante and Eakins, 2009](#)) are plotted by red lines, and that corresponding to -1000 m is marked by a bold dotted red line. The ERAI grid is marked by big green points, while that for both WRF experiments is represented by pink squares. Finally, the regions suitable for the construction of wind farms are delimited by light blue squares.

Three different types of turbines were chosen for this study: (1) MWT-92/2.4: a low turbine created by Mitsubishi Heavy Industry with the hub at 70 m and a diameter of 92 m. (2) Siemens-90/2.3: A medium high turbine with the hub at 130 m and a diameter of 90 m. (3) Siemens-160/6.0: A high turbine with the hub at 178 m.

Wind speed, and pressure and virtual temperature for the density of the air were interpolated from model original vertical levels (in η coordinates) to the three possible hub heights (92 m, 130 m and 178 m). These values are used to calculate the normalized wind speed. Then, the Capacity Factor (CF) is calculated from the average wind speed for the five-year period simulated with WRF (2010-2014), the rated power and the diameter of the turbine. Finally, the turbine’s Annual Energy Production (AEP) is calculated. The detailed methodology for the calculation of these variables is explained in the Appendix C.2.

In order to evaluate the wind energy potential at those regions, the corresponding wind roses must be known. As no measured data for those specific regions was obtained, the wind roses of the nearest buoys to the potential wind farm regions were studied. Those corresponding to Cabo Begur and Mahon buoys are presented in Figure 5.4. It is clear that the prevailing wind direction changes from one buoy to another. However, strong northern winds are more important than those from the east or west.

The seasonal and annual CF maps for the MWT-92/2.4 turbine are presented in Figure 5.5. The hub of this turbine is at 70 m, so the variables needed for the calculation of the CF are interpolated from the corresponding η levels from WRF. Focusing on the annual CF map, it is clear that the D experiment obtains similar values to that for ERAI, but with a relevant improvement in resolution. Compared to the N experiment, the results obtained by D are lower. However, the same pattern is observed in the three experiments, with higher values towards the open sea.

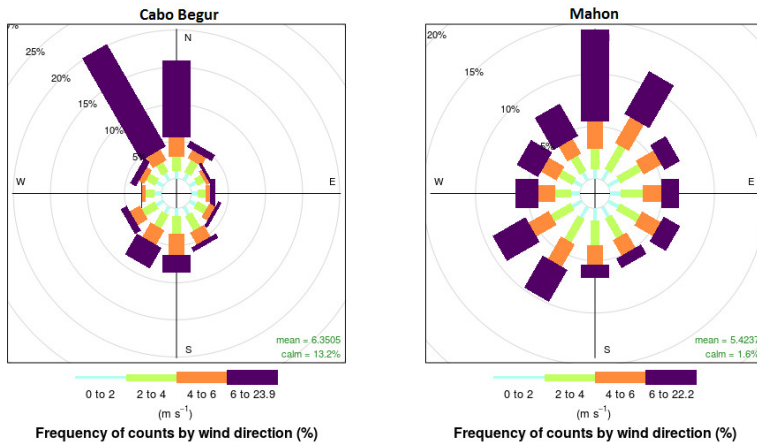


Figure 5.4: Wind roses for the Cabo Begur and Mahon buoys.

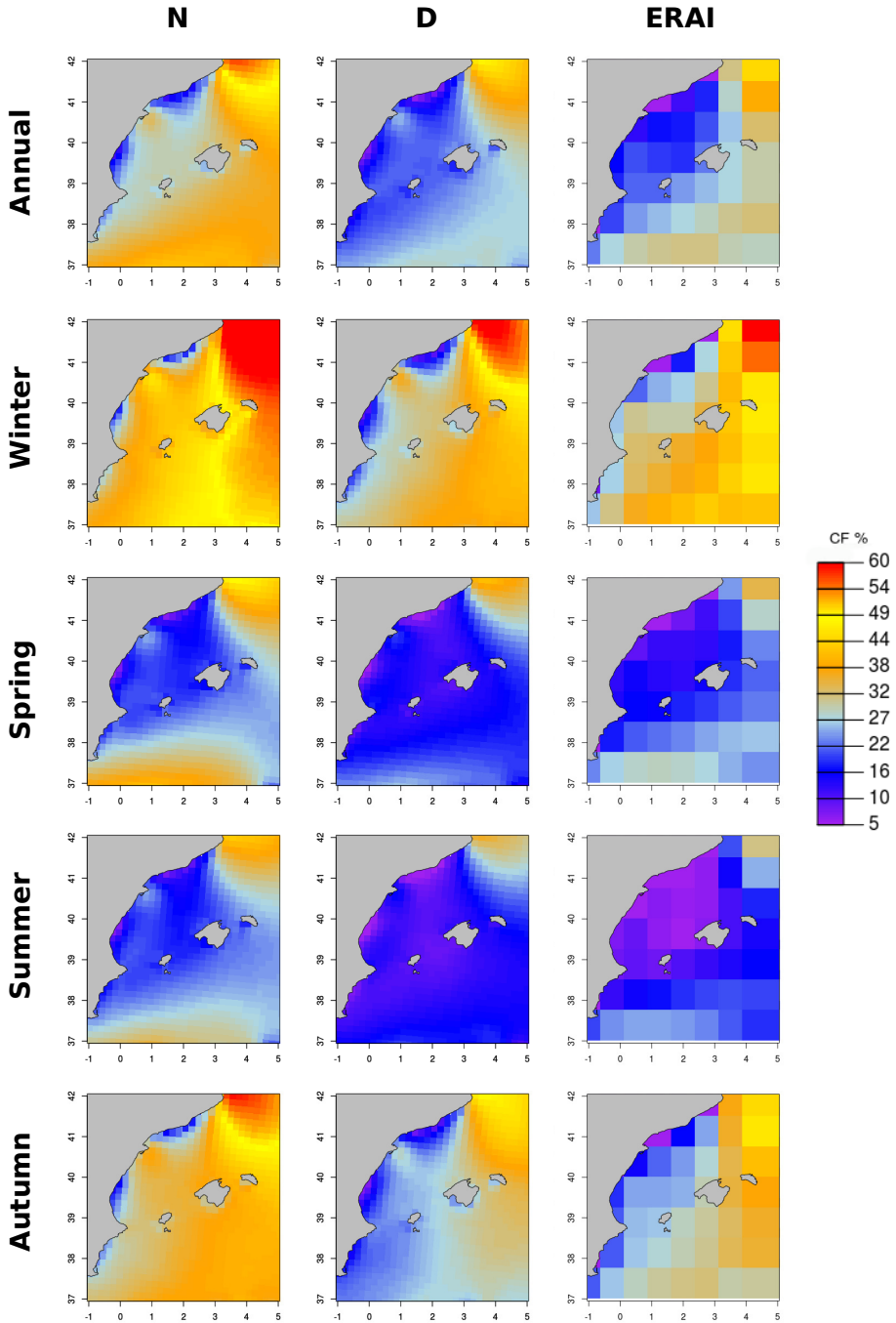


Figure 5.5: Seasonal and annual spatial distribution of the CF for the MWT-92/2.4 turbine (with the hub at 70 m).

5.2 Measurements of offshore wind energy potential

Table 5.1: Summary table for the AEP (in TW h) at the largest wind farm near Cabo Begur.

Bathymetry (m)	N. turbines	at 70 m	at 130 m	at 180 m
0-200	1190	9.71	10.96	11.45
200-400	1790	14.31	16.17	16.88
400-600	1980	16.12	18.21	19.02
600-800	920	7.53	8.5	8.88
800-1000	960	8.11	9.16	9.56
Total	6840	55.78	63.03	65.82

The differences between seasons are remarkable. Winter is the most intense season, followed by autumn, spring and summer. The high values observed during winter near the Cabo Begur are related to the northern Tramontana winds, typical in this region.

Focusing only in the most reliable experiment (the D experiment), the annual CFs obtained in the potential wind farm regions are above 30%. Particularly, the annual CF is around 49% in the largest potential wind farm (near Cabo Begur), varying from 60% during winter and 38% in summer. The annual CF for the second potential wind farm in the north of Menorca is around 32%, reaching 44% in winter but only 16% during summer.

The AEP on both potential wind farms depends on the type of turbine chosen and its corresponding hub height. Starting by the largest region near Cabo Begur (Table 5.1), 6840 turbines could be built, producing 55.78 TW h for a hub at 70 m (MWT-92/2.4 turbine) according to the results obtained by the D experiment. Using taller turbines the results would reach the 63.03 TW h for Siemens-90/2.3 (at 130 m) and 65.82 TW h for Siemens-160/6.0 (at 180 m).

According to the results obtained by the D experiment, 1700 turbines could be built in the second wind farm at the north of Menorca (Table 5.2), producing 8.79 TW h using the turbines with the hub at 70 m (MWT-92/2.4). The AEP would reach the value of 9.93 TW h using the turbines with the hub at 130 m (Siemens-90/2.3) and 10.36 TW h for those with the hub at 180 m (Siemens-160/6.0).

Table 5.2: Same as Table 5.1 but for the smallest wind farm at the north of Menorca.

Bathymetry (m)	N. turbines	at 70 m	at 130 m	at 180 m
0-200	0	0.0	0.0	0.0
200-400	140	0.72	0.81	0.85
400-600	510	2.68	3.02	3.16
600-800	550	2.85	3.22	3.35
800-1000	500	2.54	2.85	2.99
Total	1700	8.79	9.93	10.36

6 aiRthermo

NOWADAYS many research communities are increasingly adopting the R software as a tool for scientific research and data analysis, including environmental sciences (*Thyer et al., 2011*) and modelling (*Wu et al., 2014; Humphrey et al., 2017*). After all the diagnostics and statistics calculated by means of R during this thesis, and making use of old version of programming codes for the calculation of atmospheric thermodynamic variables, we realized that there was room for an R package dedicated to the analysis of atmospheric soundings and the stability of the atmosphere between the community of atmospheric scientists using R. This led to the development of the package *aiRthermo*, publicly available on <https://CRAN.R-project.org/package=aiRthermo> since August 2017.

The analysis of the stability of an air parcel or a whole atmospheric column involves the computation of many variables that affect the density of the atmosphere at different pressure levels and the analysis of the heating rates of air parcels as they ascend from one level to another following dry-adiabatic or pseudo-adiabatic evolutions, depending on the saturation of the air parcel. Some R packages as *RadioSonde*, *humidity* and *meteogRam* are dedicated to the calculation of some of these atmospheric variables. However, *aiRthermo* extends the functionality offered by them, incorporating additional functions for the calculation of moisture indices, condensation processes, vertical evolutions of air parcels or even the production of Stüve diagrams.

Additionally, not only in-situ observations (soundings) can be computed accurately by the package, but also model data.

Hopefully, *aiRthermo* will have an impact in many practical applications of environmental forecasting at different scales such as statistical downscaling for climate analysis or forecast, and the diagnosis of flash floods or storms (*de Coning et al., 2011; Chaudhuri et al., 2013; Vujović et al., 2015; Czernecki et al., 2015*). The analysis of the climatological distribution of atmospheric instability (*Siedlecki, 2009*), its interannual variability and even its expected future distribution under global change conditions (*Viceto et al., 2017*) is another field that can benefit from this package.

Most of the theory and methods used in these functions can be found in the basic atmospheric thermodynamic literature (*Rogers and Yau, 1989; Emanuel, 1994; Djuric, 1994; Bohren and Albrecht, 1998; Tsonis, 2002; Wallace and Hobbs, 2006; Petty, 2008; North and Erukhimova, 2009*). However, some key points will be explained in section 6.1 as some of the methods are not documented the same way or covered in detail in these references. Finally, a brief explanation of the most important routines contained in the package will be presented in section 6.2. The functions will be divided into groups according to their purpose.

6.1 Key points of the methodology

In every case, the state of an air parcel is defined by means of its pressure P , temperature T and mixing ratio w . As every variable defined in the package, their units must be expressed in the standard units from the International System. In this case, they are expressed in Pascals (Pa), degrees Kelvin (K) and kg/kg respectively.

The calculation of saturation pressure of water varies according to the temperature of the surface below the air parcel. For ice and water below 30° the definitions in pages 197-200 from *Bohren and Albrecht (1998)* are used, while for water above 30°C Buck's equation (*Buck, 1981*) is followed. The dew-point temperature is calculated from given pressure and mixing ratio following the equation 5.68 in *Bohren and Albrecht (1998)*.

Moist specific heats are computed following *Tsonis (2002)*. The moist specific heat at constant pressure is defined as

$$c_{pm} = c_{pd}(1 + 0.87q) \quad \text{with} \quad c_{pd} = 1005 \text{ JK}^{-1} \quad (6.1)$$

At constant volume, the moist specific heat is defined as

$$c_{vm} = c_{vd}(1 + 0.97q) \quad \text{with} \quad c_{vd} = 718 \text{ JK}^{-1} \quad (6.2)$$

The values of c_{pd} and c_{vd} are taken from *Bohren and Albrecht (1998)* and *Petty (2008)*. While using the package, the values corresponding to the specific heats for dry air can be also obtained by specifying a mixing ratio of 0 kg/kg.

An approximate expression for the calculation of the latent heat of evaporation of water is used within *aiRthermo* as no reliable analytic definition exists. Two empirical methods were defined within the package, and the use of one or the other depends on the temperature of the water. The first method, typically defined for liquid water (between 233.15 and 313.15 K), is a cubic polynomial expansion based on tabulated values from *Rogers and Yau (1989)* that yields an absolute residual smaller than 1 J/kg with all the terms statistically significant to a 99% confidence level. In this case, it is considered that super-cooled water can coexist with ice up to the Schaefer point (about -40°C). The second method is used typically when temperatures range between 210 and 273.15 K and it is a quadratic fit to the values measured for ice from *Feistel and Wagner (2006)*, characterized by residuals smaller than 0.05 J/kg. As the values are not the same in the overlapping gap between both methods, a linear combination of ice's (L_i) and water's (L_w) latent heats is computed in that range of temperatures ($T \in [253.15, 273.15]$) by means of

$$L = w_i L_i + (1 - w_i) L_w \quad \text{with weight} \quad w_i = 1 - \frac{T - 253.15}{20} \quad (6.3)$$

Below 253.15 K, the latent heat corresponding to ice is applied, while that corresponding to water is used above 273.15 K.

As the vertical evolutions are considered in the pressure vertical coordinate and they are computed assuming hydrostatic balance, the dry adiabatic and pseudo-adiabatic vertical derivatives with z (Γ_d and Γ_s) are not used in *aiRthermo*. In our case, the vertical evolutions in pressure levels are calculated as $\Gamma_d^* = \left(\frac{dT}{dP}\right)_d = \frac{\Gamma_d}{\rho g}$ and $\Gamma_s^* = \frac{\Gamma_s}{\rho g}$, transformed for the expressions in z vertical coordinates from the literature assuming hydrostatic equilibrium. Thus, the vertical evolution of an air parcel defined by the initial values of P_0 , T_0 and w_0 is computed by numerically solving the ordinary differential equation given by

$$\frac{dT}{dP} = \Gamma_i^*(P, T, w) \quad (6.4)$$

with i depending whether the particle is saturated or not ($i = d$ or $i = s$ respectively). The equation is solved by means of a Runge-Kutta scheme of fourth order and the mixing ratio changes according to whether the parcel achieves saturation against its environment or not. Additionally, it is assumed that the parcel is kept at $w = w_s$ after arriving at the Lifting Condensation Level (LCL). For the vertical ascents, Γ_d is assumed whilst the parcel remains below the LCL.

If the initial state of the air parcel (P_0 , T_0 and w_0) is not provided to the functions that calculate the instability indices, a vertical average of the lower pressure levels provided is necessary. However, this is a key step on the calculation of the indices as the results are very sensitive to the initial values of pressure and moisture (*Craven et al., 2002; Letkewicz and Parker, 2010*). Within the package, the vertical width of the parcels is defined as

$$\Delta Z = \frac{R_d}{g} \int_{P_t}^{P_s} \frac{T_v}{P} dP \quad (6.5)$$

Thus, the accumulated value of the quantity $X(P)$ in the vertical is given by the expression

$$\bar{X} = \frac{1}{\Delta Z} \frac{R_d}{g} \int_{P_t}^{P_s} \frac{X \cdot k \cdot T_v}{P} dP \quad (6.6)$$

where $k(P)$ plays the role of a normalizing function that is used to get the vertically accumulated values. This function is not always used and it varies depending on the variable that is going to be average. For example, for temperature it will be $k(P) = 1$, while for moisture the specific humidity $k(P) = q(P)$ will be used. The vertical integration is computed by aggregating the values of the discrete slabs defined in the data. A linear or logarithmic profile can be used. Additionally, in order to boost the performance of these computationally demanding functions, their core was programmed inside a C extension.

Finally, a routine for the production of Stüve diagrams was included in *aiRthermo*. It can plot the data from soundings or even the trajectory of the lifted air parcel computed with the function for the calculation of CAPE and CIN. The routine plots the equivalent potential temperature lines, constant mixing ratio lines and dry adiabatic lines, all of them calculated by *aiRthermo* in order to maintain the consistency between the results. The user can modify the axis of the Stüve diagrams without restriction and more than one line can be plotted at once.

6.2 Included functions

The package is made of 46 functions, but they can be separated into six big groups according to their utility. The functions are related to the density of the moist/dry air and their virtual temperature, to the conversion of moisture indices, to the saturation mixing ratios or pressures, to the state of the parcel after adiabatic processes, to instability indices or to plotting the Stüve diagram. A brief description of each set of functions is presented here, but for a full description of the functions and the parameters needed in order to run them, the manual of the package¹ must be checked.

- **Density of dry/moist air and virtual temperature**

Depending on the pressure, temperature and mixing ratio of an air parcel, alternative methods to calculate its density can be found in our R package. It can be calculated directly with the corresponding function (`densityMoist`), or by means of intermediate functions for the calculation of the density of dry air and the density of water vapour independently (`densityDry` and `densityH2Ov`).

¹The manual of the package can be found in the web-page corresponding to *aiRthermo* in the Comprehensive R Archive Network (CRAN): <https://cran.r-project.org/web/packages/aiRthermo/aiRthermo.pdf>

The virtual temperature of an air parcel can be also calculated directly making use of the function `virtual_temperature`. Additionally, some functions for the conversion between different variables are included. For example, any temperature can be converted from Celsius to Kelvin or vice versa with `C2K` and `K2C`, or from partial pressure of water vapour to mixing ratio with `e2w`.

- **Conversion of moisture indices**

Several functions that allow the conversion between moisture indices as dew point temperature, mixing ratio and specific or relative humidity are included in *aiRthermo*. Amongst others, the most important functions of this category are those converting from relative humidity to mixing ratio (`rh2w`), from relative humidity to specific humidity (`rh2shum`), from mixing ratio to dew point temperature (`w2Td`) and from mixing ratio to specific humidity or reverse (`w2q` and `q2w`).

- **Saturation mixing ratios or pressures**

In this class are included all the functions that use the Clausius-Clapeyron equation to calculate saturation mixing ratios or pressures. The most important functions are the `saturation_mixing_ratio` and `saturation_pressure_H2O`, computing the saturation mixing ratio w_s in kg/kg and the saturation pressure e_s in Pa respectively.

- **State and evolution of an air parcel**

The package is able to calculate the state of a parcel from given pressure, temperature and mixing ratio with the function `parcelState`. However, to calculate the evolution of an air parcel, *aiRthermo* determines which function is better depending on the state of the particle and the environment. A general ascent from a given initial pressure to the final one is computed by the function `adiabatic_ascent`. It selects the type of evolution that the air parcel is going to follow on each step, and if the mixing ratio must be conserved or set to w_s . A downwards evolution can be also computed with `AnyAdiabaticDown`, but it needs the amount of water available in the cloud for evaporation (in kg/kg) in order to work properly.

Conversions between potential temperature, temperature and pressure can be calculated making use of `PT2Theta`, `PTheta2T` and `TTheta2P`. These functions are useful if adiabatic processes are taking place.

- **Instability indices**

Several functions compute the most common instability indices of the literature, such as K index, the Total-Totals index, the Showalter index and the Lifted index (functions `Kindex`, `TTindex`, `Sindex` and `LIindex` respectively).

However, the most computationally demanding function is `CAPE_CIN`. It calculates the values of CAPE and CIN, but also the LCL, the Level of Free Convection (LFC), the End Level (EL) or even the trajectory followed by the

lifted parcel until reaching the top of the sounding. For the optimal performance of the function, some control attributes must be also provided. For example, the *PlowTop* attribute provides an initial average over the bottom layer of the sounding, *precoolType* determines if a precooling must be applied or not to the initial conditions of the air parcel and *upToTop* requests if the lifted particle should continue or no after the first time crossing the ambient sounding. Additionally, if the attribute *getLiftedBack* is set to *TRUE*, the evolution of the lifted particle until the top level of the sounding is returned as a set of vectors for P, T and *w*.

• **Stüve diagrams**

The `stuve_diagram` function is included in the package in order to create fully editable Stüve diagrams. They can optimally show the trajectory followed by

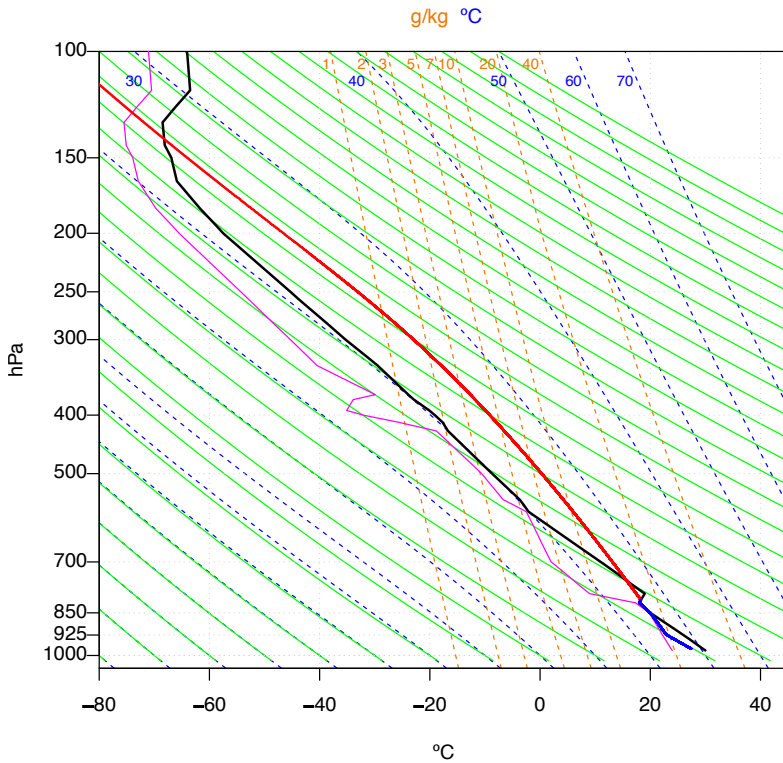


Figure 6.1: Example of a Stüve diagram plotted with *aiRthermo*. The temperatures and dew point temperatures measured by the sounding are plotted in black and magenta lines. Whilst the blue line represents the evolution of the lifted air parcel until the moment when it crosses for the first time the ambient sounding, the red line represents its evolution until the top of the sounding.

any ascending air parcel. Thus, this function is related to `CAPE_CIN`, as that function is the one that can provide the state of the parcel at each slab of the ascent.

Figure 6.1 shows a Stüve diagram created for the data measured in Davenport, USA (station ID 74455), where the balloon was released on 1997/06/21 at 00 UTC. This sounding illustrates a case with a strong convective instability, and it was taken from [Tsonis \(2002\)](#). The importance of a good calibration of the function `CAPE_CIN` is remarkable, as major differences in the estimation of CAPE for the sounding can appear if the `upToTop` attribute is set to `TRUE` or `FALSE` (red and blue lines of the sounding respectively).

7

Discussion

OUR objective was to study the effect of the 3DVAR data assimilation step on the simulation of the atmospheric branch of the water balance over the IP, and to compare the precipitation downscaled by different techniques: dynamically with WRF and statistically with SDSM. In this chapter, the methodologies and results presented in chapters 2, 3 and 4 are discussed and compared to previous studies.

The discussion will be divided in three different sections taking into account three key aspects of the study that has been carried out. Section 7.1 will focus on the configuration of both models (WRF and SDSM), section 7.2 on some issues with the validation datasets used, and finally, section 7.3 will provide further insight into the results.

7.1 Configuration of the models

We begin by discussing the configuration designed for the WRF model. Even if both simulations span the period 2009-2014, the first year (2009) was designed as spin-up

period for the model. As our intention is to analyse the atmospheric branch of the water cycle, the aim of using this year as a spin-up was to reduce the errors in the land-atmosphere fluxes and not to initialize every layer defined in the land surface model. Several years of spin-up are needed to achieve a full initialization of soil's deep layers (*Lim et al., 2012; Stacke and Hagemann, 2016*). According to *Giorgi and Bi (2000)*, the RMSD reaches the equilibrium after five to fifteen days of simulation. However, *Christensen (1999)* stated that few months would be enough to initialize correctly the soil variables. According to recent studies over the EUROCORDEX region (*Montávez et al., 2017*), six months would be the optimal length of the spin-up period for water-related studies. During the last years, different lengths of the spin-up used on this kind of studies can be found: one month (*Angevine et al., 2014*), four months (*Jerez et al., 2010, 2012, 2013*), seven months (*Argüeso et al., 2011*) or one year (*Zheng et al., 2017*). The results presented in this thesis are robust and do not vary if longer spin-up periods are defined. The spread of the residuals of both WRF simulations compared to those from ERAI do not vary when two, three, four or five years long spin-up periods are defined in our simulations.

The length of the simulations (five-years without the spin-up) is similar to those commonly used in the field when running the WRF model (*Jiménez and Dudhia, 2013; Ríos-Entenza and Miguez-Macho, 2014; Ríos-Entenza et al., 2014*). It is clear that these simulations cannot be used for the study of the climatology or the inter-annual variability of the most important terms of the water balance. However, the results were studied in order to find any possible relationship with low frequency variability sources as NAO or ENSO. The effect of the NAO is perceptible in the precipitation regimes over the IP (*Rodríguez-Puebla et al., 2001*), but the effect of the ENSO is not stationary (*López-Parages and Rodríguez-Fonseca, 2012*) and it is restricted to different regions of the IP (*Kiladis and Diaz, 1989; Rodó et al., 1997; Frías et al., 2010; Vicente-Serrano et al., 2011; Lorenzo et al., 2011*). The monthly residuals of the moisture equation from both simulations were classified into low or high values of NAO and ENSO (below the 25th percentile or above the 75th percentile), according to the indices downloaded from the Climate Prediction Center. The values of the residuals do not change from one phase to another.

Finally, this study highlighted WRF's inability to simulate a realistic evaporation in some points of the IP. In these points, the corresponding evaporation time-series were flat most of the time. Thus, the correlation between the simulated and measured evaporation was rather low (or even negative). In order to determine the cause of this problem, the static data included in the NOAH land surface model were studied, particularly the soil type and the land uses defined on each point. According to these data, the IP is mainly made of loam, while the Guadalquivir Basin is made of clay. As similar soil types were defined all over the IP, it is reasonable to think that the *built-up or urban* category in the land uses of the model is the reason why this is happening.

Changing to the configuration of the SDSM model, we begin by discussing an aspect that departs somehow from convention. In our study, the precipitation from reanalysis was also included in the initial predictor variables for the calibration of

the model. The reason why it was included is that the dynamical models simulate precipitation based on large-scale and convective processes (precipitation from fronts or cumulonimbus clouds for example), but they are not completely taken into account by other grid-scale predictors. Then, precipitation from reanalyses provides important information for the statistical models, adding some explanatory power. This is not the first time that it has been done in the literature. *Schmidli et al.* (2006) showed that precipitation can be helpful in statistical downscaling, and *Wilks* (1992) conditioned the selection of the parameters of a stochastic daily weather generator based on the monthly precipitation from coarse resolution models. Others as *Fealy and Sweeney* (2007) based the selection of predictors of a statistical technique for the prediction of rain on the correlation between those predictors with precipitation.

The number of predictors included in the calibration of the SDSM is also important. According to previous studies (*Wilby and Wigley, 2000; Hanssen-Bauer et al., 2005*), a model should not include less than three or more than six predictors. The statistical model can suffer from over-fitting if more predictors are included (*Huth, 2005*). In our case, the SDSM was calibrated including six predictors in most of the stations of the IP.

It was also found that the stations must be calibrated individually and that no predictor suites based on the latitude, longitude, elevation or annual precipitation can be defined for the stations of the IP. Similar results were obtained in a study focusing on Northern Ireland (*Crawford et al., 2007*), where the predictor suite varied even seasonally.

7.2 Issues with the validation datasets

Some problems arise from the use of several datasets for validation. The main one is that the lack of high resolution datasets complicates the interpretation of the results, particularly if the datasets are not available for the same period and domain used in our both WRF simulations.

Our results showed that the validation of our results against datasets with coarser resolution can generate misleading interpretations at first. Particularly, this is what happens with the precipitation validation datasets as EOBS. Figures 3.5 and 3.6 showed that major differences between EOBS and both WRF simulations appeared in the mountains located in the northwestern corner of the IP. However, focusing on the accumulated annual precipitation in Figure 3.30, it is clear that the spatial pattern for the D experiment presents much more similarities with that generated by the observed precipitation than that from EOBS. Thus, the geographical distribution of the field produced by WRF is similar to those produced by high resolution datasets but for a different period. These similarities in the spatial pattern are not only observed for the atlas created by the Spanish Meteorological Agency (*AEMET, 2011*), but also

for the accumulated precipitation from *Belo-Pereira et al. (2011)* (Figure 6 of their paper). The Iberian dataset with a resolution of 0.2° (*Belo-Pereira et al., 2011*), created by merging the Spain02 (*Herrera et al., 2012, 2016*) and the PT02 datasets (for Portugal), would be the most similar dataset to our simulations available in the literature. However, again, its period does not cover ours, so a direct comparison is impossible (if it is not qualitative). This means that the interpretation of the verification results would be optimal only if finer resolution and real datasets existed. Previous studies such as *Rummukainen (2010)* and *Gómez-Navarro et al. (2012)* have also identified this problem.

During this thesis, comparisons between point and gridded measurements have been carried out. This could be a problem as the representativeness error is introduced in the validation results. It is a non-zero scale-dependant error, independent of the model performance (*Tustison et al., 2001*). However, in order to compare two different datasets, the nearest neighbour or the bilinear interpolation techniques are commonly followed in the literature. On the one hand, the nearest neighbour technique does not smooth the fields when downscaling to higher resolution grids (*Accadia et al., 2003*), so it is suitable when comparing non-linear fields as precipitation (*Casati et al., 2008; Moseley, 2011*). On the other hand, the bilinear interpolation reduces the maxima and increases the minima of the field (particularly when it is applied to precipitation) (*Accadia et al., 2003*), so it is favoured only when the values do not vary too much on scales larger than the spatial resolution (*Moseley, 2011*). Taking this information into account, the use of the nearest neighbour technique was found suitable for our validations. As previously stated, several previous studies have followed the same methodology (*Borge et al., 2008; Jiménez et al., 2010; Jiménez and Dudhia, 2012; Ömol, 2012; Soares et al., 2012*).

Finally, poor correlation values were observed for precipitation near the Mediterranean region (see Figure 3.5). This feature is related to the sources of precipitation affecting the IP and how they are represented in the validation datasets. The observed precipitation over the Atlantic facade is mainly produced by frontal systems associated to cyclones in the northern Atlantic ocean. In contrast, the Mediterranean coast and the Ebro valley is characterized mainly by very scarce annual precipitation concentrated in severe small-scale (subgrid) convective events. It is known that the observational datasets are not always able to detect these high-precipitation events (*Herrera et al., 2012*), and the spatial pattern of this precipitation type has been widely studied in the literature (*Rodríguez-Puebla et al., 1998; Esteban-Parra et al., 1998; Fernández et al., 2003; Muñoz-Díaz and Rodrigo, 2004; García-Valdecasas Ojeda et al., 2017*). Therefore, that the performance of the models over the IP is better in the Atlantic region than near the Mediterranean Sea is frequently found in the literature (*Domínguez et al., 2013; Jiménez-Guerrero et al., 2013*).

Poor correlation values for evaporation were also obtained by both WRF simulations and ERAI in the Mediterranean region (see Figure 3.20). According to the literature, this would be the first time that the GLEAM datasets have been validated over the IP, and taking into account the limited availability of evaporation measure-

ments, why really small correlation values are concentrated in this region is an open question for the future.

7.3 Further insight on the results

This section focuses on providing further insight on the results obtained in this thesis. We will start by studying the results presented in section 3.4 for the residual of the water balance in both WRF simulations. The spread of the results showed that the N experiment (without data assimilation) produced a positive residual, while the D experiment (with data assimilation) and ERAI produced a negative residual. This change in the sign of the residual appears as a result of the data assimilation step in the D run. The data assimilation produces accurate initial fields in order to reproduce better the state of the atmosphere measured by observations by correcting any existing bias in the model. This is a key point for the moisture conservation equation as the moisture cannot be preserved since the analysis increments of the data assimilation are not physical terms of the equations that simulate the behaviour of the atmosphere. In our study, the D experiment is able to produce closer results to the observations despite the lack of complete balance as a result of the data assimilation step. Additionally, the D experiment improves the representation of the atmospheric branch of the hydrological cycle made by the N experiment as shown by sections 3.1, 3.2 and 3.3. It is able to obtain similar or better results than the forcing reanalysis ERAI. Thus, the data assimilation improves the quality of the variables simulated, as also found by previous studies (*Navascués et al., 2013; Ulazia et al., 2016, 2017*).

The robustness of the results presented for the residuals was further tested by means of a bootstrap analysis. Even if these results are not presented in section 3.4, 1000 time series with resampling were created from the full sample of the residuals from both WRF experiments and ERAI. The medians of these new residuals showed that the seasonal cycle is more intense than the interannual variability over the IP. The Median Absolute Deviation (MAD) between them and the full sample is really small for both WRF simulations compared to ERAI's, and the spread of the values do not overlap each other. As stated in *Ulazia et al. (2016)*, similar results are obtained for wind over the ocean for period 1990-2001 when comparing different configurations of WRF with 3DVAR data assimilation every six and twelve hours or without data assimilation.

The impact of the data assimilation is also remarkable at the seasonal analysis of the areal mean of the residuals (see Figure 3.25), where the most remarkable values appeared during the afternoon (around 18 UTC). This suggests that the assimilation of temperature and/or moisture observations has an effect particularly in the planetary boundary layer (PBL).

The breezes in the coasts of the IP seem to be a triggering factor for the water balance over the IP especially during summer. According to Figure 3.26, important changes in the analysis increments take place during the afternoon for the specific humidity at 2 m, particularly near the Ebro and Guadalquivir basins. These changes are related mainly to the coastal breezes near the Mediterranean Sea. These results are similar to those obtained by *Cardoso et al. (2013)*, as they found that the moisture enters the IP through the basins of the rivers. Additionally, *Ortiz de Galisteo et al. (2011)* stated that the breezes are also relevant for the annual and seasonal diurnal cycles of PW based onto observed GPS data.

In addition, remarkable high values of PW near the Mediterranean and Cantabrian coasts during summer (Figure 3.31) were triggered by the breezes of these regions. A similar effect was reported by *Zveryaev et al. (2008)*, as they found that local convectiveness and summer heatings can produce positive PW anomalies even if the moisture transports are reduced. The spatial pattern of the mean daily values of PW resemble the findings by *Zveryaev et al. (2008)*, where remarkable values of PW are observed near the coasts in winter, but even larger near the Mediterranean during summer.

Changing the topic to the comparison of both downscaling techniques (carried out in chapter 4), our experiments showed that their results systematically range between the results obtained by the observational datasets (EOBS, TRMM and GPCP). Not only on a site-by-site basis, but also on the defined four regions over the IP. This implies that both downscaling experiments (dynamical and statistical) produce similar results to their counterparts computed from different observational datasets, even if the correlation or RMSE scored by our experiments are not perfect. Thus, the error in the estimation of precipitation by different downscaling models is similar to the estimations of precipitation that are derived from the commonly used observational datasets. Additionally, these differences cannot simply be attributed to the representativeness error, as more reasons can affect these discrepancies between observational datasets, such as how the dataset is created or what kind of observations is made of. In this case, GPCP and TRMM are created by merging estimations of precipitation made by satellite and rain-gauge data, while EOBS does not include satellite-measured data.

Some remarkable features arise from the comparison of the SDSM mean and each member of the ensemble. The Taylor diagrams calculated for each station (see Appendix B) showed that the correlation and RMSE is improved by the ensemble mean, while the SD is deteriorated. Thus, the SD is better simulated by the ensemble members. Changing to the precipitation amount indices, the mean precipitation does not change from the SDSM mean to the ensemble members, but there is an important decrease in precipitation intensity and 90th percentile for the ensemble mean. Focusing on the precipitation occurrence indices, the maximum consecutive dry-days and the wet-day probability is overestimated by the ensemble mean, while the maximum five-total precipitation is overestimated by the members of the ensemble. Then, it is clear that in order to decide which downscaling method is better, these differences in the performance must be taken into account. However, the SDSM is able to produce

comparable (or even better) results to WRF, something that agrees with previous studies. Over flat terrain, similar results were obtained by both downscaling techniques (*Schmidli et al., 2007*). A comparison of a statistical model with WRF in the mountain regions of Colorado (*Gutmann et al., 2012*) showed that the statistical downscaling improved the results of the original model, but showing differences in the spatial pattern. Over the continental Spain, a comparison of eight RCMs with five statistical downscaling methods was carried out as part of the EURO-CORDEX project (*Casanueva et al., 2016*). The statistical methods outperformed the RCMs in terms of seasonal mean precipitation.

However, even if these results have been found for the comparison of both downscaling techniques, it must be considered that this is true for seasonal-forecast or climate-change like downscaling exercises where data assimilation cannot be considered because of the lack of observations, and only simulations as the N experiment can be carried out. Additionally, in these comparisons with different statistical downscaling techniques, the correlation coefficient is not a proper verification index as these methods will always outperform the numerical downscaling because of the methodologies they followed. The temporal occurrence of precipitation must also be checked in order to create a fair comparison between the dynamical and statistical experiments for applications not oriented to climate change such as operational weather or quantitative precipitation forecasts.

Finally, it must be noticed that the high-resolution inputs created from reanalysis data and the use of the precipitation as a predictor means that the statistical downscaling model (in our case, SDSM) is getting closer to the configuration of the dynamical downscaling models. Then, and as stated in some other studies (*Díez et al., 2005; Fernández-Ferrero et al., 2009*), maybe we should start using both techniques in combination and not in opposition. The dynamical modelling can provide the spatial coverage and occurrence, while the statistical downscaling can improve the local precipitation amount.

8 Conclusions

THIS thesis focuses on how the atmospheric balance over the IP is simulated by different configurations of the WRF model (with and without data assimilation), but also explores the possibilities of the dynamical and statistical downscaling applied to the precipitation.

In the first part of this thesis, the differences in the water balance simulated by two WRF simulations were studied. The main configuration of both simulations was the same. However, one of them included an additional 3DVAR data assimilation step (the D experiment), while the other did not (the N experiment). A spatial resolution of 15 km x 15 km was used in both simulations, an appropriate resolution for an atmospheric water balance study like ours. The comparison of both experiments allowed us to evaluate the advantages and disadvantages of using the data assimilation and to check how well WRF is able to close the water balance over the complex terrain of the IP. ERAI and several observational datasets (Radiosondes, MODIS, EOBS, ECA&D, TRMM, GPCP and GLEAM) were included in the validation of the terms of the water balance equation.

In the second part of the thesis, a comparison of daily precipitation downscaled dynamically by the above mentioned WRF simulations and statistically using the SDSM model was carried out in order to determine which technique produces better results. The SDSM was fed with predictors created from ERAI data at 0.75° in order

to design the closest configuration to that used for WRF. This way the advantages and disadvantages of each downscaling method can be determined.

This chapter is made of two sections. Section 8.1 will summarize the main results obtained in our study, contributing this way to the improvement of the state of knowledge. Then, section 8.2 will present some interesting lines of investigation left for future work following the topics covered by this thesis.

8.1 Conclusions

1. Chapter 3 includes the independent validations carried out for the most important terms of the water balance equation (equation 2.1). The validation of PW showed that the D experiment outperforms the N experiment, obtaining better correlation, SD and RMSE values for eight radiosondes evenly distributed over the IP. The D experiment is also able to improve the results from ERAI. Compared to MODIS data, similar results are obtained. The correlation values obtained by D are better than the results obtained by N and similar to those from ERAI.
2. The validation of precipitation against EOBS showed that both WRF simulations and ERAI presented poor correlation values in the Mediterranean coast and the Ebro basin. The poorest results were obtained by the N experiment, but the D experiment is able to correct them. Comparable results between ERAI and D are measured, but the D experiment outperformed ERAI in the south of the IP. Compared to the other observational datasets of precipitation (ECA&D, TRMM and GPCP), the D experiment obtains similar results to ERAI.
3. The validation of evaporation showed that the WRF model cannot simulate a realistic evaporation in every grid point whose land use is defined as *urban or built-up* in the NOAH land surface model. After all of these points were eliminated from the validation against GLEAM v3.0b and v3.0c datasets, comparable results between ERAI and the D experiment were measured. However, both ERAI and D presented really poor correlation values near the Mediterranean coast and in the northwestern corner of the IP. Even if the correlation values were comparable, the evaporation rate of ERAI overestimates the rate simulated by both GLEAM datasets, but also those from both WRF experiments.
4. The analysis of the residual calculated for both WRF simulations and ERAI showed that the leading terms of the balance were the tendency of the PW, the divergence of moisture flux, evaporation and precipitation. The terms related

to the condensates are not important. The effect of the data assimilation was perceptible in the residuals. They present remarkable changes within a day (especially at 18 UTC), related mainly to the assimilation of moisture and temperature observations in low levels. The residuals do not follow any easily recognizable pattern.

5. The D experiment is able to improve the results obtained by the experiment without data assimilation (N), and its results are similar to those obtained by ERAI. Thus, the most representative features of the water cycle simulated by this experiment (D) were studied. No recognizable patterns are observed for the evaporation. Nevertheless, the influence of the large scale precipitation in the Atlantic facade of the IP is recognizable in the annual accumulated precipitation maps. Remarkable high values of PW were observed in the coastal zones of Spain, particularly in summer.
6. The transboundary fluxes through the limits of the IP vary seasonally. A great amount of moisture enters the IP during the whole day in winter. However, the IP mainly exports moisture through the Mediterranean coast in spring, summer and, to a lesser extent, in autumn. Only during midday this tendency is reversed and moisture is imported due to the breezes, particularly in the southern coasts of Spain.
7. In chapter 4, twenty-one stations evenly spaced over the IP were chosen for the comparison of statistical and dynamical downscaling techniques. Each station was calibrated independently on the SDSM, following a methodology based only on the statistical scores provided by the model itself. That way, the knowledge about the climate of the region or the operator skill are not necessary.
8. The scores obtained by both WRF experiments and SDSM for correlation, standard deviation and RMSE are similar to those obtained from different observational datasets (EOBS, TRMM and GPCP). That means that both downscaling techniques have comparable skill to that between observational datasets. However, no downscaling technique was found superior to the other one across all the verification metrics. Depending on the metric studied, the most suitable technique varies.
9. Our results showed that the mean of the SDSM ensemble, D and ERAI produced similar correlation in four regions defined over the IP (Northern, Central, Mediterranean and Southwestern regions). If each member of the SDSM ensemble is checked, the scores are not comparable to those from the D experiment.
10. In order to check the strong points of the D experiment, SDSM mean and ensemble members, the LEPS and BSS scores were also studied. The members of the ensemble obtained the best LEPS scores in sixteen stations. In the remaining five stations, the best values were obtained by the D experiment. Systematically, the members of the ensemble and D outperformed the SDSM

mean. Conversely, according to the BSS score, the ensemble mean and D presented some added value when compared to the data used to drive those models, that were taken as the reference forecast (ERA-Interim). The same feature was not observed for the ensemble members. The reason why the members of the ensemble do not present any added value is because the BSS also takes into account the temporal occurrence of the precipitation, as was also in the case of correlation. This feature is not arbitrary, and it only reflects the idea that a downscaling technique will be optimal for a particular experiment depending on the forecast needed (deterministic or probabilistic) and the technical computer resources available.

11. Several precipitation indices were calculated. Starting by the precipitation amount indices, similar average precipitation is measured for D, SDSM mean and the ensemble members. However, the ensemble members outperformed the other experiments simulating the precipitation intensity and the 90th percentile. The SDSM mean is the one with the worst scores. If we change to the precipitation occurrence indices, the results change from one index to another. The observed maximum consecutive dry days and the probability of a wet-day is overestimated by the SDSM mean, while the D experiment and the members of the ensemble underestimate them. In contrast, the members of the ensemble overestimate the maximum five-days precipitation, but D and SDSM mean underestimate it. Overall, the D experiment presented a stable behaviour on every studied index, while the results for the SDSM experiment vary depending on the index.
12. The potential applicability of our WRF simulations in other fields was also explored in this thesis. The resolution of the domain ($15 \times 15 \text{ km}^2$) and the storage frequency of the outputs (every three hours) make these simulations suitable for a wide kind of studies. Water balance studies over land can be carried out in other regions included in our domain, but the studies can be carried out also over the Atlantic Ocean or the Mediterranean Sea. Both downscaled products could be also useful for extreme events and flood studies, but also for decision-making. It has been proved that the SDSM can produce similar results at site scales to those from the dynamical downscaling, but for longer periods and with less computational cost.
13. In chapter 5, our WRF simulations were validated against buoys and the CCMPv2 gridded dataset over water in the West Mediterranean. Similar results to those over land were observed, as the D experiment obtained similar scores to ERA-Interim, but better than N. The wind field of the D experiment was also applied for the calculation of the CF and AEP in the region. Two potential regions for the creation of wind farms were detected near cabo Begur and in the north of Menorca.
14. All of the calculations done during the thesis were carried out using the R software. Combining them with some programming codes for the calculation of

atmospheric thermodynamic variables, the *aiRthermo* package was created. It is publicly available on the CRAN repository since August 2017. Amongst the several functions included on it, the most important ones are those created for the calculation of the state of an air parcel, moisture indices, vertical evolutions and fully editable Stüve diagrams.

8.2 Future perspectives

Some open questions arisen during this study were left for future work. Here, some logical research projects that could follow this thesis are presented, taking into account the results obtained and everything learnt during this three-year period.

- The effect of enhancing the spatial and/or temporal resolution of the boundary conditions provided to WRF can be studied. For example, some new simulations should be created with the WRF model in order to analyse the effect of creating new background error covariances for the 3DVAR data assimilation step including SST data with a sub-daily temporal resolution. In this thesis, the SST provided to both WRF simulations was updated daily. However, the analysis of the residuals showed that the effect of the data assimilation step was remarkable during the afternoon, and not during the whole day. Thus, the effect of improving the temporal resolution of the data provided to the WRF model could be an interesting study.
- The static data defined within the NOAH land surface model should be further studied, as we have found that some problems can arise even if the basic configuration of the land surface model is used. Not only the land use or soil type categories should be re-evaluated, but also other categories such as vegetation fraction. In this thesis, the evaporation cannot be correctly simulated on many *urban or built-up* grid points. Then, the physical mechanisms that could explain WRF's inability to simulate a realistic evaporation over *urban or built-up* points must be identified. However, it must be taken into account that the effect of this problematic categories could extent the evaporation and affect also other variables not studied in this thesis.
- A comparison of the statistical and dynamical downscaling techniques was carried out in this thesis. However, since the SDSM provides a twenty-member ensemble, the comparison was carried out comparing the deterministic simulations created by WRF against the probabilistic results of SDSM. Then, it should be interesting to create an ensemble of simulations with WRF, made by changing the configuration of the physics of the model (that is, changing the parameterizations) or by changing the initial conditions of both simula-

tions. This way, a fair comparison between two probabilistic products could be carried out.

- The energy fluxes involved in the cold bias in the south of the IP during summer must be determined. Our study has proved that the data assimilation step is able to correct this cold bias in the model (see Figure 3.28), but most of the simulations created in the literature do not include the data assimilation step.
- The influence of two types of precipitation (large-scale and convective) can be identified in the results presented in this thesis. How well these different precipitation types are reproduced by dynamical and statistical downscaling is also an interesting topic to be developed in further research. In addition, the inter-annual or seasonal variability of precipitation simulated with WRF and SDSM could be also studied.
- The ability of WRF and SDSM to simulate actual precipitation regimes was tested in this thesis. However, this study could be extended to the evaluation of the skill of the models to reproduce climate changes. Because of the use of the data assimilation step, the WRF model cannot simulate future climate changes, but it could be useful for the simulation of those changes in the regimes observed during the 20th century.

Appendices

A Predictor suites for SDSM experiments

In this appendix we present the predictor suites generated for each SDSM experiment in section 4.1. Particularly, Figures A.1 and A.2 are the predictor suites for the N48 and E79 experiments, described in the main body as NCEP and ERA predictor suites respectively. Figures A.3 and A.4 are those predictor suites created for the N79 and E79r experiments.

NCEP Predictor Suite (Experiment N48)

	DSWR	MSLP	USUR	VSUR	DSUR	F500	U500	V500	Z500	H500	D500	F850	U850	V850	Z850	H850	D850	PREC	R500	R850	RSUR	R2N48	R2N79	R2E79	R2E79r				
Murcia	1	0	0	0	0	0	0	0	1	1	0	0	0	0	0	0	0	0	1	0	0	0	10.6	12.7	11.6	17.5			
Lisbon	0	1	0	0	0	0	1	0	0	1	0	0	1	0	0	0	0	0	1	0	1	0	11.2	11.4	6.2	9.5			
A Coruna	1	0	1	0	0	0	1	0	0	0	0	0	0	0	0	0	0	1	0	1	0	1	19.2	19.8	18.5	26.5			
Barcelona	0	0	0	0	0	0	0	1	0	1	1	0	0	0	0	0	0	0	1	0	0	0	7.5	11.3	9.1	14.1			
Madrid	1	1	0	0	0	0	0	1	0	1	0	0	0	0	0	0	0	0	1	1	1	0	18.5	17.2	16.3	20.8			
Santander	1	0	0	1	1	1	0	0	0	1	0	1	0	0	0	0	0	0	1	0	1	0	20.5	22.5	22.3	21			
Tarifa	1	0	0	0	0	0	0	0	0	1	1	1	0	0	0	0	0	0	1	0	1	0	16.1	20.4	14.3	24.9			
Caceres	1	1	0	0	0	0	0	0	0	0	0	0	1	0	0	0	0	0	1	0	1	0	15.8	18.8	22.2	21.1			
Albacete	0	0	0	0	0	0	0	1	1	1	0	0	0	0	0	0	0	0	1	0	1	0	11.7	16.2	11.5	18.9			
Huelva	1	0	0	0	0	0	0	0	0	1	1	0	1	0	0	0	0	0	1	0	1	1	1	15.1	14.7	26.2	20.7		
Ciudad Real	1	1	0	0	0	0	0	0	0	0	0	0	0	0	0	0	0	0	1	0	1	1	0	13.9	17.8	18.7	22.9		
Lleida	0	0	0	0	0	0	0	1	0	0	0	1	0	0	0	0	0	0	0	1	1	0	0	13.2	16.8	13.6	15.5		
Soria	1	1	0	0	0	0	0	0	0	1	0	0	0	0	0	0	0	0	0	1	1	0	0	11.7	13.5	16.9	16.9		
Pamplona	1	1	0	0	0	1	1	0	0	1	0	0	0	0	0	0	0	0	1	0	1	0	0	16.5	20.1	19	21.5		
Valladolid	1	1	1	0	0	0	0	1	0	0	0	0	0	0	0	0	0	0	1	0	1	1	0	0	14.7	16	20.9	22.6	
Gijon	1	1	0	0	0	1	1	0	0	1	0	1	0	0	0	0	0	0	0	1	1	0	0	17.9	19.8	18	27.8		
Almeria	1	0	0	0	0	0	0	1	0	0	0	0	0	0	0	0	0	0	0	1	0	0	0	15	13.5	18.1	17.9		
Cordoba	1	0	0	0	0	0	0	1	0	1	0	0	1	0	0	0	0	0	1	0	1	0	1	0	18.3	20.3	30.7	29.9	
Vigo	1	0	1	0	0	1	0	0	0	1	0	1	0	0	0	0	0	0	1	0	1	0	1	1	28.2	29.7	32.3	35.7	
Cast Plana	1	0	0	0	0	0	0	1	0	0	0	0	0	0	0	0	0	0	1	0	1	1	0	0	11.8	14.6	18.1	17.1	
Daroca	1	1	0	0	0	0	0	0	0	0	0	0	0	0	0	0	0	0	1	1	0	1	0	0	0	12.4	13.4	12.8	16.5

Figure A.1: SDSM predictor suite calibrated using N48 inputs. R2 values are for the validation period when SDSM is driven by N48, N79, E79 and E79r inputs respectively. This predictor suite is described in the main body text as the ‘NCEP predictor suite’. Acronyms of the predictors as defined in *Wilby and Dawson (2013)*.

ERA Predictor Suite (Experiment E79)

	DSWR	MSLP	USUR	VSUR	DSUR	F500	U500	V500	Z500	H500	D500	F850	U850	V850	Z850	H850	D850	PREC	R500	R850	RSUR	R2N48	R2N79	R2E79	R2E79r
Murcia	1	0	0	0	0	0	0	0	0	1	0	0	0	0	1	0	0	1	0	0	0	10.6	12.5	11.7	18.3
Lisbon	1	0	1	0	0	0	1	0	0	0	0	0	1	0	0	1	0	1	0	0	1	14.7	14.5	14.2	19.4
ACoruna	1	0	1	0	0	0	1	0	0	0	0	0	0	0	1	0	1	1	0	0	20.6	20.9	20.5	27.3	
Barcelona	1	0	0	0	0	0	0	1	0	0	0	0	0	0	1	0	1	0	1	1	6.7	11	10.7	15.6	
Madrid	1	1	0	0	0	0	0	1	0	0	0	0	0	0	1	0	1	1	0	0	14.8	13.2	15.3	21.1	
Santander	1	0	1	0	1	1	0	0	0	1	0	0	1	0	0	1	0	1	0	1	0	20.1	21.5	22.7	24
Tarifa	1	0	0	1	0	0	0	0	0	1	0	1	1	0	0	1	0	1	0	0	0	22.6	29	26.7	29.3
Caceres	1	1	0	0	0	0	0	0	0	0	0	1	0	0	0	1	0	1	0	0	0	15.8	18.8	22.2	21.1
Albacete	1	0	0	1	0	0	0	1	0	1	0	0	0	0	0	1	0	1	1	0	0	12.6	16	18.1	23.6
Huelva	1	0	0	1	1	0	0	0	0	1	0	0	1	0	0	1	0	1	0	0	0	15.7	18.7	24.5	24.5
Ciudad Real	1	1	0	0	0	0	0	0	0	0	0	0	1	0	0	1	0	1	1	0	0	13.9	17.8	18.7	22.9
Lleida	1	1	0	0	0	0	0	1	0	0	1	0	0	0	0	1	0	1	1	0	0	14.5	18.1	18.9	21.2
Soria	1	1	0	0	1	0	0	1	0	0	0	0	0	0	0	1	0	1	1	0	0	15.9	19.9	17.1	18.6
Pamplona	1	1	0	0	0	1	1	0	0	1	0	0	0	0	0	1	0	1	0	0	0	16.5	20.2	19	21.5
Valladolid	1	1	1	0	0	0	0	1	0	0	0	0	0	0	0	1	0	1	1	0	0	14.7	16	20.9	22.6
Gijon	1	0	1	0	1	0	0	0	0	1	0	0	0	0	0	0	0	1	1	0	0	19.4	21.9	20.7	28.1
Almeria	1	0	0	0	0	0	0	1	0	0	0	0	0	0	0	0	0	1	0	0	0	15	13.5	18.1	17.9
Cordoba	1	0	0	1	0	0	0	0	0	1	0	1	0	0	0	1	0	1	1	0	0	18.9	21.4	29.9	31.8
Vigo	1	1	0	1	0	0	1	0	0	1	0	0	1	0	0	1	0	1	0	1	1	31.9	32.8	37.4	38.6
Cast_Plana	1	0	0	0	0	0	0	0	0	1	0	0	0	0	0	0	0	1	0	0	0	11.4	13.5	17.2	16.5
Daroca	1	1	0	0	0	0	0	0	0	0	0	0	0	0	1	1	0	1	0	0	0	12.4	13.4	12.8	16.5

Figure A.2: As in Figure A.1 but for E79 inputs. This predictor suite is described in the main body text as the ERA predictor suite’.

Experiment N79 – Predictor Suite

	DSWR	MSLP	USUR	VSUR	DSUR	F500	U500	V500	Z500	H500	D500	F850	U850	V850	Z850	H850	D850	PREC	R500	R850	RSUR
Murcia	0	0	0	0	0	0	0	0	1	1	0	0	0	0	0	0	0	1	0	0	0
Lisbon	0	1	0	0	0	0	1	0	0	1	0	0	1	0	0	0	0	1	0	1	0
ACoruna	1	0	1	0	0	0	1	0	0	0	0	0	0	0	0	1	0	1	0	1	0
Barcelona	0	0	0	0	0	0	0	1	0	1	1	0	0	0	0	0	0	1	0	0	0
Madrid	1	1	0	0	0	0	0	1	0	1	0	0	0	0	0	0	1	1	1	0	0
Santander	1	0	0	1	1	1	0	0	0	1	0	1	0	0	0	0	0	1	0	1	0
Tarifa	1	0	0	0	0	1	0	0	0	1	1	0	0	0	0	1	0	1	0	0	0
Caceres	1	1	0	0	0	0	0	0	0	0	0	1	0	0	0	1	0	1	0	0	0
Albacete	1	0	0	0	0	0	0	1	0	1	0	0	0	0	0	0	0	1	0	0	0
Huelva	1	0	0	0	0	0	0	0	0	1	1	0	1	0	0	1	0	1	0	1	0
Ciudad Real	1	1	1	0	0	0	0	0	0	0	0	0	0	0	0	1	0	1	0	0	0
Lleida	0	0	0	0	0	0	0	1	0	0	1	0	0	0	0	0	0	1	1	0	0
Soria	1	1	0	0	0	0	0	0	0	1	0	0	0	0	0	0	0	1	1	0	0
Pamplona	1	1	0	0	0	1	1	0	0	1	0	0	0	0	0	1	0	1	0	0	0
Valladolid	1	1	1	0	0	0	0	1	0	0	0	0	0	0	0	1	0	1	1	0	0
Gijon	1	1	0	0	0	1	1	0	0	1	0	1	0	0	0	0	0	1	1	0	0
Almeria	1	0	0	0	0	0	0	1	0	0	0	0	0	0	0	0	0	1	0	0	0
Cordoba	1	0	0	0	0	0	0	1	0	1	0	0	1	0	0	1	0	1	0	1	0
Vigo	1	1	1	0	0	0	0	0	0	0	0	1	0	0	0	1	0	1	0	0	1
Cast_Plana	1	0	0	0	0	0	0	1	0	0	0	0	0	0	0	1	0	1	1	0	0
Daroca	0	1	0	0	0	0	0	0	0	0	0	0	0	0	1	1	0	1	0	0	0

Figure A.3: As in Figure A.1 but for N79 inputs.

Experiment E79r – Predictor Suite

	DSWR	MSLP	USUR	VSUR	DSUR	F500	U500	V500	Z500	H500	D500	F850	U850	V850	Z850	H850	D850	PREC	R500	R850	RSUR	
Murcia	1	0	0	0	0	0	0	0	0	1	0	0	0	0	0	1	0	0	1	0	0	0
Lisbon	1	0	1	0	0	0	1	0	0	0	0	0	1	0	0	1	0	1	0	0	0	1
ACoruna	1	0	0	0	0	0	1	0	0	0	0	0	0	0	0	1	0	1	1	0	0	0
Barcelona	1	0	0	0	0	0	0	0	0	1	0	0	0	0	0	1	0	1	0	0	0	0
Madrid	1	1	0	0	0	0	0	1	0	0	0	0	0	0	0	1	0	1	1	0	0	0
Santander	1	0	1	0	0	1	0	0	0	0	0	0	1	0	0	1	0	1	0	0	0	0
Tarifa	1	0	0	1	0	0	0	0	0	1	0	0	1	0	0	0	0	1	0	0	0	0
Caceres	1	1	0	0	0	0	0	0	0	0	0	0	0	0	0	1	0	1	0	0	0	0
Albacete	0	0	0	0	0	0	0	0	0	1	0	0	0	0	0	1	0	1	1	0	0	0
Huelva	1	0	0	1	0	0	0	0	0	1	0	0	1	0	0	1	0	1	0	0	0	0
Ciudad Real	1	1	0	0	0	0	0	0	0	0	0	0	0	0	0	1	0	1	1	0	0	0
Lleida	1	1	0	0	0	0	0	1	0	0	0	0	0	0	0	1	0	1	1	0	0	0
Soria	1	1	0	0	0	0	0	1	0	0	0	0	0	0	0	1	0	1	1	0	0	0
Pamplona	1	1	0	0	0	1	1	0	0	1	0	0	0	0	0	1	0	1	0	0	0	0
Valladolid	1	1	1	0	0	0	0	1	0	0	0	0	0	0	0	1	0	1	1	0	0	0
Gijon	1	0	0	0	0	0	0	0	0	1	0	0	0	0	0	0	0	1	1	0	0	0
Almeria	1	0	0	0	0	0	0	1	0	0	0	0	0	0	0	0	0	1	0	0	0	0
Cordoba	1	0	0	1	0	0	0	0	0	1	0	0	0	0	0	1	0	1	1	0	0	0
Vigo	1	1	0	1	0	0	1	0	0	1	0	0	1	0	0	1	0	1	0	1	1	1
Cast_Plana	1	0	0	0	0	0	0	0	0	1	0	0	0	0	0	0	0	1	0	0	0	0
Daroca	1	1	0	0	0	0	0	0	0	0	0	0	0	0	1	1	0	1	0	0	0	0

Figure A.4: As in Figure A.1 but for E79r inputs.

B Taylor diagrams for each region of the IP

This appendix includes every Taylor diagram created for the chosen stations over the IP. As stated in section 4.3 (Figure 4.7), four regions were defined: Northern, Central, Mediterranean and SouthWestern regions. Figure B.1 shows the results for the Northern region of the IP, including Vigo, A Coruña, Gijón and Santander stations. The Taylor diagrams for the central region are presented in Figure B.2, which includes Pamplona, Soria, Valladolid, Madrid and Daroca stations. The Taylor diagrams for Lleida, Barcelona, Castellón de la Plana, Almería and Murcia stations (Mediterranean region) are included in Figure B.3. Finally, the Taylor diagrams for the southwestern zone are presented in Figure B.4, including Lisbon, Cáceres, Ciudad Real, Albacete, Córdoba, Huelva and Tarifa.

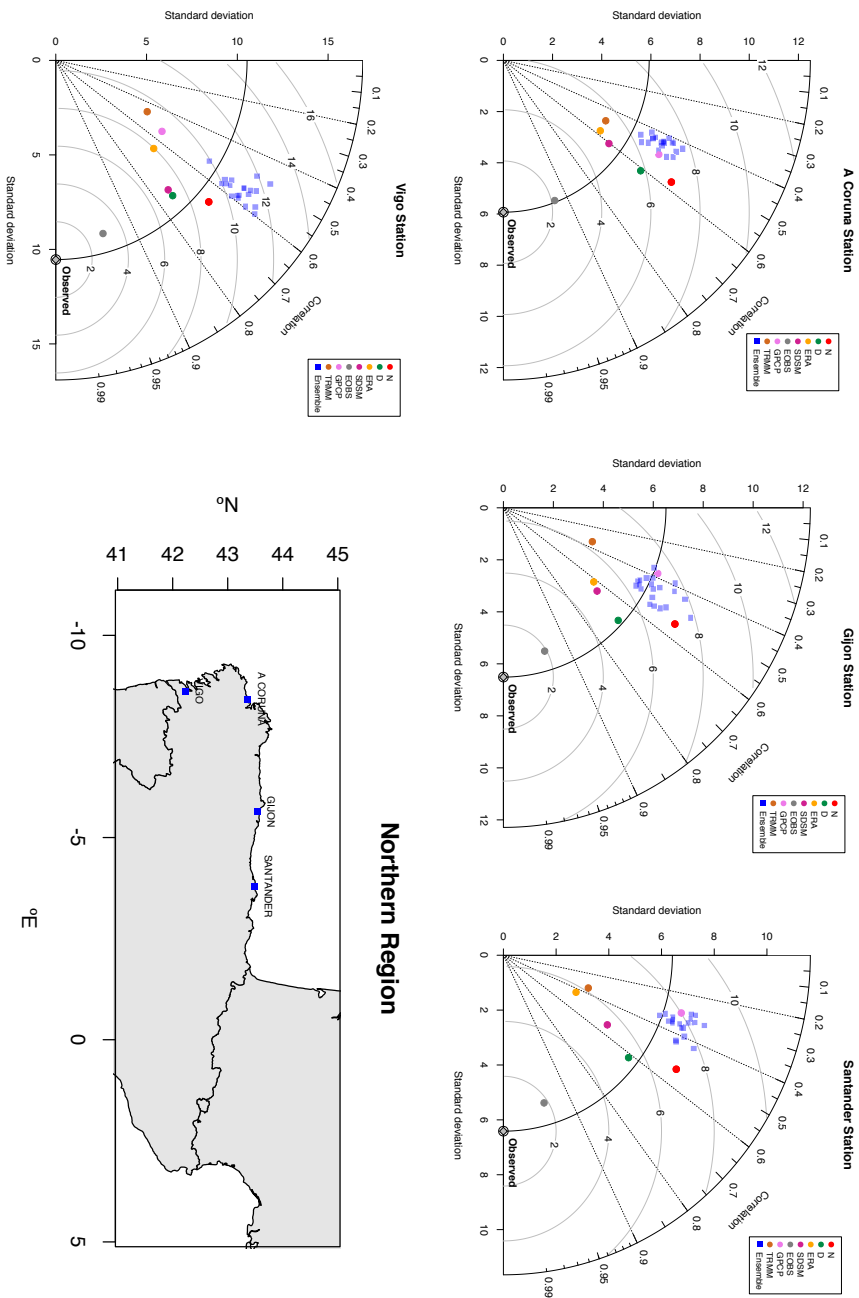


Figure B.1: Taylor diagrams for the Northern region. Seven experiments/datasets can be found on it: WRF N (red), WRF D (green), ERAI (orange), the SDSM ensemble mean (magenta), EOBS (grey), GPCC (violet) and TRMM (brown). Observed station data (grey diamond) and the members of the ensemble created by SDSM (blue squares) are also shown.

B TAYLOR DIAGRAMS FOR EACH REGION OF THE IP

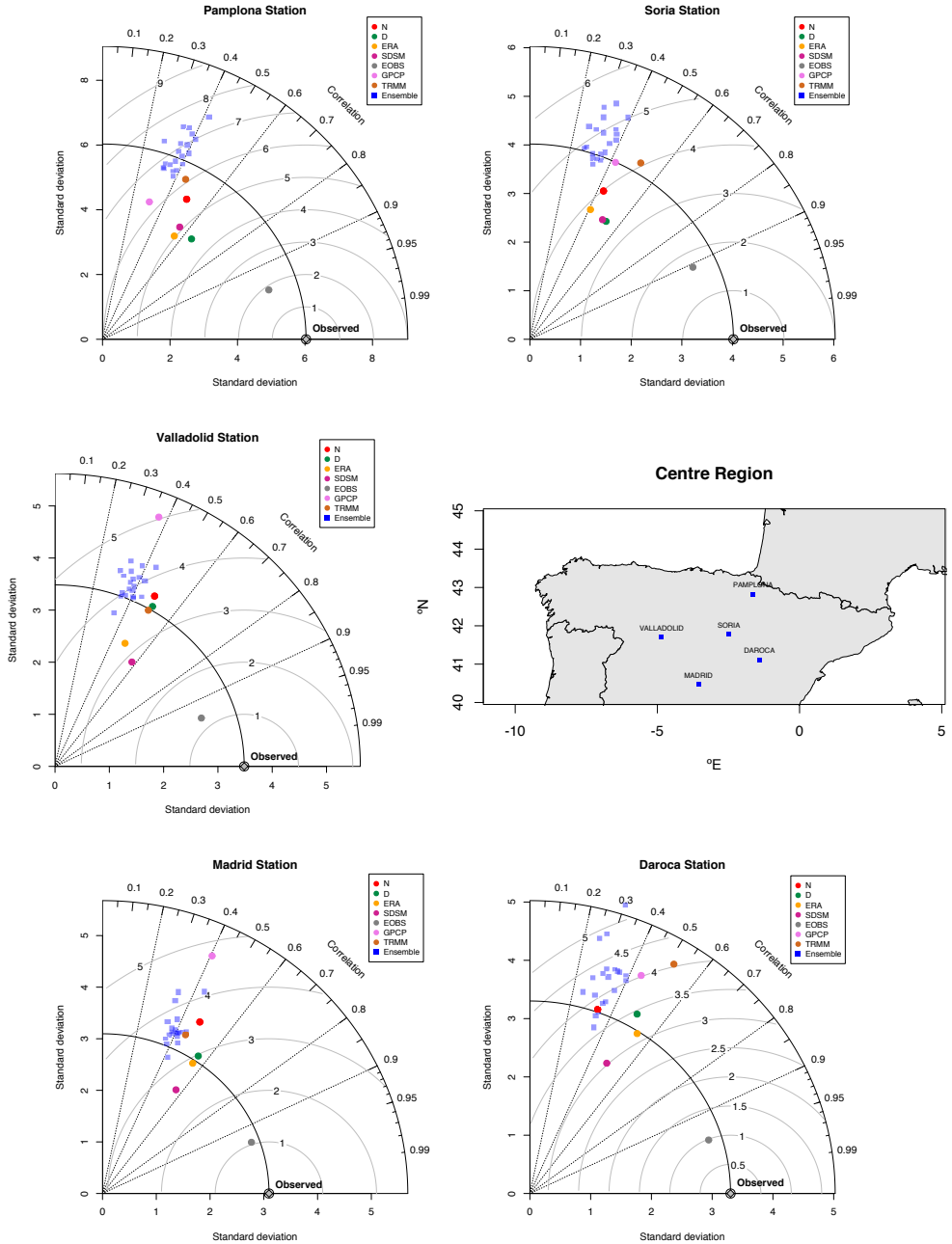
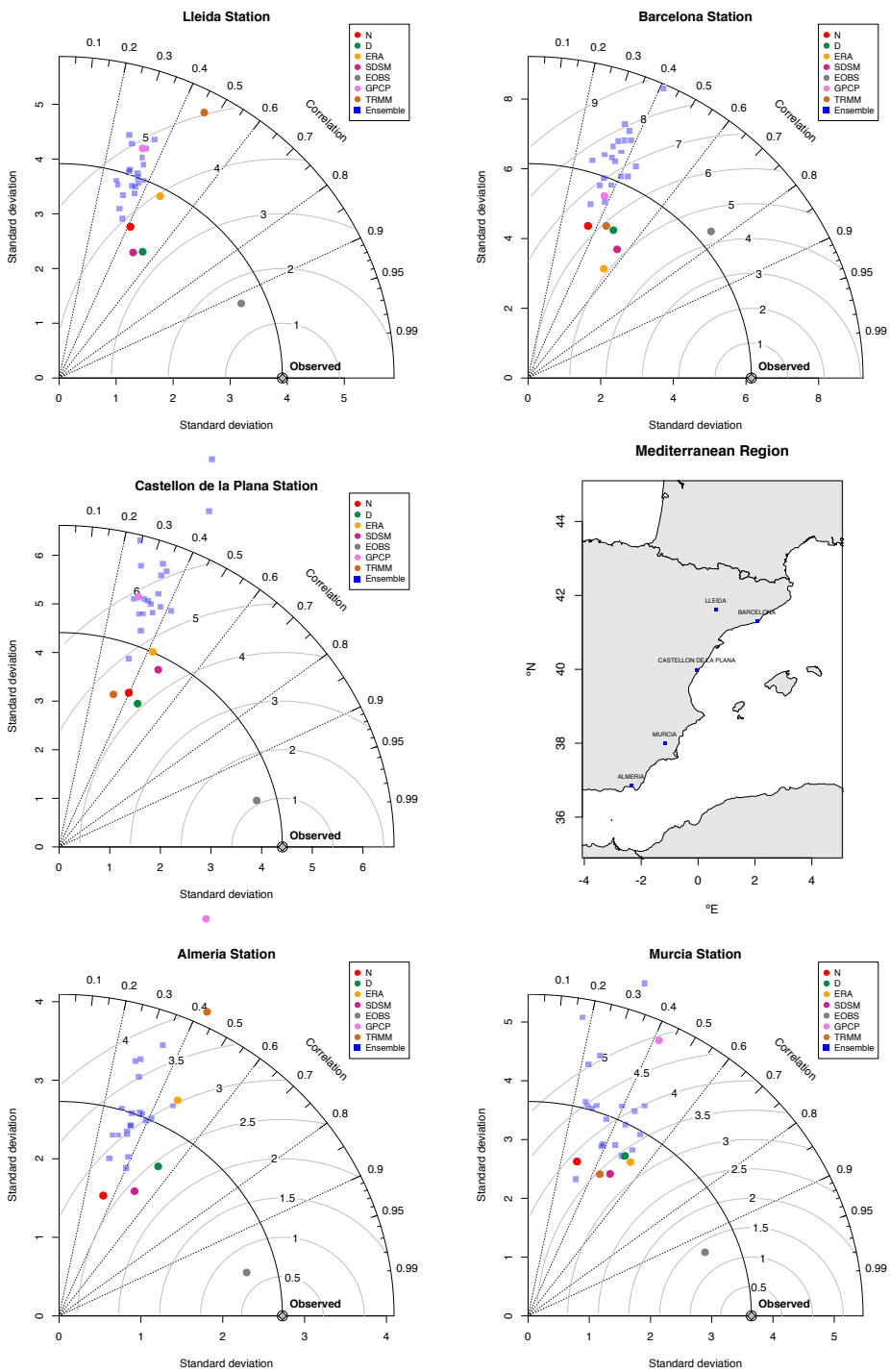


Figure B.2: Same as Figure B.1 but for the Central region.



114 Figure B.3: Same as Figures B.1 and B.2 but for the Mediterranean region.

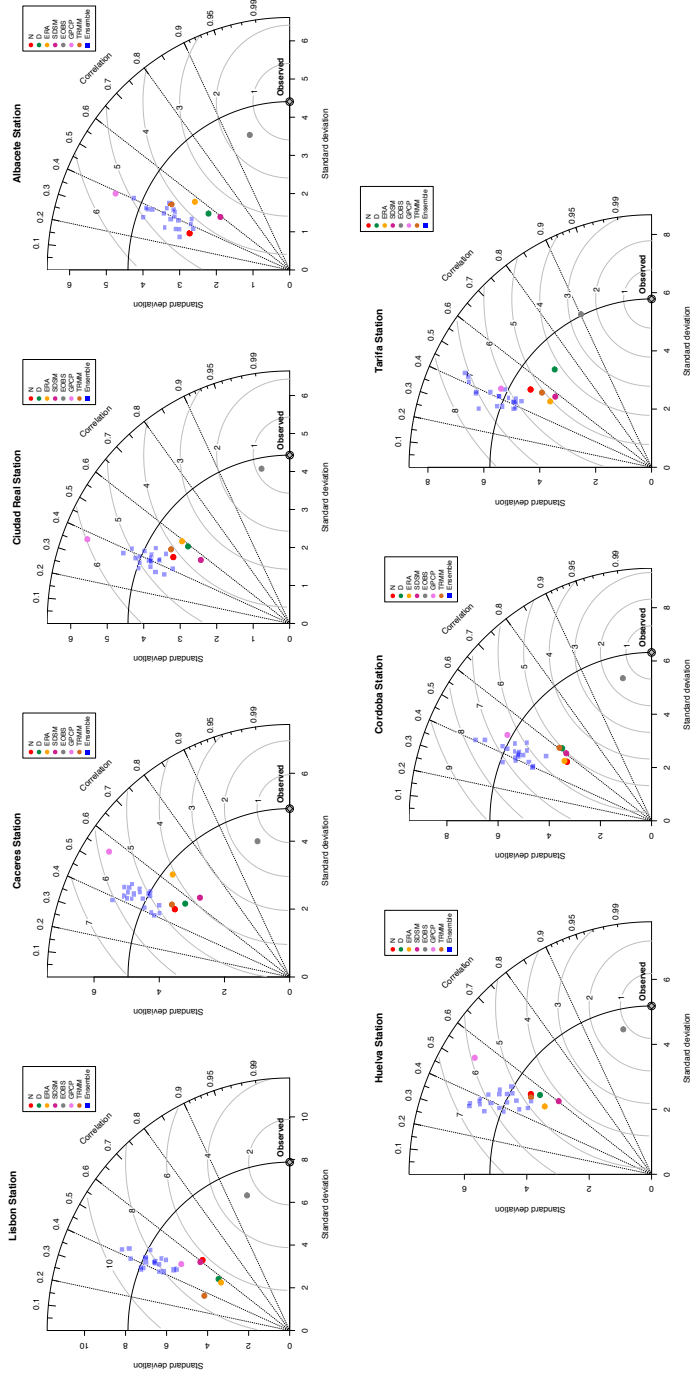


Figure B.4: Same as Figures B.1, B.2 and B.3 but for the Southwestern IP.

C Details on the methodology for the calculation of wind farm related variables

In this appendix we give more details about the methodology followed in chapter 5 for the calculation of the wind speed at 10 m from the measured wind at 3 m by the buoys, but also the one followed for the calculation of the CF and AEP of the turbines.

C.1 Wind at 10 m

All the buoys chosen for the study present their anemometer at 3 m. However, the nearest wind to that height that can be obtained from both WRF simulations is the wind at 10 m. Thus, it is necessary to estimate the measured wind at 10 m by the buoys.

To do so, the instantaneous roughness of the sea (z_0) was calculated by means of

Hsu's equation ([Hsu, 2003](#)):

$$\frac{z_0}{H_s} = 1200 \cdot \left(\frac{H_s}{L_p} \right)^{4.5} \quad (\text{C.1})$$

where L_p is the peak period wavelength (obtained from the records of each buoy) and H_s the significant wave height.

Once the instantaneous roughness was calculated, the logarithmic law of vertical wind shear was applied:

$$U(z) = U(z_r) + \frac{\ln((z + z_0)/z_0)}{\ln((z_r + z_0)/z_0)} \quad (\text{C.2})$$

where $U(z_r)$ is the wind speed at the reference level ($z = 3$ m) and $U(z)$ the estimation at the desired height. In this case, $z = 10$ m.

C.2 Capacity Factor and Annual Energy Production

In order to incorporate the effect of air density on wind speed, the CF and AEP were calculated with the normalized wind speed U_n . It is defined this way:

$$U_n = U \left(\frac{\rho}{\rho_0} \right)^3 \quad (\text{C.3})$$

where ρ_0 is the density of the air at sea level and at 15°C according to the Standard Atmosphere model (1.225 kg/m³).

According to equations 6.62 to 6.64 in [Masters \(2013\)](#), the CF of a turbine is defined as:

$$CF = 0.087 \cdot \overline{U_n} - \frac{P_R}{D^2} \quad (\text{C.4})$$

depending on the mean wind speed in m/s (in this case, the mean normalized wind speed for period 2010-2014), the rated power P_R in KW and the diameter of the wind turbine D in m.

Once the CF is calculated, it is easy to calculate the AEP of a turbine (in TW h/year) as:

$$E_a = CF \cdot P_R \cdot 365.25 \cdot 24 \cdot 10^{-12} \quad (\text{C.5})$$

Bibliography

- Accadia, C., S. Mariani, M. Casaioli, A. Lavagnini, and A. Speranza (2003), Sensitivity of precipitation forecast skill scores to bilinear interpolation and a simple nearest-neighbor average method on high-resolution verification grids, *Weather and Forecasting*, 18(5), 918–932, doi:10.1175/1520-0434(2003)018<0918:SOPFSS>2.0.CO;2.
- AEMET (2011), *Atlas climático ibérico: Temperatura del aire y precipitación (1971-2000)*, Agencia Estatal de Meteorología (AEMET).
- Amante, C., and B. Eakins (2009), ETOPO1 1 Arc-Minute Global Relief Model: Procedures, Data Sources and Analysis. NOAA Technical Memorandum NESDIS NGDC-24., National Geophysical Data Center, NOAA., doi:10.7289/V5C8276M.
- Angevine, W. M., E. Bazile, D. Legain, and D. Pino (2014), Land surface spinup for episodic modeling, *Atmospheric Chemistry and Physics*, 14(15), 8165–8172, doi:10.5194/acp-14-8165-2014.
- Argüeso, D., J. M. Hidalgo-Muñoz, S. R. Gámiz-Fortis, M. J. Esteban-Parra, J. Dudhia, and Y. Castro-Díez (2011), Evaluation of WRF parameterizations for climate studies over southern Spain using a multistep regionalization, *Journal of Climate*, 24(21), 5633–5651, doi:10.1175/JCLI-D-11-00073.1.

-
- Atlas, R., R. N. Hoffman, J. Ardizzone, S. M. Leidner, J. C. Jusem, D. K. Smith, and D. Gombos (2011), A Cross-Calibrated, multiplatform ocean surface wind velocity product for meteorological and oceanographic applications, *Bulletin of the American Meteorological Society*, *92*(2), 157–174, doi:10.1175/2010BAMS2946.1.
- Bangash, R. F., A. Passuello, M. Sanchez-Canales, M. Terrado, A. López, F. J. Elorza, G. Ziv, V. Acuña, and M. Schuhmacher (2013), Ecosystem services in Mediterranean river basin: Climate change impact on water provisioning and erosion control, *Science of The Total Environment*, *458-460*, 246 – 255, doi: <https://doi.org/10.1016/j.scitotenv.2013.04.025>.
- Barker, D., X.-Y. Huang, Z. Liu, T. Auligné, X. Zhang, S. Rugg, R. Ajjaji, A. Bourgeois, J. Bray, Y. Chen, M. Demirtas, Y.-R. Guo, T. Henderson, W. Huang, H.-C. Lin, J. Michalakes, S. Rizvi, and X. Zhang (2012), The Weather Research and Forecasting model’s community variational/ensemble data assimilation system: WRFDA, *Bulletin of the American Meteorological Society*, *93*(6), 831–843, doi:10.1175/BAMS-D-11-00167.1.
- Belo-Pereira, M., E. Dutra, and P. Viterbo (2011), Evaluation of global precipitation data sets over the Iberian Peninsula, *Journal of Geophysical Research: Atmospheres*, *116*(D20), doi:10.1029/2010JD015481.
- Berberly, E. H., and E. M. Rasmusson (1999), Mississippi moisture budgets on regional scales, *Monthly Weather Review*, *127*(11), 2654–2673, doi:10.1175/1520-0493(1999)127<2654:MMBORS>2.0.CO;2.
- Berrisford, P., D. Dee, P. Poli, R. Brugge, K. Fielding, M. Fuentes, P. Kållberg, S. Kobayashi, S. Uppala, and A. Simmons (2011), The ERA-Interim archive Version 2.0, Shinfield Park, Reading, 23 pp.
- Bohren, C., and B. Albrecht (1998), *Atmospheric Thermodynamics*, Oxford University Press, New York.
- Borge, R., V. Alexandrov, J. J. del Vas, J. Lumbreras, and E. Rodríguez (2008), A comprehensive sensitivity analysis of the WRF model for air quality applications over the Iberian Peninsula, *Atmospheric Environment*, *42*, 8560–8574, doi:10.1016/j.atmosenv.2008.08.032.
- Buck, A. L. (1981), New equations for computing vapor pressure and enhancement factor, *Journal of Applied Meteorology*, *20*(12), 1527–1532, doi:10.1175/1520-0450(1981)020<1527:NEFCVP>2.0.CO;2.
- Cardoso, R. M., P. M. M. Soares, P. M. A. Miranda, and M. Belo-Pereira (2013), WRF high resolution simulation of Iberian mean and extreme precipitation climate, *International Journal of Climatology*, *33*(11), 2591–2608, doi:10.1002/joc.3616.
- Casanueva, A., S. Herrera, J. Fernández, and J. Gutiérrez (2016), Towards a fair comparison of statistical and dynamical downscaling in the framework of

- the EURO-CORDEX initiative, *Climatic Change*, 137(3), 411–426, doi:10.1007/s10584-016-1683-4.
- Casati, B., L. J. Wilson, D. B. Stephenson, P. Nurmi, A. Ghelli, M. Pocernich, U. Damrath, E. E. Ebert, B. G. Brown, and S. Mason (2008), Forecast verification: Current status and future directions, *Meteorological Applications*, 15(1), 3–18, doi:10.1002/met.52.
- Cavazos, T. (2000), Using self-organizing maps to investigate extreme climate events: An application to wintertime precipitation in the Balkans, *Journal of Climate*, 13(10), 1718–1732, doi:10.1175/1520-0442(2000)013<1718:USOMTI>2.0.CO;2.
- Cavazos, T., and B. C. Hewitson (2005), Performance of NCEP–NCAR reanalysis variables in statistical downscaling of daily precipitation, *Climate Research*, 28(2), 95–107.
- Chaudhuri, S., J. Pal, A. Middey, and S. Goswami (2013), Nowcasting Bordoichila with a composite stability index, *Natural Hazards*, 66(2), 591–607, doi:10.1007/s11069-012-0504-y.
- Christensen, O. B. (1999), Relaxation of soil variables in a regional climate model, *Tellus A*, 51(5), 674–685, doi:10.1034/j.1600-0870.1999.00010.x.
- Craven, J. P., R. E. Jewell, and H. E. Brook (2002), Comparison between observed convective cloud-base heights and lifting condensation level for two different lifted parcels, *Weather and Forecasting*, 17(4), 885–890, doi:10.1175/1520-0434(2002)017<0885:CBOCCB>2.0.CO;2.
- Crawford, T., N. L. Betts, and D. Favis-Mortlock (2007), GCM grid-box choice and predictor selection associated with statistical downscaling of daily precipitation over Northern Ireland, *Climate Research*, 34(2), 145–160.
- Czernecki, B., M. Taszarek, L. Kolendowicz, and K. Szyga-Pluta (2015), Atmospheric conditions of thunderstorms in the European part of the Arctic derived from sounding and reanalysis data, *Atmospheric Research*, 154(Supplement C), 60–72, doi:https://doi.org/10.1016/j.atmosres.2014.11.001.
- de Coning, E., M. Koenig, and J. Olivier (2011), The combined instability index: a new very-short range convection forecasting technique for southern Africa, *Meteorological Applications*, 18(4), 421–439, doi:10.1002/met.234.
- Dee, D. P., S. M. Uppala, A. J. Simmons, P. Berrisford, P. Poli, S. Kobayashi, U. Andrae, M. A. Balmaseda, G. Balsamo, P. Bauer, P. Bechtold, A. C. M. Beljaars, L. van de Berg, J. Bidlot, N. Bormann, C. Delsol, R. Dragani, M. Fuentes, A. J. Geer, L. Haimberger, S. B. Healy, H. Hersbach, E. V. Hólm, L. Isaksen, P. Kållberg, M. Köhler, M. Matricardi, A. P. McNally, B. M. Monge-Sanz, J.-J. Morcrette, B.-K. Park, C. Peubey, P. de Rosnay, C. Tavolato, J.-N. Thépaut, and F. Vitart (2011), The ERA-Interim reanalysis: Configuration and performance of

-
- the data assimilation system, *Quarterly Journal of the Royal Meteorological Society*, 137(656), 553–597, doi:10.1002/qj.828.
- Díez, E., C. Primo, J. A. García-Moya, J. M. Gutiérrez, and B. Orfila (2005), Statistical and dynamical downscaling of precipitation over Spain from DEMETER seasonal forecasts, *Tellus A*, 57(3), 409–423, doi:10.1111/j.1600-0870.2005.00130.x.
- Djuric, D. (1994), *Weather Analysis*, Prentice Hall, New Jersey.
- Domínguez, M., R. Romera, S. E. L. Fita, J. Fernández, P. Jiménez-Guerrero, J. P. Montávez, W. D. Cabos, G. Liguori, and M. A. Gaertner (2013), Present-climate precipitation and temperature extremes over Spain from a set of high resolution RCMs, *Clim. Res.*, 58, 149–164, doi:10.3354/cr01186.
- Dosio, A. (2016), Projections of climate change indices of temperature and precipitation from an ensemble of bias-adjusted high-resolution EURO-CORDEX regional climate models, *Journal of Geophysical Research: Atmospheres*, 121, 5488–5511, doi:10.1002/2015JD024411.
- ECMWF (2015), *Part IV: Physical Processes*, chap. 7, IFS Documentation, ECMWF, operational implementation 12 May 2015.
- Eiras-Barca, J., S. Brands, and G. Miguez-Macho (2016), Seasonal variations in North Atlantic atmospheric river activity and associations with anomalous precipitation over the Iberian Atlantic margin, *Journal of Geophysical Research: Atmospheres*, 121, 931–948, doi:10.1002/2015JD023379.
- Emanuel, K. A. (1994), *Atmospheric Convection*, Oxford University Press, New York.
- Esteban-Parra, M. J., F. S. Rodrigo, and Y. Castro-Diez (1998), Spatial and temporal patterns of precipitation in Spain for the period 1880–1992, *International Journal of Climatology*, 18(14), 1557–1574, doi:10.1002/(SICI)1097-0088(19981130)18:14<1557::AID-JOC328>3.0.CO;2-J.
- Fealy, R., and J. Sweeney (2007), Statistical downscaling of precipitation for a selection of sites in Ireland employing a generalised linear modelling approach, *International Journal of Climatology*, 27(15), 2083–2094, doi:10.1002/joc.1506.
- Feistel, R., and W. Wagner (2006), A new equation of state for H₂O ice Ih, *Journal of Physical and Chemical Reference Data*, 35(2), 1021–1047, doi:10.1063/1.2183324.
- Fernández, J., and J. Sáenz (2003), Improved field reconstruction with the analog method: Searching the CCA space, *Climate Research*, 24(3), 199–213.
- Fernández, J., J. Sáenz, and E. Zorita (2003), Analysis of wintertime atmospheric moisture transport and its variability over Southern Europe in the NCEP Reanalyses, *Climate Research*, 23(3), 195–215.

- Fernández, J., J. P. Montávez, J. Sáenz, J. F. González-Rouco, and E. Zorita (2007), Sensitivity of the MM5 mesoscale model to physical parameterizations for regional climate studies: Annual cycle, *Journal of Geophysical Research: Atmospheres*, *112*(D4), doi:10.1029/2005JD006649.
- Fernández-Ferrero, A., J. Sáenz, G. Ibarra-Berastegi, and J. Fernández (2009), Evaluation of statistical downscaling in short range precipitation forecasting, *Atmospheric Research*, *94*(3), 448 – 461, doi:https://doi.org/10.1016/j.atmosres.2009.07.007.
- Feser, F., B. Rockel, H. von Storch, J. Winterfeldt, and M. Zahn (2011), Regional climate models add value to global model data: A review and selected examples, *Bulletin of the American Meteorological Society*, *92*(9), 1181–1192, doi:10.1175/2011BAMS3061.1.
- Foley, A. (2010), Uncertainty in regional climate modelling: A review, *Progress in Physical Geography*, *34*(5), 647–670, doi:10.1177/0309133310375654.
- Fowler, H. J., and R. L. Wilby (2007), Beyond the downscaling comparison study, *International Journal of Climatology*, *27*(12), 1543–1545, doi:10.1002/joc.1616.
- Frías, M. D., S. Herrera, A. S. Cofiño, and J. M. Gutiérrez (2010), Assessing the skill of precipitation and temperature seasonal forecasts in Spain: Windows of opportunity related to ENSO events, *Journal of Climate*, *23*(2), 209–220, doi:10.1175/2009JCLI2824.1.
- Gampe, D., G. Nikulin, and R. Ludwig (2016), Using an ensemble of regional climate models to assess climate change impacts on water scarcity in European river basins, *Science of The Total Environment*, *573*, 1503 – 1518, doi:https://doi.org/10.1016/j.scitotenv.2016.08.053.
- Gao, B.-C., and Y. J. Kaufman (2003), Water vapor retrievals using Moderate Resolution Imaging Spectroradiometer (MODIS) near-infrared channels, *Journal of Geophysical Research: Atmospheres*, *108*(D13), doi:10.1029/2002JD003023, 4389.
- García-Díez, M., J. Fernández, D. San-Martín, S. Herrera, and J. M. Gutiérrez (2015), Assessing and improving the local added value of WRF for wind downscaling, *Journal of Applied Meteorology and Climatology*, *54*(7), 1556–1568, doi:10.1175/JAMC-D-14-0150.1.
- García-Valdecasas Ojeda, M., S. R. Gámiz-Fortis, Y. Castro-Díez, and M. J. Esteban-Parra (2017), Evaluation of WRF capability to detect dry and wet periods in Spain using drought indices, *Journal of Geophysical Research: Atmospheres*, *122*(3), 1569–1594, doi:10.1002/2016JD025683.
- Gimeno, L., R. Nieto, R. M. Trigo, S. M. Vicente-Serrano, and J. I. López-Moreno (2010), Where does the Iberian Peninsula moisture come from? An answer based on a Lagrangian approach, *Journal of Hydrometeorology*, *11*(2), 421–436, doi:10.1175/2009JHM1182.1.

-
- Giorgi, F. (2006), Regional climate modeling: Status and perspectives, *Journal de Physique IV (Proceedings)*, 139, 101–118, doi:10.1051/jp4:2006139008.
- Giorgi, F., and X. Bi (2000), A study of internal variability of a regional climate model, *Journal of Geophysical Research: Atmospheres*, 105(D24), 29,503–29,521, doi:10.1029/2000JD900269.
- Gómez-Hernández, M., A. Drumond, L. Gimeno, and R. Garcia-Herrera (2013), Variability of moisture sources in the Mediterranean region during the period 1980–2000, *Water Resources Research*, 49, 6781–6794, doi:10.1002/wrcr.20538.
- Gómez-Navarro, J. J., J. P. Montávez, S. Jerez, P. Jiménez-Guerrero, and E. Zorita (2012), What is the role of the observational dataset in the evaluation and scoring of climate models?, *Geophys. Res. Lett.*, 39, L24,701, doi:10.1029/2012GL054206.
- Goodess, C., C. Anagnostopoulou, A. Bárdossy, C. Frei, C. Harpham, M. R. Haylock, Y. Hundecha, P. Maheras, J. Ribalaygua, J. Schmidli, T. Schmith, K. Tolika, R. Tomozeiu, and R. L. Wilby (2007), An intercomparison of statistical downscaling methods for Europe and European regions - Assessing their performance with respect to extreme temperature and precipitation events, *Climatic Change*.
- Goodess, C. M., and P. D. Jones (2002), Links between circulation and changes in the characteristics of Iberian rainfall, *International Journal of Climatology*, 22(13), 1593–1615, doi:10.1002/joc.810.
- Goodess, C. M., and J. P. Palutikof (1998), Development of daily rainfall scenarios for southeast Spain using a circulation-type approach to downscaling, *International Journal of Climatology*, 18(10), 1051–1083, doi:10.1002/(SICI)1097-0088(199808)18:10<1051::AID-JOC304>3.0.CO;2-1.
- Gulacha, M. M., and D. M. Mulungu (2017), Generation of climate change scenarios for precipitation and temperature at local scales using SDSM in Wami-Ruvu River Basin Tanzania, *Physics and Chemistry of the Earth, Parts A/B/C*, 100, 62 – 72, doi:https://doi.org/10.1016/j.pce.2016.10.003.
- Gutmann, E. D., R. M. Rasmussen, C. Liu, K. Ikeda, D. J. Gochis, M. P. Clark, J. Dudhia, and G. Thompson (2012), A comparison of statistical and dynamical downscaling of winter precipitation over complex terrain, *Journal of Climate*, 25(1), 262–281, doi:10.1175/2011JCLI4109.1.
- Gutowski Jr., W. J., Y. Chen, and Z. Ötles (1997), Atmospheric water vapor transport in NCEP-NCAR reanalyses: Comparison with river discharge in the central United States, *Bulletin of the American Meteorological Society*, 78, 1957–1969, doi:10.1175/1520-0477(1997)078<1957:AWVTIN>2.0.CO;2.
- Hannachi, A., I. T. Jolliffe, and D. B. Stephenson (2007), Empirical orthogonal functions and related techniques in atmospheric science: A review, *International Journal of Climatology*, 27(9), 1119–1152, doi:10.1002/joc.1499.

- Hanssen-Bauer, I., C. Achberger, R. E. Benestad, D. Chen, and E. J. Førland (2005), Statistical downscaling of climate scenarios over Scandinavia, *Climate Research*, *29*(3), 255–268.
- Hashmi, M. Z., A. Y. Shamseldin, and B. W. Melville (2011), Comparison of SDSM and LARS-WG for simulation and downscaling of extreme precipitation events in a watershed, *Stochastic Environmental Research and Risk Assessment*, *25*(4), 475–484, doi:10.1007/s00477-010-0416-x.
- Hastings, D. A., and P. K. Dunbar (1999), Global land one-kilometer base elevation (GLOBE) digital elevation model, documentation, *Key to Geophysical records documentation (KGRD)*, *34*(1.0).
- Haylock, M. R., and C. M. Goodess (2004), Interannual variability of European extreme winter rainfall and links with mean large-scale circulation, *International Journal of Climatology*, *24*(6), 759–776, doi:10.1002/joc.1033.
- Haylock, M. R., G. C. Cawley, C. Harpham, R. L. Wilby, and C. M. Goodess (2006), Downscaling heavy precipitation over the United Kingdom: a comparison of dynamical and statistical methods and their future scenarios, *International Journal of Climatology*, *26*(10), 1397–1415, doi:10.1002/joc.1318.
- Haylock, M. R., N. Hofstra, A. M. G. Klein Tank, E. J. Klok, P. D. Jones, and M. New (2008), A European daily high-resolution gridded data set of surface temperature and precipitation for 1950–2006, *Journal of Geophysical Research: Atmospheres*, *113*(D20), doi:10.1029/2008JD010201.
- Herrera, S., J. M. Gutiérrez, R. Ancell, M. R. Pons, M. D. Frías, and J. Fernández (2012), Development and analysis of a 50-year high-resolution daily gridded precipitation dataset over Spain (Spain02), *International Journal of Climatology*, *32*(1), 74–85, doi:10.1002/joc.2256.
- Herrera, S., J. Fernández, and J. M. Gutiérrez (2016), Update of the Spain02 gridded observational dataset for EURO-CORDEX evaluation: assessing the effect of the interpolation methodology, *International Journal of Climatology*, *36*(2), 900–908, doi:10.1002/joc.4391.
- Hirschi, M., S. I. Seneviratne, and C. Schär (2006), Seasonal variations in terrestrial water storage for major midlatitude river basins, *Journal of Hydrometeorology*, *7*(1), 39–60, doi:10.1175/JHM480.1.
- Hong, S.-Y., J. Dudhia, and S.-H. Chen (2004), A revised approach to ice microphysical processes for the bulk parameterization of clouds and precipitation, *Monthly Weather Review*, *132*(1), 103–120, doi:10.1175/1520-0493(2004)132<0103:ARATIM>2.0.CO;2.
- Hsu, S. A. (2003), Estimating overwater friction velocity and exponent of power-law wind profile from gust factor during storms, *Journal of Waterway, Port, Coastal,*

-
- and Ocean Engineering*, 129(4), 174–177, doi:10.1061/(ASCE)0733-950X(2003)129:4(174).
- Huffman, G. J., R. F. Adler, M. M. Morrissey, D. T. Bolvin, S. Curtis, R. Joyce, B. McGavock, and J. Susskind (2001), Global precipitation at one-degree daily resolution from multisatellite observations, *Journal of Hydrometeorology*, 2(1), 36–50, doi:10.1175/1525-7541(2001)002<0036:GPAODD>2.0.CO;2.
- Humphrey, G. B., H. R. Maier, W. Wu, N. J. Mount, G. C. Dandy, R. J. Abraham, and C. W. Dawson (2017), Improved validation framework and R-package for artificial neural network models, *Environmental Modelling & Software*, 92(Supplement C), 82 – 106, doi:https://doi.org/10.1016/j.envsoft.2017.01.023.
- Huth, R. (2005), Downscaling of humidity variables: a search for suitable predictors and predictands, *International Journal of Climatology*, 25(2), 243–250, doi:10.1002/joc.1122.
- Iacono, M. J., J. S. Delamere, E. J. Mlawer, M. W. Shephard, S. A. Clough, and W. D. Collins (2008), Radiative forcing by long-lived greenhouse gases: Calculations with the AER radiative transfer models, *Journal of Geophysical Research: Atmospheres*, 113(D13), doi:10.1029/2008JD009944.
- Ibarra-Berastegi, G., J. Saénz, A. Ezcurra, A. Elías, J. Diaz Argandoña, and I. Errasti (2011), Downscaling of surface moisture flux and precipitation in the Ebro Valley (Spain) using analogues and analogues followed by random forests and multiple linear regression, *Hydrology and Earth System Sciences*, 15(6), 1895–1907, doi:10.5194/hess-15-1895-2011.
- Iglesias, A., L. Garrote, F. Flores, and M. Moneo (2007), Challenges to manage the risk of water scarcity and climate change in the Mediterranean, *Water Resources Management*, 21(5), 775–788, doi:10.1007/s11269-006-9111-6.
- Jerez, S., J. P. Montávez, J. J. Gómez-Navarro, P. Jiménez-Guerrero, J. Jiménez, and J. F. González-Rouco (2010), Temperature sensitivity to the land-surface model in MM5 climate simulations over the Iberian Peninsula, *Meteorologische Zeitschrift*, 19(4), 363–374, doi:10.1127/0941-2948/2010/0473.
- Jerez, S., J. P. Montávez, J. J. Gómez-Navarro, P. A. Jiménez, P. Jiménez-Guerrero, R. Lorente, and J. F. González-Rouco (2012), The role of the land-surface model for climate change projections over the Iberian Peninsula, *Journal of Geophysical Research: Atmospheres*, 117(D1), doi:10.1029/2011JD016576.
- Jerez, S., J. P. Montávez, J. J. Gomez-Navarro, R. Lorente-Plazas, J. A. Garcia-Valero, and P. Jimenez-Guerrero (2013), A multi-physics ensemble of regional climate change projections over the Iberian Peninsula, *Climate Dynamics*, 41(7), 1749–1768, doi:10.1007/s00382-012-1551-5.

- Jiménez, P. A., and J. Dudhia (2012), Improving the representation of resolved and unresolved topographic effects on surface wind in the WRF model, *J. Appl. Meteor. Climatol.*, *51*, 300–316, doi:10.1175/JAMC-D-11-084.1.
- Jiménez, P. A., and J. Dudhia (2013), On the ability of the WRF Model to reproduce the surface wind direction over complex terrain, *Journal of Applied Meteorology and Climatology*, *52*(7), 1610–1617, doi:10.1175/JAMC-D-12-0266.1.
- Jiménez, P. A., J. F. González-Rouco, E. García-Bustamante, J. Navarro, J. P. Montávez, J. V.-G. de Arellano, J. Dudhia, and A. Muñoz-Roldan (2010), Surface wind regionalization over complex terrain: Evaluation and analysis of a high-resolution WRF simulation, *J. Appl. Met.*, *49*, 268–287, doi:10.1175/2009JAMC2175.1.
- Jiménez-Guerrero, P., J. Montávez, M. Domínguez, R. Romera, L. Fita, J. Fernández, W. Cabos, G. Liguori, and M. Gaertner (2013), Mean fields and interannual variability in RCM simulations over Spain: The ESCENA project, *Climate Research*, *57*(3), 201–220.
- Jones, R. G., J. M. Murphy, and M. Noguer (1995), Simulation of climate change over Europe using a nested regional-climate model. I: Assessment of control climate, including sensitivity to location of lateral boundaries, *Quarterly Journal of the Royal Meteorological Society*, *121*(526), 1413–1449, doi:10.1002/qj.49712152610.
- Kiladis, G. N., and H. F. Diaz (1989), Global climatic anomalies associated with extremes in the Southern Oscillation, *Journal of Climate*, *2*(9), 1069–1090, doi:10.1175/1520-0442(1989)002<1069:GCAAWE>2.0.CO;2.
- Klein Tank, A. M. G., J. B. Wijngaard, G. P. Können, R. Böhm, G. Demarée, A. Gocheva, M. Mileta, S. Pashiardis, L. Hejkrlik, C. Kern-Hansen, R. Heino, P. Bessemoulin, G. Müller-Westermeier, M. Tzanakou, S. Szalai, T. Pálsdóttir, D. Fitzgerald, S. Rubin, M. Capaldo, M. Maugeri, A. Leitass, A. Bukantis, R. Aberfeld, A. F. V. van Engelen, E. Forland, M. Miletus, F. Coelho, C. Mares, V. Razuvaev, E. Nieplova, T. Cegnar, J. Antonio López, B. Dahlström, A. Moberg, W. Kirchhofer, A. Ceylan, O. Pachaliuk, L. V. Alexander, and P. Petrovic (2002), Daily dataset of 20th-century surface air temperature and precipitation series for the European Climate Assessment, *International Journal of Climatology*, *22*(12), 1441–1453, doi:10.1002/joc.773.
- Kottek, M., J. Grieser, C. Beck, B. Rudolf, and F. Rubel (2006), World map of the Köppen-Geiger climate classification updated, *Meteorologische Zeitschrift*, *15*(3), 259–263, doi:doi:10.1127/0941-2948/2006/0130.
- Letkewicz, C. E., and M. D. Parker (2010), Forecasting the maintenance of mesoscale convective systems crossing the Appalachian Mountains, *Weather and Forecasting*, *25*(4), 1179–1195, doi:10.1175/2010WAF2222379.1.

-
- Leung, L. R., and Y. Qian (2009), Atmospheric rivers induced heavy precipitation and flooding in the western U.S. simulated by the WRF regional climate model, *Geophysical Research Letters*, *36*(3), doi:10.1029/2008GL036445.
- Lim, Y.-J., J. Hong, and T.-Y. Lee (2012), Spin-up behavior of soil moisture content over East Asia in a land surface model, *Meteorology and Atmospheric Physics*, *118*(3), 151–161, doi:10.1007/s00703-012-0212-x.
- Lionello, P., M. Gacic, D. Gomis, R. Garcia-Herrera, F. Giorgi, S. Planton, R. Trigo, A. Theocharis, M. N. Tsimplis, U. Ulbrich, and E. Xoplaki (2012), Program focuses on climate of the Mediterranean region, *Eos, Transactions American Geophysical Union*, *93*(10), 105–106, doi:10.1029/2012EO100001.
- Liu, X., P. Coulibaly, and N. Evora (2007), Comparison of data-driven methods for downscaling ensemble weather forecasts, *Hydrology and Earth System Sciences Discussions*, *4*(1), 189–210.
- López-Parages, J., and B. Rodríguez-Fonseca (2012), Multidecadal modulation of El Niño influence on the Euro-Mediterranean rainfall, *Geophysical Research Letters*, *39*(2), doi:10.1029/2011GL050049.
- Lorenzo, M. N., J. J. Taboada, I. Iglesias, and M. Gómez-Gesteira (2011), Predictability of the spring rainfall in Northwestern Iberian Peninsula from sea surfaces temperature of ENSO areas, *Climatic Change*, *107*(3), 329–341, doi:10.1007/s10584-010-9991-6.
- Mahmood, R., and M. S. Babel (2013), Evaluation of SDSM developed by annual and monthly sub-models for downscaling temperature and precipitation in the Jhelum basin, Pakistan and India, *Theoretical and Applied Climatology*, *113*(1), 27–44, doi:10.1007/s00704-012-0765-0.
- Mahmood, R., and M. S. Babel (2014), Future changes in extreme temperature events using the Statistical DownScaling Model (SDSM) in the trans-boundary region of the Jhelum river basin, *Weather and Climate Extremes*, *5-6*, 56 – 66, doi:https://doi.org/10.1016/j.wace.2014.09.001.
- Martens, B., D. G. Miralles, H. Lievens, R. van der Schalie, R. A. M. de Jeu, D. Fernández-Prieto, H. E. Beck, W. A. Dorigo, and N. E. C. Verhoest (2017), GLEAM v3: Satellite-based land evaporation and root-zone soil moisture, *Geoscientific Model Development*, *10*(5), 1903–1925, doi:10.5194/gmd-10-1903-2017.
- Mason, I. (1982), A model for assessment of weather forecasts, *Aust. Meteor. Mag.*, *30*(4), 291–303.
- Masters, G. M. (2013), *Renewable and efficient electric power systems*, John Wiley & Sons.

- Miralles, D. G., T. R. H. Holmes, R. A. M. De Jeu, J. H. Gash, A. G. C. A. Meesters, and A. J. Dolman (2011), Global land-surface evaporation estimated from satellite-based observations, *Hydrology and Earth System Sciences*, *15*(2), 453–469, doi:10.5194/hess-15-453-2011.
- Montávez, J. P., J. M. López-Romero, S. Jerez, J. J. Gómez-Navarro, and P. Jiménez-Guerrero (2017), How much spin-up period is really necessary in regional climate simulations?, in *EGU General Assembly Conference Abstracts*, vol. 19, p. 15806.
- Moseley, S. (2011), From observations to forecasts – Part 12: Getting the most out of model data, *Weather*, *66*(10), 272–276, doi:10.1002/wea.844.
- Muñoz-Díaz, D., and F. S. Rodrigo (2004), Spatio-temporal patterns of seasonal rainfall in Spain (1912–2000) using cluster and principal component analysis: comparison, *Annales Geophysicae*, *22*(5), 1435–1448.
- Nakanishi, M., and H. Niino (2006), An Improved Mellor–Yamada Level-3 Model: Its Numerical Stability and Application to a Regional Prediction of Advection Fog, *Boundary-Layer Meteorology*, *119*(2), 397–407, doi:10.1007/s10546-005-9030-8.
- Navascués, B., J. Calvo, G. Morales, C. Santos, A. Callado, A. Cansado, J. Cuxart, M. Díez, P. del Río, P. Escribà, O. García-Colombo, J. García-Moya, C. Geijo, E. Gutiérrez, M. Hortal, I. Martínez, B. Orfila, J. Parodi, E. Rodríguez, J. Sánchez-Arriola, I. Santos-Atienza, and J. Simarro (2013), Long-term verification of HIRLAM and ECMWF forecasts over Southern Europe: History and perspectives of Numerical Weather Prediction at AEMET, *Atmospheric Research*, *125*(Supplement C), 20 – 33, doi:https://doi.org/10.1016/j.atmosres.2013.01.010.
- Nicholls, N., and W. Murray (1999), Workshop on indices and indicators for climate extremes: Asheville, NC, USA, 3–6 june 1997 breakout group b: Precipitation, *Climatic Change*, *42*(1), 23–29, doi:10.1023/A:1005495627778.
- North, G. R., and T. L. Erukhimova (2009), *Atmospheric Thermodynamics: elementary physics and chemistry*, Cambridge University Press, New York.
- Önol, B. (2012), Effects of coastal topography on climate: high-resolution simulation with a regional climate model, *Climate Research*, *52*, 159–174.
- Ortiz de Galisteo, J. P., V. Cachorro, C. Toledano, B. Torres, N. Laulainen, Y. Benouna, and A. de Frutos (2011), Diurnal cycle of precipitable water vapor over Spain, *Quarterly Journal of the Royal Meteorological Society*, *137*(657), 948–958, doi:10.1002/qj.811.
- Osma, V. C., J. E. C. Romá, and M. A. P. Martín (2015), Modelling regional impacts of climate change on water resources: the Júcar basin, Spain, *Hydrological Sciences Journal*, *60*(1), 30–49, doi:10.1080/02626667.2013.866711.

-
- Paredes, D., R. M. Trigo, R. Garcia-Herrera, and I. F. Trigo (2006), Understanding precipitation changes in Iberia in early spring: Weather typing and storm-tracking approaches, *Journal of Hydrometeorology*, 7(1), 101–113, doi:10.1175/JHM472.1.
- Parrish, D. F., and J. C. Derber (1992), The National Meteorological Center’s Spectral Statistical-Interpolation Analysis System, *Monthly Weather Review*, 120, 1747–1763, doi:10.1175/1520-0493(1992)120<1747:TNMCSS>2.0.CO;2.
- Peel, M. C., B. L. Finlayson, and T. A. McMahon (2007), Updated world map of the Köppen-Geiger climate classification, *Hydrology and Earth System Sciences Discussions*, 4(2), 439–473.
- Peixoto, J., and A. Oort (1992), *Physics of Climate*, New York, NY (United States); American Institute of Physics.
- Petty, G. W. (2008), *A First Course in Atmospheric Thermodynamics*, Sundog Publishing, Madison.
- Quadrelli, R., V. Pavan, and F. Molteni (2001), Wintertime variability of Mediterranean precipitation and its links with large-scale circulation anomalies, *Climate Dynamics*, 17(5), 457–466, doi:10.1007/s003820000121.
- Reynolds, R. W., T. M. Smith, C. Liu, D. B. Chelton, K. S. Casey, and M. G. Schlax (2007), Daily high-resolution-blended analyses for sea surface temperature, *Journal of Climate*, 20(22), 5473–5496, doi:10.1175/2007JCLI1824.1.
- Rios-Entenza, A., and G. Miguez-Macho (2014), Moisture recycling and the maximum of precipitation in spring in the Iberian Peninsula, *Climate Dynamics*, 42(11), 3207–3231, doi:10.1007/s00382-013-1971-x.
- Rios-Entenza, A., P. M. M. Soares, R. M. Trigo, R. M. Cardoso, and G. Miguez-Macho (2014), Moisture recycling in the Iberian Peninsula from a regional climate simulation: Spatiotemporal analysis and impact on the precipitation regime, *Journal of Geophysical Research: Atmospheres*, 119, 5895–5912, doi:10.1002/2013JD021274.
- Rockel, B., C. L. Castro, R. A. Pielke, H. von Storch, and G. Leoncini (2008), Dynamical downscaling: Assessment of model system dependent retained and added variability for two different regional climate models, *Journal of Geophysical Research: Atmospheres*, 113(D21), doi:10.1029/2007JD009461.
- Rodó, X., E. Baert, and F. A. Comín (1997), Variations in seasonal rainfall in Southern Europe during the present century: Relationships with the North Atlantic Oscillation and the El Niño-Southern Oscillation, *Climate Dynamics*, 13(4), 275–284, doi:10.1007/s003820050165.

- Rodríguez-Puebla, C., A. H. Encinas, S. Nieto, and J. Garmendia (1998), Spatial and temporal patterns of annual precipitation variability over the Iberian Peninsula, *International Journal of Climatology*, 18(3), 299–316, doi:10.1002/(SICI)1097-0088(19980315)18:3<299::AID-JOC247>3.0.CO;2-L.
- Rodríguez-Puebla, C., A. H. Encinas, and J. Sáenz (2001), Winter precipitation over the Iberian Peninsula and its relationship to circulation indices, *Hydrology and Earth System Sciences*, 5, 233–244, doi:10.5194/hess-5-233-2001.
- Rogers, R., and M. K. Yau (1989), *A Short Course in Cloud Physics, 3rd Edition*, Pergamon Press, Oxford.
- Romero, R., C. Ramis, and J. Guijarro (1999), Daily rainfall patterns in the Spanish Mediterranean area: An objective classification, *International Journal of Climatology*, 19, 95–112, doi:10.1002/(SICI)1097-0088(199901)19:1<95::AID-JOC344>3.0.CO;2-S.
- Rubel, F., K. Brugger, K. Haslinger, and I. Auer (2017), The climate of the European Alps: Shift of very high resolution Köppen-Geiger climate zones 1800–2100, *Meteorologische Zeitschrift*, 26(2), 115–125, doi:10.1127/metz/2016/0816.
- Rummukainen, M. (2010), State-of-the-art with regional climate models, *Wiley Interdisciplinary Reviews: Climate Change*, 1(1), 82–96, doi:10.1002/wcc.8.
- Sáenz, J., C. Rodríguez-Puebla, J. Fernández, and J. Zubillaga (2001), Interpretation of interannual winter temperature variations over Southwestern Europe, *Journal of Geophysical Research: Atmospheres*, 106(D18), 20,641–20,651, doi:10.1029/2001JD900247.
- Schmidli, J., C. Frei, and P. L. Vidale (2006), Downscaling from GCM precipitation: a benchmark for dynamical and statistical downscaling methods, *International Journal of Climatology*, 26(5), 679–689, doi:10.1002/joc.1287.
- Schmidli, J., C. M. Goodess, C. Frei, M. R. Haylock, Y. Hundecha, J. Ribalaygua, and T. Schmith (2007), Statistical and dynamical downscaling of precipitation: An evaluation and comparison of scenarios for the European Alps, *Journal of Geophysical Research: Atmospheres*, 112, doi:10.1029/2005JD007026.
- Schoof, J., and S. Pryor (2001), Downscaling temperature and precipitation: A comparison of regression-based methods and artificial neural networks, *International Journal of Climatology*, 21(7), 773–790, doi:10.1002/joc.655.
- Serrano, A., J. A. García, V. L. Mateos, M. L. Cancillo, and J. Garrido (1999), Monthly modes of variation of precipitation over the Iberian Peninsula, *Journal of Climate*, 12(9), 2894–2919, doi:10.1175/1520-0442(1999)012<2894:MMOVOP>2.0.CO;2.
- Siedlecki, M. (2009), Selected instability indices in Europe, *Theoretical and Applied Climatology*, 96(1), 85–94, doi:10.1007/s00704-008-0034-4.

-
- Skamarock, W. C., J. B. Klemp, J. Dudhia, D. O. Gill, D. M. Barker, M. G. Duda, X.-Y. Huang, W. Wang, and J. G. Powers (2008), A description of the advanced research WRF version 3, *NCAR Technical Note NCAR/TN-475+STR*, doi:10.5065/D68S4MVH.
- Snider, J. B. (2000), Long-term observations of cloud liquid, water vapor, and cloud-base temperature in the North Atlantic Ocean, *Journal of Atmospheric and Oceanic Technology*, *17*, 928–939, doi:10.1175/1520-0426(2000)017<0928:LTOOCL>2.0.CO;2.
- Soares, P. M. M., R. M. Cardoso, P. M. A. Miranda, J. de Medeiros, M. Belo-Pereira, and F. Espiritu-Santo (2012), WRF high resolution dynamical downscaling of ERA-Interim for Portugal, *Clim. Dyn.*, *39*, 2497–2522, doi:10.1007/s00382-012-1315-2.
- Soares, P. M. M., R. M. Cardoso, J. a. J. Ferreira, and P. M. A. Miranda (2015), Climate change and the Portuguese precipitation: ENSEMBLES regional climate models results, *Climate Dynamics*, *45*, 1771–1787, doi:10.1007/s00382-014-2432-x.
- Sousa, P. M., R. M. Trigo, D. Barriopedro, P. M. M. Soares, A. M. Ramos, and M. L. R. Liberato (2017), Responses of European precipitation distributions and regimes to different blocking locations, *Climate Dynamics*, *48*, 1141–1160, doi:10.1007/s00382-016-3132-5.
- Stacke, T., and S. Hagemann (2016), Lifetime of soil moisture perturbations in a coupled land–atmosphere simulation, *Earth System Dynamics*, *7*(1), 1–19, doi:10.5194/esd-7-1-2016.
- Storch, H. v., and F. W. Zwiers (1999), *Statistical Analysis in Climate Research*, Cambridge University Press, doi:10.1017/CBO9780511612336.
- Tang, J., X. Niu, S. Wang, H. Gao, X. Wang, and J. Wu (2016), Statistical downscaling and dynamical downscaling of regional climate in China: Present climate evaluations and future climate projections, *Journal of Geophysical Research: Atmospheres*, *121*(5), 2110–2129, doi:10.1002/2015JD023977.
- Taylor, K. E. (2001), Summarizing multiple aspects of model performance in a single diagram, *Journal of Geophysical Research: Atmospheres*, *106*(D7), 7183–7192, doi:10.1029/2000JD900719.
- Tewari, M., F. Chen, W. Wang, J. Dudhia, M. LeMone, K. Mitchell, M. Ek, G. Gayno, J. Wegiel, and R. Cuenca (2004), Implementation and verification of the unified NOAA land surface model in the WRF model, in *20th conference on weather analysis and forecasting/16th conference on numerical weather prediction*, vol. 1115.
- Thyer, M., M. Leonard, D. Kavetski, S. Need, and B. Renard (2011), The open source RFortran library for accessing R from Fortran, with applications in environmental

- modelling, *Environmental Modelling & Software*, 26(2), 219 – 234, doi:<https://doi.org/10.1016/j.envsoft.2010.05.007>.
- Tiedtke, M. (1989), Comprehensive mass flux scheme for cumulus parameterization in large-scale models, *Monthly Weather Review*, 117(8), 1779–1800, doi:{10.1175/1520-0493(1989)117<1779:ACMFSF>2.0.CO;2}.
- Timbal, B., and D. A. Jones (2008), Future projections of winter rainfall in southeast Australia using a statistical downscaling technique, *Climatic Change*, 86(1), 165–187, doi:10.1007/s10584-007-9279-7.
- Trenberth, K. E., and C. J. Guillemot (1998), Evaluation of the atmospheric moisture and hydrological cycle in the NCEP/NCAR reanalyses, *Climate Dynamics*, 14(3), 213–231, doi:10.1007/s003820050219.
- Trenberth, K. E., L. Smith, T. Qian, A. Dai, and J. Fasullo (2007), Estimates of the global water budget and its annual cycle using observational and model data, *Journal of Hydrometeorology*, 8(4), 758–769, doi:10.1175/JHM600.1.
- Trigo, I. F., T. D. Davies, and G. R. Bigg (1999), Objective climatology of cyclones in the Mediterranean region, *Journal of Climate*, 12(6), 1685–1696, doi:10.1175/1520-0442(1999)012<1685:OCOCIT>2.0.CO;2.
- Trigo, R. M., and J. P. Palutikof (2001), Precipitation scenarios over Iberia: A comparison between direct GCM output and different downscaling techniques, *Journal of Climate*, 14(23), 4422–4446, doi:10.1175/1520-0442(2001)014<4422:PSOIAAC>2.0.CO;2.
- Tsonis, A. A. (2002), *An Introduction to Atmospheric Thermodynamics*, Cambridge University Press, Cambridge.
- Tullot, I. F. (2000), *Climatología de España y Portugal*, vol. 76, Universidad de Salamanca.
- Tustison, B., D. Harris, and E. Foufoula-Georgiou (2001), Scale issues in verification of precipitation forecasts, *Journal of Geophysical Research: Atmospheres*, 106(D11), 11,775–11,784, doi:10.1029/2001JD900066.
- Ulazia, A., J. Sáenz, and G. Ibarra-Berastegui (2016), Sensitivity to the use of 3DVAR data assimilation in a mesoscale model for estimating offshore wind energy potential. A case study of the Iberian northern coastline, *Applied Energy*, 180(Supplement C), 617 – 627, doi:<https://doi.org/10.1016/j.apenergy.2016.08.033>.
- Ulazia, A., J. Sáenz, G. Ibarra-Berastegui, S. J. González-Rojí, and S. Carreno-Madinabeitia (2017), Using 3DVAR data assimilation to measure offshore wind energy potential at different turbine heights in the West Mediterranean, *Applied Energy*, 208(Supplement C), 1232 – 1245, doi:<https://doi.org/10.1016/j.apenergy.2017.09.030>.

-
- van den Besselaar, E. J. M., M. R. Haylock, G. van der Schrier, and A. M. G. Klein Tank (2011), A European daily high-resolution observational gridded data set of sea level pressure, *Journal of Geophysical Research: Atmospheres*, 116(D11), doi:10.1029/2010JD015468.
- Vérant, S., K. Laval, J. Polcher, and M. D. Castro (2004), Sensitivity of the continental hydrological cycle to the spatial resolution over the Iberian Peninsula, *Journal of Hydrometeorology*, 5(2), 267–285, doi:10.1175/1525-7541(2004)005<0267:SOTCHC>2.0.CO;2.
- Vicente-Serrano, S. M., R. M. Trigo, J. I. López-Moreno, M. L. R. Liberato, J. Lorenzo-Lacruz, S. Beguería, E. Morán-Tejeda, and A. E. Kenawy (2011), Extreme winter precipitation in the Iberian Peninsula in 2010: Anomalies, driving mechanisms and future projections, *Climate Research*, 46(1), 51–65.
- Vicente-Serrano, S. M., C. Azorín-Molina, A. Sánchez-Lorenzo, E. Morán-Tejeda, J. Lorenzo-Lacruz, J. Revuelto, J. I. López-Moreno, and F. Espejo (2014), Temporal evolution of surface humidity in Spain: Recent trends and possible physical mechanisms, *Climate Dynamics*, 42, 2655–2674, doi:10.1007/s00382-013-1885-7.
- Viceto, C., M. Marta-Almeida, and A. Rocha (2017), Future climate change of stability indices for the Iberian Peninsula, *International Journal of Climatology*, 37(12), 4390–4408, doi:10.1002/joc.5094.
- von Storch, H. (2006), *Encyclopedia of Hydrological Sciences*, chap. Models of Global and Regional Climate, John Wiley & Sons, Ltd, doi:10.1002/0470848944.hsa035.
- von Storch, H., E. Zorita, and U. Cubasch (1993), Downscaling of global climate change estimates to regional scales: An application to Iberian rainfall in winter-time, *Journal of Climate*, 6(6), 1161–1171, doi:10.1175/1520-0442(1993)006<1161:DOGCCE>2.0.CO;2.
- Vujović, D., M. Paskota, N. Todorović, and V. Vučković (2015), Evaluation of the stability indices for the thunderstorm forecasting in the region of belgrade, serbia, *Atmospheric Research*, 161-162(Supplement C), 143 – 152, doi:https://doi.org/10.1016/j.atmosres.2015.04.005.
- Wallace, J. M., and P. V. Hobbs (2006), *Atmospheric Science: An Introductory Survey, 2nd Edition*, Elsevier, Oxford.
- Wang, J.-J., R. F. Adler, G. J. Huffman, and D. Bolvin (2014), An updated TRMM composite climatology of tropical rainfall and its validation, *Journal of Climate*, 27(1), 273–284, doi:10.1175/JCLI-D-13-00331.1.
- Ward, M. N., and C. K. Folland (1991), Prediction of seasonal rainfall in the north nordeste of Brazil using eigenvectors of sea-surface temperature, *International Journal of Climatology*, 11(7), 711–743, doi:10.1002/joc.3370110703.

- Weichert, A., and G. Bürger (1998), Linear versus nonlinear techniques in downscaling, *Climate Research*, 10(2), 83–93.
- Wetterhall, F., A. Bárdossy, D. Chen, S. Halldin, and C.-Y. Xu (2006), Daily precipitation-downscaling techniques in three Chinese regions, *Water Resources Research*, 42(11), doi:10.1029/2005WR004573.
- Wetterhall, F., S. Halldin, and C.-Y. Xu (2007), Seasonality properties of four statistical-downscaling methods in central Sweden, *Theoretical and Applied Climatology*, 87(1), 123–137, doi:10.1007/s00704-005-0223-3.
- Wilby, R., C. Dawson, and E. Barrow (2002), SDSM — a decision support tool for the assessment of regional climate change impacts, *Environmental Modelling & Software*, 17(2), 145 – 157, doi:https://doi.org/10.1016/S1364-8152(01)00060-3.
- Wilby, R. L., and C. W. Dawson (2013), The Statistical DownScaling Model: insights from one decade of application, *International Journal of Climatology*, 33(7), 1707–1719, doi:10.1002/joc.3544.
- Wilby, R. L., and T. M. L. Wigley (2000), Precipitation predictors for downscaling: observed and general circulation model relationships, *International Journal of Climatology*, 20, 641–661.
- Wilby, R. L., and D. Yu (2013), Rainfall and temperature estimation for a data sparse region, *Hydrology and Earth System Sciences*, 17(10), 3937.
- Wilby, R. L., H. Hassan, and K. Hanaki (1998), Statistical downscaling of hydrometeorological variables using general circulation model output, *Journal of Hydrology*, 205(1), 1 – 19, doi:https://doi.org/10.1016/S0022-1694(97)00130-3.
- Wilby, R. L., L. E. Hay, W. J. Gutowski, R. W. Arritt, E. S. Takle, Z. Pan, G. H. Leavesley, and M. P. Clark (2000), Hydrological responses to dynamically and statistically downscaled climate model output, *Geophysical Research Letters*, 27(8), 1199–1202, doi:10.1029/1999GL006078.
- Wilby, R. L., C. W. Dawson, C. Murphy, P. O’Connor, and E. Hawkins (2014), The Statistical DownScaling Model - Decision Centric (SDSM-DC): conceptual basis and applications, *Climate Research*, 61(3), 259–276.
- Wilks, D. S. (1992), Adapting stochastic weather generation algorithms for climate change studies, *Climatic Change*, 22(1), 67–84, doi:10.1007/BF00143344.
- Winterfeldt, J., B. Geyer, and R. Weisse (2011), Using QuikSCAT in the added value assessment of dynamically downscaled wind speed, *International Journal of Climatology*, 31(7), 1028–1039, doi:10.1002/joc.2105.
- Wu, Y., S. Liu, and W. Yan (2014), A universal Model-R Coupler to facilitate the use of R functions for model calibration and analysis, *Environmental Modelling & Software*, 62(Supplement C), 65 – 69, doi:https://doi.org/10.1016/j.envsoft.2014.08.012.

-
- Xu, K.-M., and D. A. Randall (1996), A semiempirical cloudiness parameterization for use in climate models, *Journal of the Atmospheric Sciences*, *53*(21), 3084–3102, doi:10.1175/1520-0469(1996)053<3084:ASCPFU>2.0.CO;2.
- Yang, W., A. Bárdossy, and H.-J. Caspary (2010), Downscaling daily precipitation time series using a combined circulation- and regression-based approach, *Theoretical and Applied Climatology*, *102*(3), 439–454, doi:10.1007/s00704-010-0272-0.
- Yeh, P. J.-F., and J. S. Famiglietti (2008), Regional terrestrial water storage change and evapotranspiration from terrestrial and atmospheric water balance computations, *Journal of Geophysical Research: Atmospheres*, *113*(D9), doi:10.1029/2007JD009045.
- Zhang, C., Y. Wang, and K. Hamilton (2011), Improved representation of boundary layer clouds over the Southeast Pacific in ARW-WRF using a modified Tiedtke Cumulus Parameterization Scheme, *Monthly Weather Review*, *139*(11), 3489–3513, doi:10.1175/MWR-D-10-05091.1.
- Zheng, D., R. Van Der Velde, Z. Su, J. Wen, and X. Wang (2017), Assessment of Noah land surface model with various runoff parameterizations over a Tibetan river, *Journal of Geophysical Research: Atmospheres*, *122*(3), 1488–1504, doi:10.1002/2016JD025572.
- Zorita, E., and H. von Storch (1999), The analog method as a simple statistical downscaling technique: Comparison with more complicated methods, *Journal of Climate*, *12*(8), 2474–2489, doi:10.1175/1520-0442(1999)012<2474:TAMAAS>2.0.CO;2.
- Zorita, E., V. Kharin, and H. von Storch (1992), The atmospheric circulation and sea surface temperature in the North Atlantic area in winter: Their interaction and relevance for Iberian precipitation, *Journal of Climate*, *5*(10), 1097–1108, doi:https://doi.org/10.1175/1520-0442(1992)005<1097:TACASS>2.0.CO;2.
- Zveryaev, I. I., J. Wibig, and R. P. Allan (2008), Contrasting interannual variability of atmospheric moisture over Europe during cold and warm seasons, *Tellus A*, *60*(1), 32–41, doi:10.1111/j.1600-0870.2007.00283.x.